Assembling Single RbCs Molecules with Optical Tweezers

STEFAN JOEL SPENCE

Assembling Single RbCs Molecules with Optical Tweezers

Stefan Joel Spence

A thesis submitted in partial fulfilment
of the requirements for the degree of
Doctor of Philosophy

Department of Physics
Durham University

2023

Assembling Single RbCs Molecules with Optical Tweezers

Stefan Joel Spence

Abstract

Optical tweezer arrays are useful tools for manipulating single atoms and molecules. An exciting avenue for research with optical tweezers is using the interactions between polar molecules for quantum computation or quantum simulation.

Molecules can be assembled in an optical tweezer array starting from pairs of atoms. The atoms must be initialised in the relative motional ground state of a common trap. This work outlines the design of a Raman sideband cooling protocol which is implemented to prepare an 87-Rubidium atom in the motional ground state of an 817 nm tweezer, and a 133-Caesium atom in the motional ground state of a 938 nm tweezer. The protocol circumvents strong heating and dephasing associated with the trap by operating at lower trap depths and cooling from outside the Lamb-Dicke regime. By analysing several sources of heating, we design and implement a merging sequence that transfers the Rb atom and the Cs atom to a common trap with minimal motional excitation. Subsequently, we perform a detailed characterisation of AC Stark shifts caused by the tweezer light, and identify several situations in which the confinement of the atom pair influences their interactions. Then, we demonstrate the preparation of a molecular bound state after an adiabatic ramp across a magnetic Feshbach resonance. Measurements of molecular loss rates provide evidence that the atoms are in fact associated during the merging sequence, before the magnetic field ramp.

By preparing a weakly-bound molecule in an optical tweezer, we carry out important steps towards assembling an array of ultracold RbCs molecules in their rovibrational ground states.

Declaration

I confirm that no part of the material offered has previously been submitted by myself for a degree in this or any other University. Where material has been generated through joint work, the work of others has been indicated.

Stefan Joel Spence
Durham, January 21, 2023

The data presented in this thesis are available from doi:10.15128/r2xs55mc11s

Acknowledgements

After four years of researching quantum physics, the key lesson that I have learned is my dependence on other people. Modern academia is acutely aware of this fact: we stand on the shoulders of giants; if you have a tough problem to solve, then find the person who has already solved it. On a personal level, humans are relational, and I could not have come so far without the tremendous support provided to me along the way.

First of all, I would like to thank my supervisor, Professor Simon Cornish. I have profited from his experience in leading research of ultracold molecule experiments over several decades. Occasionally I would wonder how he found time for so many people and activities requesting his attention, but he was always up-to-date and ready with sensible guidance when I needed it.

Secondly, thanks are due to my secondary supervisor, Professor David Carty, for his support and advice. Our meetings might have been infrequent, but if anything that is testimony to their effectiveness.

I should also acknowledge Durham University and EPSRC for funding my research - building an experiment for ultracold molecules is not cheap!

I owe a lot to my colleagues in the optical tweezers lab. The experiment has benefited from the leadership of several postdoctoral researchers. Ana Rakonjac inspired me with her willingness to just start tackling any issue, which was essential in the early days of the experiment. Subsequently, Alex Guttridge was a foundation of rationality and scientific knowledge, giving many hours of hard work. I am also grateful for the vital contributions of Philip Gregory, Sarah Bromley, Lewis McCard, Rahul Sawant, and Alex Alampounti. Of course, little progress would have been made without the help of my fellow PhD students. I am grateful for my friendship with Vincent Brooks and being able to learn from following in his footsteps. Thanks are also due to Dan Ruttley for his contributions - it is comforting to know that I leave the experiment in capable hands.

The benefit of working in the Durham Physics Department is the warmth of the community. I am so grateful for my friends in the Quantum Light and Matter group. In particular, I have enjoyed the opportunity to present and discuss work, life, and the rest at group meetings, seminars, pub trips, and lunchtime runs. Without understating the blessing of encouraging interactions with many people, I would like to specifically thank Dani Pizzey, Tom Cutler, Clare Higgins, Andrew Innes, and Matthew Hill for their friend-

ship and support. More generally, the Quantum Light and Matter group has greatly benefited from the selfless work of Dani Pizzey and Lucy Downs as they volunteer time organising EDI and outreach, teaching us the importance of 'extra-curricular' activities.
The later sections of this work start to delve the murky depths of ultracold molecules where the boundary between quantum physics and quantum chemistry dissolves. I am indebted to the wisdom of Professor Jeremy Hutson who provided insightful discussion and theoretical calculations. Thanks are also due to Professors Alejandro Saenz and Fabio Revuelta Peña who offered insightful discussion based on their experience of simulating trapped ultracold atom pairs.
It is so important to me to express gratitude for my family and friends who have been with me through it all. The golden years were spent living with Ant, James, and Sam. I think we all miss spending so much time together, but I am so grateful for our ongoing friendship. I am also very grateful for the friendship of Charlie Evans, Seth Price, and many others who have been with me along the way. I am unspeakably grateful to Judith, my girlfriend, for her unceasing affection and support. For their faithful support, I am most grateful for my loving parents—mum, dad—and siblings. My family have made me who I am today, and I intend to continue following their example of generosity, kindness, and following Jesus wholeheartedly.
I have reserved the final position of honour for thanking God. I have been transformed by grace, and I see no better way of living than pursuing justice and righteousness. The Lord knows my innermost thoughts and watches over every situation, whether obvious or hidden. Through God's forgiveness I am accepted, and I will live a life overflowing with gratitude.

Contents

List of Figures

List of Tables

Chapter 1

Introduction

1.1 Background

Arrays of interacting particles are an attractive system with which to advance the frontiers of quantum science. The appeal originates from a variety of factors. Spatial separation of the particles provides a means of suppressing collisional loss. Rearrangement techniques permit deterministic preparation of the initial arrangement [1–6]. The interactions between the particles can be used for gate operations [7, 8], investigating the phase transitions between novel phases of matter [9–11], and creating entangled states [12–15]. Furthermore, increasingly complex operations are possible as the system size is scaled up, with the limitation of scalability usually being of technical nature [16].

The applications of arrays of interacting particles are as varied as the possible implementations. Quantum simulation of complex systems [17] is possible using trapped ions [18–20], Rydberg atoms [21, 22], polar molecules [23–26], or magnetic atoms [27, 28]. Alternatively, an array of alkaline-earth atoms has suitable characteristics for precise clock measurements [29–31]. Another area of interest is quantum computation, which promises solutions to complicated problems using algorithms that are intractable on classical computers [32, 33]. Experimental realisations of quantum computers include systems of trapped ions [34, 35], and Rydberg atoms [36, 37]. Using atoms as qubits takes advantage of the fact that they are identical particles, which is not the case for superconducting processors or quantum dots [38–41]. An alternative

platform uses photons as information carriers, and significant advances have been made to overcome the challenges of creating low loss interfaces and high efficiency detectors [42, 43]. Alongside the progress in these fields, there are proposals to leverage the long-range interactions between heteronuclear molecules [44–48]. Such ambitious proposals become increasingly feasible thanks to technological advances in laser technology and demonstrations of single-particle control [49–52]. In this work we demonstrate steps towards assembling an array of ultracold molecules with prospects for applications in quantum computation and quantum simulation.

1.2 Array Generation

There are several ways to generate an array of traps. Quantum gas microscopes use interfering laser beams propagating in different directions to generate an optical lattice that can trap large samples of atoms. Alternatively, one can generate an array of optical tweezers by focusing a laser beam down to micron-sized spots. These two methods for array generation have different advantages and weaknesses.

1.2.1 Optical Lattice

A quantum gas microscope combines the manipulation of large samples of atoms (or molecules) and imaging with single-site resolution [53]. Interfering laser beams produce an optical lattice that can trap particles in typically hundreds or thousands of sites with subwavelength separation [54–56]. Single-site imaging is achieved using super-resolution microscopy [57–60].

The pattern of the array, including the lattice spacing, is determined by the geometry of the laser beams. Appropriate laser alignment can realise non-cubic patterns including triangular [61] or honeycomb lattices [62]. Systems in these geometries are expected to exhibit transitions between exotic quantum phases. Furthermore, an appropriate choice of polarisation for the laser beams creates state-dependent lattices - another handle for controlling the system.

Optical lattices isolate groups of particles, and are capable of isolating single particles. The average occupation probability of a lattice site becomes near unity after a phase transition to the Mott insulator state [63], and deep in the Mott insulator regime there is a region where the density is constrained to one particle per site. One issue is that even if one achieves a high average filling fraction of lattice sites, the location of residual unoccupied sites is random. A solution is imaging and sorting the positions of particles into a sublattice, for example by shifting atoms with a state-dependent lattice [64]. Such schemes for deterministic preparation of an ordered array require the capability to address single particles, which is possible using optical tweezers.

1.2.2 Optical Tweezers

Optical tweezers are individual microtraps formed by focusing light and attracting microscopic particles to a region of peak intensity [65]. The optical tweezer is a convenient tool for imaging and addressing single particles. The tweezer traps a single particle, which is useful for circumventing issues with lossy collisions [66–71]. Light-assisted collisions during the loading of the tweezer selectively remove multiple atoms in pairs, leaving either one or zero atoms remaining [72]. Using red-detuned incident light, the probability of observing an atom in the trap is ~ 0.5, however grey-molasses techniques can enhance the loading probability to > 0.9 [73–77].

Optical tweezer arrays have become an established tool for trapping neutral atoms [21, 22, 74, 78–82]. As a platform, tweezer arrays have a range of desirable characteristics for experiments in quantum simulation and quantum compuation [83, 84]. Aside from limiting the trap occupancy to less than two atoms, tweezers also offer dynamic control over trap positions, which is useful for reducing entropy by rearranging traps into an ordered array [3–6, 85], or merging traps [50, 86, 87]. Another benefit is in the flexibility of the control; traps can be arranged in arbitrary geometries [81, 88].

Several methods allow generation of an optical tweezer array. A digital micromirror device (DMD) manipulates an array of micro-mechanical mirrors that can holographically generate an arbitrary array of traps [6]. However, the DMD is not suitable for dynamic movement of the traps due to a technical

issue that would heat the atom during transport. A liquid crystal spatial light modulator (SLM) works by a similar principle, but the mirrors are replaced with electrodes that modify the refractive index of a liquid crystal [78, 81, 89–91]. Again, the SLM is not suitable for dynamic movement of the traps, but this time because the refresh rate is too slow. Another alternative is using an acousto-optic deflector (AOD) [4, 92], or two crossed AODs to generate a 2-dimensional array [3]. Driving the AOD with a multi-tone radio-frequency (RF) signal deflects the incident laser beam down multiple paths, and an optical relay system redirects the light to create an array of traps. The AOD is particularly suitable for dynamic steering of traps [86, 93]. However, it can be challenging to produce large arrays due to the intermodulation of multiple tones and limited diffraction efficiency. A popular compromise is to create a static array with an SLM, and use an AOD to steer a "shuttle" trap that moves atoms between sites of the static array [21, 88].

While most experiments use a single species of atom, dual-species experiments open new avenues for research. The species can be distinguished by their different transition frequencies [94]. Then species-selective imaging could be used to perform quantum non-demolition measurements with low cross-talk [95] as part of a quantum error correction scheme [96]. Furthermore, species-selective traps using tweezers with different wavelengths [87, 97, 98] provide a route towards association into a molecular state [99].

1.3 Ultracold Molecules

Polar molecules offer additional advantages over neutral atoms that can be leveraged for research in quantum science [100, 101]. Research proposals exploit the rich internal structure of rotational, vibrational, and electronic energy levels of a molecule, the strong coupling to electric fields, and the long-range dipole-dipole interactions (DDI) between heteronuclear molecules. These features make arrays of ultracold molecules an enticing platform for quantum simulation [23–26], quantum computation [15, 44–48, 102], and precision measurements of fundamental physics [103].

As an aside, Rydberg atoms present an alternative system where long-range

DDI and strong coupling to external fields can be used for quantum technologies [104, 105]. Arrays of Rydberg atoms are already being used as quantum simulators of spin models [21, 22, 92]. However, applications are often limited by the relatively short lifetime of order $100\,\mu$s [37]. Circular Rydberg states might provide a route towards extending the lifetime, and have valuable prospects for future research [106–108].

As for molecules, applications in quantum information processing benefit from the ability to choose from a large number of quantum states. Proposals of using molecules for quantum computation require storage qubits with long coherence times, single-qubit rotations, and gate operations carried out by spin-exchange interactions [45, 48]. Appropriate states have been identified by research on molecules in bulk gases. Robust storage qubits can be constructed from particular hyperfine states [109, 110] or coherent superpositions of hyperfine states [111–113] or rotational states [114]. Single-qubit rotations have been demonstrated using coherent transfer between rotational states mediated by a microwave field [115, 116]. The spin-exchange interaction has been observed for molecules in optical lattices [117, 118], and an optical tweezer array [119].

Combining the rich internal structure with long-range interactions make molecules an ideal system for applications in quantum information processing [120]. The use of magic-polarisation traps [111–113, 121] and magic-wavelength traps [122, 123] extends rotational coherence times between multiple states. Exploiting these features, molecules could be used to encode qudits [102] or synthetic dimensions [124].

In practice, there are two routes towards preparing a system of ultracold molecules. The first takes the direct approach of cooling and trapping molecules from an appropriate source. The second starts by using well-established techniques to cool atoms which are then associated into a molecule. Each route has its own advantages and challenges.

1.3.1 The Direct Approach

The difficulty in directly cooling a molecule is that the complexity of the internal energy level structure impedes the search for a closed cooling cycle

[125], an essential element of laser cooling. Sources of cold molecules are available using buffer-gas cooling, Stark decelerators or Zeeman decelerators [100]. However, the cooling is insufficient for loading an optical trap.

Certain species of molecules have been directly cooled by taking advantage of diagonal Franck-Condon factors which limit the number of decay channels [126–129]. Advances in cooling techniques led to the trapping of molecules in optical tweezers [52] and observation of spin-exchange interactions [119]. However, the removal of thermal dephasing by cooling to the motional ground state remains an ongoing challenge due to the complexity of the internal structure [130].

1.3.2 The Indirect Approach

A desirable alternative method for preparing ultracold diatomic molecules is to assemble them from pairs of alkali atoms. This method capitalises on well-established cooling and imaging techniques developed for neutral atoms. Experiments using bulk mixtures have refined the process of cooling atoms and subsequently associating them into a weakly-bound state using a magnetic Feshbach resonance [131–134]. The weakly-bound molecule can then be transferred into the rovibrational ground state by stimulated Raman adiabatic passage (STIRAP) [135–144]. This efficient two-stage process overcomes the vanishing wavefunction overlap between the atom-pair state and the rovibrational ground state molecule by using the weakly-bound state as an intermediary. Since its demonstration in bulk mixtures, the indirect method has been used to prepare rovibrational ground state molecules in an array of optical tweezers [145].

Efficient association first requires cooling to high phase space density, or in the case of an atom pair in an optical tweezer, to the relative motional ground state of a harmonic trapping potential [146]. Motional ground-state cooling is achievable through sideband cooling, a technique first demonstrated on ions [147, 148]. Raman sideband cooling has since been used for efficient motional ground state preparation of neutral atoms in optical tweezers [149–154].

Two atoms prepared in the motional ground state of separate tweezers can be merged into a common trap and associated into a bound state. The molecule

inherits the initial motional state of the atom pair [99, 155]. Multiple techniques for association exist, including RF association [155], photoassociation [156], or magnetoassociation [99]. For the popular method of magnetoassociation, an applied magnetic field is swept across an interspecies Feshbach resonance so that the atoms adiabatically follow an avoided crossing into a molecular state [133]. With an appropriate choice of ramp speed, an atom pair in the relative motional ground state of the trap can be associated into a bound state with a conversion efficiency near unity.

The next stage is transferring the molecule to the rovibrational ground state. Several methods might accomplish coherent transfer, but in our case STIRAP is anticipated to be the most efficient. The process of STIRAP involves controlling the time-dependent coupling of a probe beam and a Stokes beam that are incident on the molecule. The molecule remains in a dark state that is coherently transformed from the initial weakly-bound state to the final rovibrational ground state as the powers of the beams are changed. The process of cooling atoms, forming a molecule by magnetoassociation, and coherently transferring the molecule to its rovibrational ground state has been used to prepare a NaCs molecule in an optical tweezer [157] and has been extended to prepare an array of molecules [145].

There is incentive to apply these techniques to prepare different bialkali molecules; the ^{87}Rb^{133}Cs molecule in particular benefits from a history of theoretical and experimental research. Measurements of interspecies Feshbach resonances and molecular spectroscopy determined an efficient method for association and transfer into the rovibrational ground state [141, 158]. Furthermore, for RbCs there has been detailed characterisation of the rotational and hyperfine structure [159–161] and AC Stark shifts [116, 160]. Research has also identified where a magic-wavelength trap can eliminate differential AC Stark shifts between multiple rotational states by taking advantage of the molecular structure of the $X^1\Sigma^+ \rightarrow b^3\Pi$ transition in RbCs [123]. This is an important finding given that AC Stark shifts are a major source of decoherence for transitions between rotational states. Overall, there are exciting prospects for research using RbCs molecules. Our experiment intends to implement the indirect method to assemble an optical tweezer array of RbCs molecules in their rovibrational ground states.

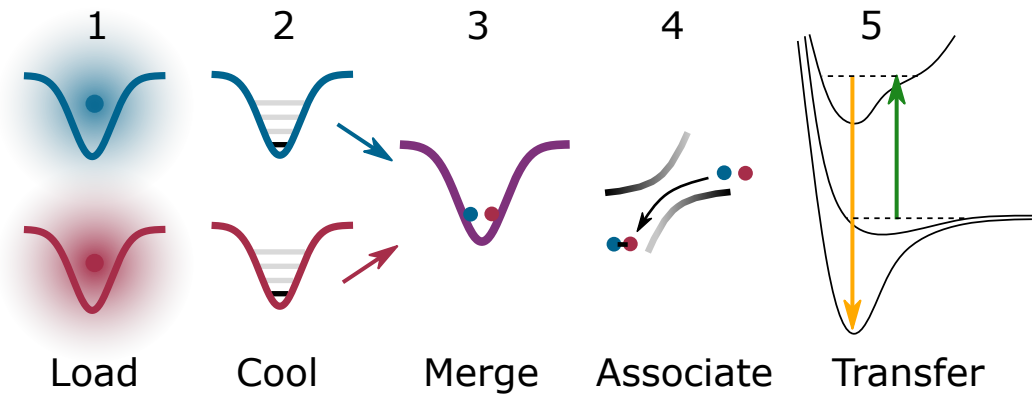

Figure 1.1: An overview of the stages required to assemble a molecule in its rovibrational ground state. The process will be expanded to assemble an array of RbCs molecules in parallel.

1.4 Route to Ultracold Molecules

Following the indirect approach, we design an experiment that prepares a molecule in the rovibrational ground state starting with single atoms. The required steps are outlined in Figure 1.1. Using optical tweezer arrays, the process can be expanded to assemble an array of molecules in parallel. It is worth providing additional context for each of the required steps.

Firstly, we start by loading a Rb atom and a Cs atom into separate optical tweezer traps. Throughout this work, a sequential scheme first loads a Rb atom, then repeats the process to load a Cs atom. Starting with a magneto-optical trap (MOT), we cool a cloud of atoms localised around the tweezer trap. From the cloud, a single atom becomes trapped in each tweezer.

Secondly, the two atoms must be prepared in particular quantum states. The atoms are cooled to the motional ground state of their respective traps using Raman sideband cooling (RSC). Subsequent microwave (MW) transitions or two-photon Raman transitions transfer to the spin state from which association is possible using techniques established in bulk mixtures of Rb and Cs [162, 163].

Thirdly, the two atoms must be transferred to a common trap. The merging process needs to conserve the quantum state. Therefore, we perform a thorough investigation to determine a trajectory that overlaps the traps with

minimal motional excitation of the atoms.

Fourthly, a magnetoassociation ramp across a Feshbach resonance transfers the atom pair into a weakly-bound state. Subsequently, STIRAP transfers the molecule to the rovibrational ground state. The STIRAP, association, and merging stages will be reversed to detect surviving atoms as evidence of coherent transfer. Expanding the process to create an array of molecules will allow investigations into dipole-dipole interactions between molecules.

1.5 Thesis Outline

Following the structure of the sequence that prepares a molecule, the rest of this thesis outlines progress made towards the creation of a molecule in its rovibrational ground state.

- Chapter 2 describes the experimental apparatus, including laser systems, magnetic coils, and software control. Particular focus is given to developments upon the work described in Ref. [164].
- Chapter 3 explains our methods for loading atoms and preparing a particular spin state. We characterise the initial cooling with a temperature measurement and provide a thorough characterisation of the state preparation fidelity.
- Chapter 4 describes the theory used to design a pulse sequence for RSC. The result is a robust cooling protocol with a high probability of preparing an atom in the motional ground state. To accomplish this, we use numerical simulations of the master equation and investigate cooling the motional state distribution from high-lying motional levels.
- Chapter 5 applies the RSC pulse sequence to a Rb atom and a Cs atom in separate tweezers. After confirming high-fidelity motional ground state preparation, we quantify the effects of several sources of decoherence. After balancing the intensities of four tweezers, we apply the RSC protocol to a 1D array of Rb atoms, demonstrating the capability for scaling up the procedure. Finally, we determine a trajectory that

merges the tweezers with minimal motional excitation and prepares an atom pair in the relative motional ground state of a common trap.

- Chapter 6 is about the interactions between an atom pair near to a Feshbach resonance. The theory of Feshbach resonances is introduced, and we take account of the influence of the trapping potential on the energy eigenstates of the atom pair. We present measurements of AC Stark shifts when the tweezer light has a frequency near to a molecular transition. Then, we demonstrate association into a molecular bound state and characterise the lifetime of the bound state, which is limited by photoexcitation driven by tweezer light.

- Chapter 7 provides an outlook towards immediate and long-term goals for the experiment. We introduce the laser system required to perform STIRAP and present measurements of single-photon spectroscopy of an excited molecular state in the spin-orbit coupled $A^1\Sigma^+ - b^3\Pi$ potential. These measurements provide insight into the binding energy of the molecule. Finally, we discuss the prospects for experiments starting with an array of RbCs molecules in the rovibrational ground state.

1.6 Contributions of the Author

The optical tweezers experiment at Durham is founded upon the contributions of many talented researchers, under the guidance of Professor Simon Cornish. Myself, Vincent Brooks, and Daniel Ruttley are the PhD students who have worked on this project. Several postdoctoral researchers have contributed, including Ana Raconjak, Alex Guttridge, Philip Gregory, Lewis McCard, Alex Alampounti, and Rahul Sawant. Students on master's and summer projects have contributed, including Wendy Tomboza, Jie (Ben) Zhang, Ce Li, and Albert Tao.

When I arrived, Ana, Vincent, Phil, and Lewis had assembled the vacuum system, magnetic coils, and the laser system for MOT beams, and recently observed the first MOT of Cs atoms. Later, the servos for the bias and jump coils were set up and characterised by Alex and Dan. The laser system and locking for the MOT and OP beams was designed by Ana and Vincent, who

also set up the optics. I picked up initial designs for the Raman beams from Ana and Vincent, and fleshed out a plan of the required hardware for implementing RSC. I led the setup of the optics for the Raman beams, with help from Vincent and Alex. Ana and Vincent built the initial optical setup for the tweezers. Alex and I designed and implemented the changes to the dichroic mirror mounts. I performed the characterisation measurements of the two-axis AOD, and Alex aided me with its installation. I wrote PyDex, the master experimental control script, incorporating the SLM and microwave generator scripts written by Dan. Lewis developed the DDS rack and wrote the code which was incorporated into our software control. Alex A wrote the basis of the AWG code which was later upgraded by Vincent, myself, and Dan. The method for rearrangement was designed by Vincent. I performed the experiments overlapping the tweezer positions, with help from Alex and Dan for the axial alignment. Alex, Dan, Vincent and I characterised the tweezer trap beam waists and performed temperature measurements. Alex and I characterised the OP and transfer between spin states. I created the simulations of RSC, based on the idea that Rahul started. I designed the pulse sequence under the guidance of Alex and Simon. I performed the experiments testing the performance of the RSC protocol and choosing a merging trajectory with the help of Alex and Dan. Alex, Dan, and I carried out the experiments characterising the Stark shift of the Feshbach resonance and association into a bound state. Alex and Dan carried out the experiments of single-photon spectroscopy of the weakly bound state.

Calculations of the wavefunctions of RbCs bound states were provided by Jeremy Hutson, alongside guidance on the interpretation of experimental measurements of weakly-bound molecules.

1.7 List of Publications

The following publications were completed during the course of this work:

- R. V. Brooks et al., "Preparation of one ^{87}Rb and one ^{133}Cs atom in a single optical tweezer", *New J. Phys.* 23, 6 (2021), p. 065002
- R. V. Brooks et al., "Feshbach Spectroscopy of Cs Atom Pairs in Opti-

cal Tweezers", *arXiv:2204.08877* (2022), URL: https://doi.org/10.48550/arXiv.2204.08877 (accepted in the New J. of Phys. at the time of writing: https://iopscience.iop.org/article/10.1088/1367-2630/ac99f6)

- S. Spence, R. V. Brooks, D. K. Ruttley, A. Guttridge, and S. L. Cornish, "Preparation of ^{87}Rb and ^{133}Cs in the motional ground state of a single optical tweezer", *New J. Phys.* 24, 10 (2022), p. 103022

Chapter 2

Experimental Apparatus

Ultracold atom experiments are assembled from a range of parts. This chapter describes the equipment we use to cool individual atoms and assemble single molecules in optical tweezers. Much of the apparatus has been introduced in previous publications [98, 164–166]. Here, we will provide an overview of the whole apparatus, and then focus on the most recent upgrades, which include reducing the clipping of the beams generating the tweezers and inserting a 2D acousto-optic deflector (AOD) to control the position of the 817 nm tweezer. Finally, we present the computer control software and additional modules that were developed alongside the experiment.

2.1 Hardware

2.1.1 Vacuum System

We create a controlled environment for trapping single atoms by isolating atoms in a vacuum. The key components of the experimental apparatus are illustrated in Figure 2.1. A vacuum pump maintains a pressure of $< 1 \times 10^{-10}$ torr inside the system. Alkali metal dispensers running at a current of ~ 2 A feed small amounts of Rb and Cs into an anti-reflection-coated science cell with interior dimensions $20 \times 20 \times 60\,\mathrm{mm}^3$ and a wall thickness of 3 mm. In-vacuum electrodes will be used to produce large DC electric fields in the centre of the cell. The coating of the cell transmits light

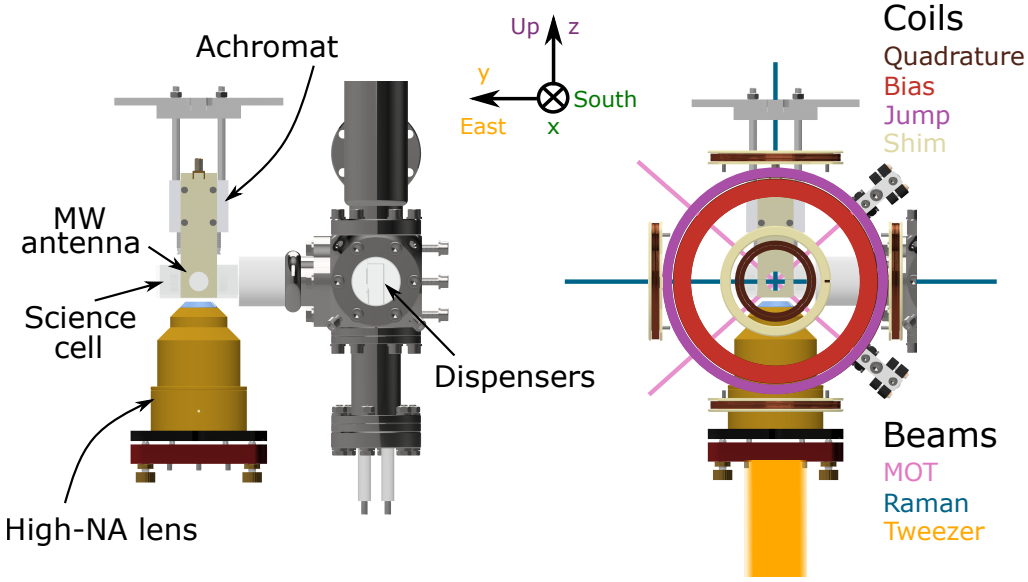

Figure 2.1: The key components of the main table apparatus. On the left the magnetic coils and laser beams are hidden for clarity, otherwise the images show the same components. Lasers focused through the high-NA objective lens form optical tweezer traps in the science cell. Single atoms are trapped and manipulated with the magnetic coils, a range of different lasers, and two MW antennae. We define a right-handed coordinate system with the x-axis pointing south. The compass coordinates - North/South, East/West, and Up/Down - are used to name the shim coils.

at wavelengths between $750 - 1100\,\text{nm}$, allowing lasers to be aligned to a central region to trap and cool atoms.

2.1.2 Objective Lens and Microwave Antennae

An objective lens with a numerical aperture (NA) of 0.55 sits 2 mm beneath the cell and is used to form optical tweezer traps at the centre of the cell. The high-NA lens has an effective focal length of 35.34 mm and a working distance of 15.5 mm such that the tweezer beams focus down to a waist of $\sim 1\,\mu\text{m}$. The same objective lens is used to collect atomic fluorescence in order to image atoms trapped in the tweezers. The objective lens was characterised in previous work [164] where we calculated a collection efficiency of 5.0(8) % for photons emitted by a Rb or a Cs atom.

Several appendages enable further control of trapped atoms. Two microwave (MW) antennae are each positioned 2 mm from the cell. They are designed to output circularly polarised MW radiation at frequencies around 6.8 GHz or 9.2 GHz [164], which is the splitting of the ground-state hyperfine energy levels of Rb or Cs respectively. In practice, the emitted field has a superposition of left-handed and right-handed circular polarisation in a ratio of $\sim 7:1$, but by applying a bias field we enforce dipole selection rules and create a Zeeman shift such that we can selectively drive transitions to a single hyperfine sublevel. Additionally, an achromatic lens (Thorlabs AC254-050-B) with a focal length of 50 mm is mounted above the cell. Its purpose is to focus beams onto the atoms and to refocus tweezer light exiting the cell for characterisation of a tweezer array.

2.1.3 Electromagnetic Coils

Magnetic fields are required for trapping clouds of atoms, controlling the spin state of an atom, and magnetoassociation into a molecular state. We accomplish these processes using six pairs of electromagnetic coils wired up around the experiment. The key characteristics are summarised in Table 2.1. The quadrupole, bias, and jump coils all have a hollow core which has fluid from a cooling system flowing through it in order to counteract the heating

Coil name	Calibration ($\mathrm{G\,A^{-1}}$)	Typical Field (G)	Inductance (μH)	Axis
Quadrupole	0.2991(6) ($\mathrm{cm^{-1}}$)	8.47 ($\mathrm{cm^{-1}}$)	2	x
N/S shim	1.211(3)	4.78	84	x
E/W shim	0.927(4)	< 0.5	533	y
U/D shim	0.939(3)	< 1	461	z
Bias	1.3926(7)	180	40	x
Jump	0.2814(7)	20	7	x

Table 2.1: Summary of the main characteristics of the different electromagnetic coil pairs.

caused by the large electrical powers dissipated in the coils. There are a few things to note about each of the coils in turn.

Quadrupole and Shim Coils

The quadrupole coils are in an anti-Helmholtz arrangement such that they produce a uniform magnetic field gradient near the midpoint along the x-direction. During the magneto-optical trap (MOT) stage, the field gradient is set to $8.47\,\mathrm{G\,cm^{-1}}$ so that atoms are confined near the field zero.

The N/S, E/W, and U/D shims are pairs of Hemlholtz coils named according to the direction of the field that they produce. The shims cancel static stray fields during the loading, cooling, and imaging stages. The field from the shim coils shifts the position of the field zero during the MOT stage so that the MOT can be overlapped with the tweezer traps. The shims are driven by a bipolar current supply, which allows the field direction to be flipped by inverting the direction of current through the coils. Each shim coil can produce a field magnitude of up to $\sim 5\,\mathrm{G}$. The shim coils are not water-cooled since only small currents are required to produce these fields. We define a quantisation axis during the optical pumping (OP) and Raman sideband cooling (RSC) stages by using the N/S shims to apply a $4.78\,\mathrm{G}$ field along the x-direction.

Bias coils

The bias coils are also named the Feshbach coils since they provide fields of up to 200 G, close to the relevant inter-species Feshbach resonances used for magnetoassociation. The field points in the x-direction, the same direction as the N/S shim coils, and is intended to provide a large, static magnetic field that is held constant during the association and dissociation of a molecule. We are therefore more concerned about possible damage to the coils as a result of heating from using high currents rather than about the ability to make dynamic changes to the magnetic field.

A home-built servo circuit controls the current in the coils, and we take steps to ensure that its components do not overheat. The circuit converts a user-defined setpoint voltage into a stable voltage reference, which controls the gate voltages of four MOSFETs (IXYS Corp IXFN200N10P) connected in parallel. A Hall sensor (Honeywell CSNJ481) in series with the coils feeds back a measure of the current to be stabilised relative to the setpoint voltage. When setting up the coils, a major consideration is the power dissipated in the MOSFETs, which are rated for temperatures of up to 150 °C. Reaching fields of $\sim$ 200 G requires drawing currents of up to 150 A. While we cannot measure the resistance of the MOSFETs directly, we precisely infer the voltage drop across the MOSFETs by measuring the resistance of the whole circuit excluding the MOSFETs and using the fact that the current is uniform throughout the components connected in series. For our power supply voltage of 5.5 V and with the resistance of the coils and connecting cables measured as 36.9(2) mΩ, the power dissipated over each MOSFET remains less than 60 W. We determine that this safely limits the temperature to < 100 °C, given that the coils are running at high currents for a maximum of 150 ms (with a duty cycle of $\lesssim$30 %) and the thermal response of the MOSFETs is $< 0.2\,\mathrm{K\,W^{-1}}$. Furthermore, the heat sink of the MOSFETs is connected to the water cooling system to prevent heat building up over time. With a flow rate of 0.5 L per minute, it provides a cooling rate of > 700 W, which is greater than the power dissipated in the MOSFETs. A parallel cooling system passes coolant through the central bore of the coils to prevent overheating. The total resistance of the bias coils is measured as

$R = 32.5(2)\,\mathrm{m\Omega}$, meaning that a power of $731(5)\,\mathrm{W}$ is dissipated for a current of $150\,\mathrm{A}$. This is comparable to a conservative estimate of the cooling rate for the coils. Therefore, the temperature in the coils remains stable even for continuous operation at high currents. Despite having calculated the safe operational limits, we avoid running the coils continuously at high currents as a final precaution.

The dynamic response of the coils is limited by the servo control and the inductance of the coils. The servo circuit has capacitors as part of its PI control, but the capacitors can be bypassed in order to make fast jumps in the current. With the capacitors bypassed the field is close to $180\,\mathrm{G}$ within a few milliseconds of turning the coils on. These timescales are acceptable given that the bias coils are predominately used for constant offset fields.

Jump coils

The standard process for magnetoassociation involves ramping the magnetic field across a Feshbach resonance. In our experiment, the jump coils provide dynamic control over the magnetic field strength. The jump coils produce a field that points in the x-direction and can provide up to $\sim 42\,\mathrm{G}$ using a current of $150\,\mathrm{A}$. This smaller magnetic field is summed with the large, constant magnetic field from the Bias coil during magnetoassociation. It is still important to minimise the risk of overheating, but the dynamic response of the jump coils is the most important concern.

The servo circuit that controls the current is a replica of the one for the bias coils. To reach currents of up to $150\,\mathrm{A}$, we run the power supply at $3\,\mathrm{V}$. Then the power dissipated in each of the four MOSFETs is $< 40\,\mathrm{W}$, given that we measure a resistance of $14.060(8)\,\mathrm{m\Omega}$ for the circuit excluding the MOSFETs. This is well within the safety threshold. Similarly, the total power dissipated in the coils is less than the cooling rate of its cooling system. The measured resistance of the jump coils is $8.776(6)\,\mathrm{m\Omega}$, meaning that a maximum power of $200\,\mathrm{W}$ is dissipated in the coils for a current of $150\,\mathrm{A}$.

The jump coils are intended to provide faster switching times than the bias coils, so that they can be used for ramping the field during a magnetoassociation sequence. The switching time is limited to the order of $1\,\mathrm{ms}$ by the

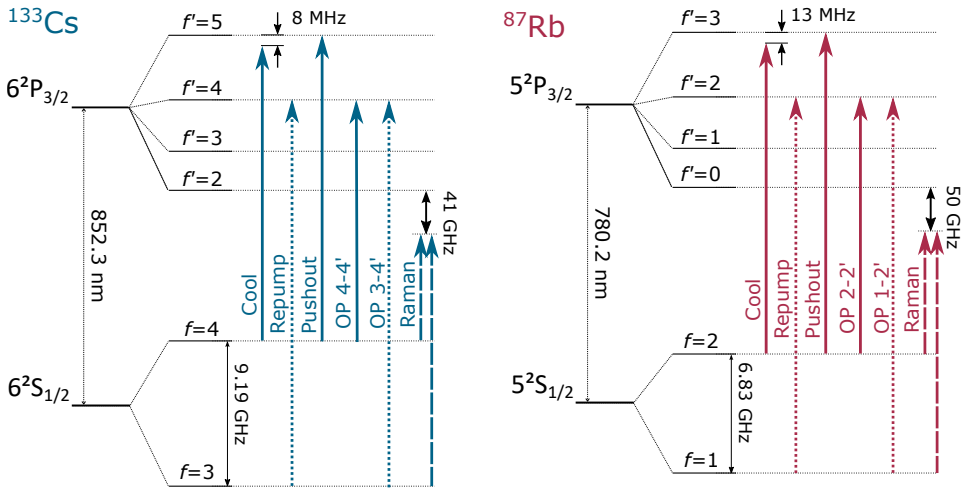

Figure 2.2: The laser frequencies with respect to the atomic transitions that they address. Six beams are generated from three laser sources (solid, dotted and dashed lines) to address Cs atoms. A duplicate system addresses Rb atoms. The cool and repump laser beams are used for the MOT, polarisation gradient cooling, and imaging. The pushout beam is used for state-selective detection. The optical pumping beams are used to prepare a specific hyperfine sub-level. The Raman beams are used for Raman sideband cooling.

inductance of the coils. This timescale is similar to the RC time constant of the servo circuit with the integrator activated, so there is not a significant benefit from bypassing the integrator. In practice, we rarely want to ramp the field so quickly, such that these timescales are not limiting.

2.1.4 Laser System

We use a total of nine lasers to carry out the stages on the route to assembling a molecule. The laser sources are all kept on an optical table - the laser table - separate from the main table with the experimental apparatus. We lock several beams to the same atomic reference by dividing a common laser source between several paths. Each path has its own acousto-optic modulator (AOM) to change the frequency and attenuate the light. The different paths are sometimes recombined before being coupled into polarisation-maintaining optical fibres which carry the light over to the main table. The optical

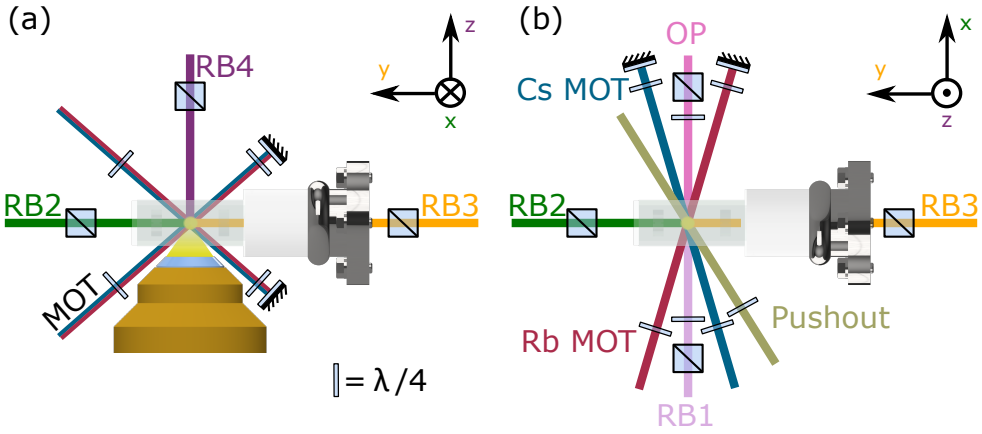

Figure 2.3: The laser beams incident on the science cell. The lasers are all fibre-coupled across from a separate table. (a) Facing along the x-axis. The vertical MOT beams overlap 780 nm light for Rb and 852 nm light for Cs using dichroic mirrors. The MOT beams are retro-reflected after passing through quarter waveplates. Raman beams RB2, 3, and 4 are all linearly polarised. The optical tweezer lasers focus through the high-NA objective lens. (b) Looking down on the experiment from above. The optical pumping, pushout, RB1, and MOT beams are all circularly polarised using quarter waveplates.

setup on the laser table has been explained in a previous thesis, along with a description of the laser locking [164]. Therefore, here we will focus on the beams incident on the atoms and their roles depicted in Figure 2.2. Additionally, Figure 2.3 displays the geometry of the laser beams, which is important for cooling the atoms in 3D.

Magneto-Optical Trapping Beams

Three pairs of laser beams are used to form a MOT in the first 150 ms of an experimental sequence. The beams in a pair are carrying light that addresses Rb or Cs respectively, with negligible cross-talk. To form a MOT, the quadrupole coils apply a magnetic field gradient and the lasers remove kinetic energy from the atoms. Each beam is composed of two frequencies of light generated from different lasers; a cooling laser and a repump laser. Figure 2.2 shows the atomic transitions addressed by the cooling and repump lasers. In this context, f is the total angular momentum quantum number combining the nuclear spin with the angular momentum of the electron, which has a projection m_f onto the quantisation axis. The cooling light is $\sim 10\,\mathrm{MHz}$ red-detuned from the free-space $f = 2 \rightarrow f' = 3$ transition for Rb, and the $f = 4 \rightarrow f' = 5$ transition for Cs. A slowing force is created through the repeated absorption of photons Doppler-shifted into resonance with the Zeeman-shifted transition frequency [167, 168]. A second frequency is required because atoms excited by the cooling light have a small probability of decaying to the lower hyperfine manifold. So-called repump light is used to pump atoms back into the cooling cycle. The repump light is resonant with the $f = 1 \rightarrow f' = 2$ transition for Rb, and the $f = 3 \rightarrow f' = 4$ transition for Cs. For efficient cooling of Rb in the MOT, each beam typically has 0.6 mW (a total intensity of $\sim 30 I_{\mathrm{sat}}$) of cooling light and 0.3 mW of repump light. For Cs, each beam typically has 0.4 mW (a total intensity of $\sim 24 I_{\mathrm{sat}}$) of cooling light and 0.4 mW of repump light.

On the main table, the MOT beams are aligned to cool the atoms in 3D. Figure 2.3(a) shows that the MOT beams in the vertical y-z plane have 780 nm light and 852 nm light overlapped using a dichroic mirror. In contrast, Figure 2.3(b) shows the horizontal MOT beams are independent, which is

a useful degree of freedom during alignment. The MOT beam radii of $\sim$ 1.5 mm are small enough to reach the atoms without clipping on the in-vacuum electrodes. Each of the MOT beams has a quarter waveplate ($\lambda/4$) that sets the polarisation as circular. A second quarter waveplate before the retro-reflection mirror ensures that retro-reflected beam has the same handedness as the incoming beam.

After the MOT stage, the same MOT beams are subsequently used for polarisation gradient cooling (PGC) [169]. This step has multiple purposes: it provides sub-Doppler cooling and induces light-assisted collisions so that the optical tweezer is occupied by either 1 or 0 atoms. To accomplish this, the quadrupole field is turned off and the frequency of the Rb (Cs) cooling beam is further red-detuned to 80 MHz (60 MHz) from the free space cooling transition. We also apply PGC at other points in the sequence, such as just after taking a fluorescence image in order to counteract heating of the atom during the imaging pulse.

The MOT beams are also used for fluorescence imaging. We image Rb and Cs atoms simultaneously in separate tweezer traps by pulsing the MOT beams on for 20 ms. During the image the tweezer trap depth is set to 1mK for Rb atoms.We use a lower trap depth of 0.5 mK for Cs atoms to reduce loss caused by scattering tweezer light at a wavelength near 920 nm which excites the atom from $6P_{3/2}$ into an antitrapped state. This is necessary despite the fact that the proportion of tweezer light at 920 nm is suppressed using an optical line filter on the tweezer laser diode output, Semrock Maxline LL01-976-12.5 [164]. The Rb cooling light is red-detuned by 21 MHz from the free space cooling transition and set to a power of 0.4 mW per beam (total intensity $\sim 20 I_{\mathrm{sat}}$), whereas the repump light is still on resonance but with a reduced power of 0.04 mW per beam in order to reduce background scattered light. Similarly, the Cs cooling light is red-detuned by 36 MHz and set to a power of 0.4 mW per beam (total intensity $\sim 24 I_{\mathrm{sat}}$), and the repump light reduced to a power of 0.05 mW per beam.

State-selective Pushout Beam

In many experimental sequences we are interested in measuring the internal state of the atom. We accomplish this using a circularly-polarised resonant pushout beam [170, 171]. The pushout beam has light at two frequencies which are resonant with the $f = 2 \rightarrow f' = 3$ transition for Rb and the $f = 4 \rightarrow f' = 5$ transition for Cs respectively. Pulsing on this beam with an intensity of $\sim 3\,\mathrm{mW\,cm^{-2}}$ for $500\,\mu$s ejects atoms from a $\sim 0.3\,$mK potential if they are in the ground-state upper hyperfine manifold while having an insignificant effect on atoms in the lower hyperfine manifold. The pushout maps the atomic spin state onto the trap occupancy which is determined in a subsequent fluorescence image.

Optical Pumping Beams

The OP beams are used for both the initial state preparation and OP during RSC. This description of our OP scheme is taken from Ref. [166]. We pump to a spin-stretched hyperfine sub-level using circularly polarised light to drive σ^+ transitions. To ensure that there is only a single dark state, the OP beam is composed of two frequencies for each atomic species. The $\mathrm{OP}^{\downarrow}$ beam drives $|f = i - 1/2, m_f\rangle \rightarrow |f' = i + 1/2, m'_f = m_f + 1\rangle$ transitions, where the nuclear spin quantum number is $i = 3/2$ for Rb and $i = 7/2$ for Cs. The $\mathrm{OP}^{\uparrow}$ beam drives $|f = i + 1/2, m_f\rangle \rightarrow |f' = i + 1/2, m_{f'} = m_f + 1\rangle$ transitions. In this case, the spin-stretched states, $|\uparrow\rangle = |f = 2, m_f = 2\rangle$ for Rb and $|\uparrow\rangle = |f = 4, m_f = 4\rangle$ for Cs, are dark to the OP light provided that the $\mathrm{OP}^{\uparrow}$ beam selectively drives σ^+ transitions. To this aim, high-purity circular polarisation is achieved using a polariser with extinction $> 5000 : 1$ (Qioptiq G335722000) followed by an achromatic quarter waveplate (Edmund Optics #46-560).

Raman Beams

The following description of generating Raman laser beams is taken from Ref. [166].

All of the Raman beams for one species are generated from the same laser,

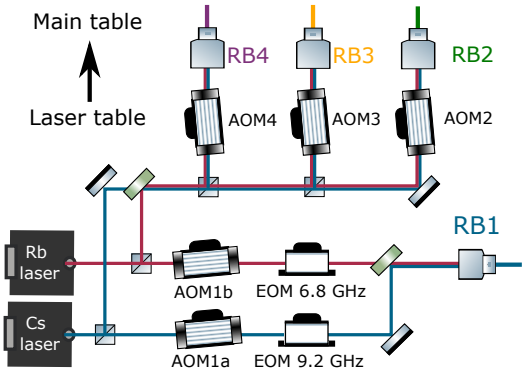

Figure 2.4: Lasers operating at 780 nm and 852 nm generate light for driving Raman transitions in Rb and Cs, respectively. Electro-optic modulators (EOM) add frequency sidebands to the RB1 beams at the hyperfine splitting of the electronic ground-state, prior to overlap. For the remaining Raman beams, the 780 nm and 852 nm light is first overlapped and then split into three separate beam paths, each with an acousto-optic modulator (AOM) to control the power. Figure reproduced from [166].

which ensures the phase coherence of two-photon Raman transitions. Figure 2.2 depicts the frequencies of the lasers used for Raman transitions. Our choice of laser frequency is a compromise between reducing off-resonant single-photon scattering whilst maintaining sufficiently strong coupling for two-photon Raman transitions. The 780 nm laser is 50 GHz red-detuned from the Rb D_2 transition, and the 852 nm laser is 41 GHz red-detuned from the Cs D_2 transition. For the work in Chapter 6, we changed the frequency of the Cs Raman laser so that it was red-detuned by 60 GHz.

The geometry of Raman beams in Figure 2.3 allows us to couple to the motional state along the three orthogonal axes of the trap. The two-photon Raman transitions are also coupling the spin states $|f = 3, m_f = 3\rangle$ and $|4, 4\rangle$ for Cs, or $|1, 1\rangle$ and $|2, 2\rangle$ for Rb. To couple to the motion along a given axis, the resultant wavevector from the combination of the two beams must have a non-zero projection along that trap axis. It should be noted that both RB1+RB2 and RB1+RB3 have a resultant wavevector with a finite projection along both radial axes (for the implications of this fact, see Section 5.2.1).

The Raman beams are focused onto the atoms to produce beam waists of

$100 - 160\,\mu$m so that modest laser powers can be used to achieve the desired Rabi frequencies. We note that a combined Raman beam power of 2 mW at the atoms is sufficient for our cooling scheme. The beams are overlapped with the atoms in turn by applying a pulse that will heat the atoms and maximising the atom loss as a function of beam alignment. An alternative method involves applying a state-selective pushout after the Raman-beam pulse to detect the single-photon Raman scattering from the beam. In both methods, the atom loss is maximised when the scattering rate is greatest, which occurs at the point of highest intensity at the centre of the beam. Since RB2 and RB3 propagate in opposite directions, we back-coupled RB3 through the fibre coupler of RB2. The efficiency of the fibre coupling gives an indicator of the beam-pointing drift over time. A quantitative measure is taken by imaging the reflected light from a polarising beamsplitter onto a CCD camera, from which we determine that the displacement of the beam doesn't drift further than $20\,\mu$m from the atoms over one month.

Figure 2.4 displays the hardware controlling the Raman beams. The 852 nm light is overlapped with the 780 nm light using a dichroic mirror so that they share hardware in the RB2, RB3, and RB4 beam paths. Frequency and power control is achieved using five AOMs. The Bragg diffraction angle of each AOM is wavelength dependent, so we must compromise the diffraction efficiency between the optimum for 780 nm and the optimum for 852 nm. Despite this, we typically achieve first order diffraction efficiencies of $> 50\%$ for both wavelengths. Electro-optic modulators (EOMs) are used to add frequency sidebands at 6.8 GHz for Rb and 9.2 GHz for Cs. To suppress the possibility of driving unwanted transitions and introducing pathways for quantum interference [172], we offset the EOM frequency by 10 MHz from the Zeeman-shifted ground-state hyperfine splitting [149] (see Section 4.2). The use of separate AOMs for RB1 (AOM1a for Cs and AOM1b for Rb) allows for independent control over the two-photon detuning and Rabi frequency of each species. However, sharing AOMs means that the pulse durations of RB2, RB3, and RB4 are constrained to be the same for both wavelengths.

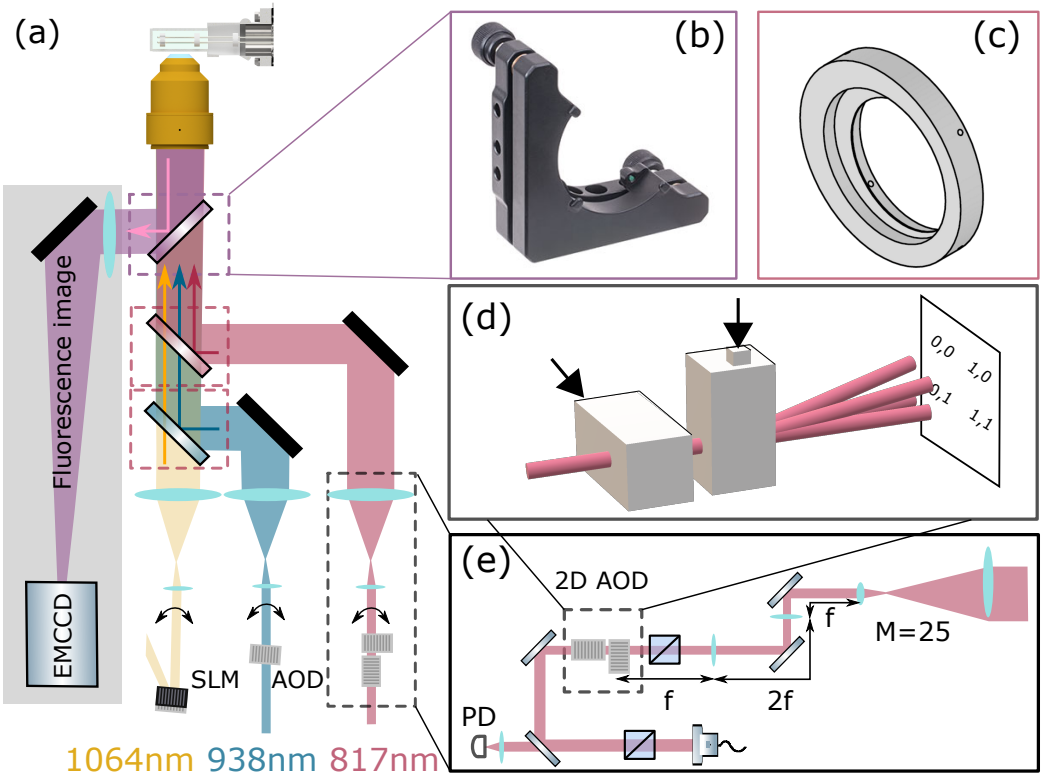

Figure 2.5: Tweezer and imaging optics on the main experiment table. (a) The high-NA lens collects atomic fluorescence, which is focused down by an achromatic lens onto the EMCCD. Optical tweezers at wavelengths of 1064 nm, 938 nm and 817 nm are magnified then overlapped using dichroic mirrors before they enter the high-NA lens. Each tweezer has its own beam-steering hardware. (b) The first dichroic mirror is clamped into a clear-edge mount. All the tweezer beams are transmitted. (c) The second and third dichroic mirrors are glued into custom-made 3" adaptors in order to reduce the stress from clamping. (d) Separate RF signals drive the first and second AOD to deflect the 817 nm tweezer in the horizontal and vertical directions respectively. (e) The optics for the 817 nm tweezer path. Polarisers set linear polarisation before and after a pair of AODs oriented orthogonally (2D AOD). A 4-f optical relay images the vertical AOD onto the first lens of a telescope that magnifies the beam size by 25×.

Optical Tweezer Lasers

The wavelengths of the lasers used for the optical tweezer traps are chosen so that they form species-selective trapping potentials [87, 97, 98]. 1064 nm is far red-detuned from both the Rb and Cs D_1 and D_2 transitions, such that it can form attractive potentials for both species and the scattering rate from the tweezer is insignificant over the timescales of our experiments. 938 nm is also red-detuned for both species, but its proximity to the Cs D_1 transition at 895 nm means that the polarisability for Cs atoms is $\sim 3\times$ the Rb polarisability. 817 nm is red-detuned for Rb, but blue-detuned from the Cs D_1 and D_2 transitions, such that it provides a repulsive potential for Cs atoms. Use of these tweezers for species-selective trapping has been discussed elsewhere [98, 164]. Since that work, there have been a few changes to the optical tweezer lasers. The later chapters of this thesis make use of different lasers with wavelengths near to 1064 nm. Also, we increased the operating current for the laser diode used to generate the Rb optical tweezer, and as a side effect the wavelength changed from 814 nm to 817 nm.

The original 1064 nm tweezer laser source was an Azurlight systems ALS-IR-1064-10-I-CC-SF at 1064.0 nm. The experiments in Chapter 6 also used a Coherent Mephisto at 1064.5 nm which seeds an Azurlight ALS-IR-1064-30-A-SF amplifier, and a Thorlabs DBR1064PN with tunable wavelength from 1063.5 nm up to 1065.5 nm.

The reason for changing the current of the 817 nm laser diode was to improve the single-mode character of its output. We noticed a consequence of multi-mode behaviour when examining the output of the 8 m optical fibre that couples light from the laser table to the main table. Unless the diode is operating in a particular single-mode regime, fast polarisation noise appears on the laser after it has passed through the optical fibre when the optical power fed into the fibre is above a threshold of ~ 7 mW. It is likely that this is modal noise as a result of interference between multiple modes propagating through the fibre [173, 174], although it is unexpected for single-mode polarisation-maintaining optical fibres. The polarisation noise is broadband, and is converted to intensity noise by a polariser after the fibre output, which then noticeably reduces the lifetime of atoms trapped in the tweezer. We set

the current of the 817 nm and the 938 nm laser diodes by minimising the intensity noise observed after a polariser on the output side of their respective optical fibres.

Main Table Tweezer Optics

The main table tweezer optics displayed in Figure 2.5 are designed to magnify the tweezer beams so that they fill the clear aperture of the high-NA lens, minimising the tweezer waist. The figure focuses on changes that were implemented in February 2022, after most of the work in Chapter 5. In particular, we changed the mounting of the dichroic mirrors[1] in order to increase their clear aperture.

Our aim in changing the optics setup was to decrease the beam waist of the optical tweezer traps by increasing the size of the beams entering the high-NA lens. Smaller waists are beneficial as less power is required to create a potential of the same depth, an important consideration for the prospects of scaling up to an array. One might think that the minimum waist for the tweezer traps is limited by the 30.6 mm wide rear aperture of the high-NA lens. However, overfilling the aperture still reduces the beam waist at the focus, albeit with the consequence that the focused Gaussian profile transforms into an Airy disk. Theoretical calculations using Zemax OpticsStudio predict that beam diameters of > 40 mm entering the high-NA lens are required in order to achieve a near-diffraction-limited waist at the focus. Unfortunately, the clear aperture of the 2" dichroic mirrors in the tweezer beam paths is reduced to 35 mm in the horizontal direction in which they are tilted at 45° (limiting w_x). In the initial setup, the horizontal clear aperture was further reduced by the mounts holding the dichroics. All of the dichroic mirrors used to overlap tweezer beams were held in threaded mounts and secured by a retaining ring, which ensures a uniform distribution of pressure across the surface of the mirror. The pressure must be applied uniformly to avoid stress-induced curvature of the dichroic mirror which adds astigmatism to

[1]The first dichroic has a custom coating from LaserOptik which reflects 780 nm and 852 nm, but transmits 800-820 nm and > 930 nm. The second dichroic is a long-pass with 900 nm cut-on wavelength: Thorlabs DMLP900L. The third dichroic is a long-pass with 950 nm cut-on wavelength: Thorlabs DMLP950L

the reflected beam by preferentially focusing one axis over the other [164]. However, the drawback of this mount was that it has a lip which clips both reflected and transmitted beams, reducing the clear aperture to $\sim 25\,\text{mm}$. Therefore, we decided to implement a clear-edge mount (Thorlabs KM2CE) as shown in Figure 2.5(b). This mount allows use of the full 35 mm width of the mirror, but it uses two grub screws to secure the mirror which apply concentrated stress. The resulting astigmatic aberration is not an issue for the imaging light reflected off the first dichroic, but would increase the waist of tweezer traps.

To avoid adding aberrations to the tweezers, we designed a custom adaptor to mount the dichroics which reflect tweezer beams, displayed in Figure 2.5(c), viewed from the rear. The inner radius of the hole is 0.5 mm less than the radius of the mirror to provide a lip for the mirror to rest on. The outer radius is 1 mm greater than the radius of the mirror, and this gap is filled with UV-cure glue to secure the mirror in place. The glue is equally distributed around the circumference by piping it through four holes in the exterior edge of the mount. A cylinder is cut out of the back of the adaptor to ensure that the thickness of the adaptor doesn't limit the clear aperture. The adaptor is held in a standard 3" lens mount. These custom mounts should achieve a 34 mm clear aperture without adding curvature by stressing the dichroic. In practice, after carefully positioning and aligning the three dichroic mirrors, we find that the tweezer beams are apodised to a diameter of $\sim 30\,\text{mm}$ in the horizontal direction. Furthermore, after using a cylindrical lens to correct astigmatism in the 938 nm tweezer beam path, we find that oblique astigmatism is present on the focused beam. This suggests that either the UV-cure glue was not uniformly distributed around the dichroic, or that another mirror in the beam path has significant curvature. In the future, the oblique astigmatism could be corrected using a rotating mount to set the angle of the cylindrical lens. The results of changing the mounts and re-aligning the tweezers are presented in Chapter 3.

2.1.5 Acousto-Optic Deflectors

Acousto-optic deflectors (AODs) are now a popular method for controlling the position of optical tweezers [4, 31, 52, 74, 92, 145]. Using a 2D AOD is an even more attractive prospect as it provides an extra dimension for dynamic control over an array of atoms [3, 94, 97, 175, 176]. In our experiment an AOD in the 938 nm tweezer beam path (IntraAction ATD-1803DA2.850) is used to create arrays of Cs atoms and translate the tweezer position along the x-direction. Similarly, a 2D AOD in the 817 nm tweezer beam path (AA Opto-Electronic DTSXY-400-810) is used to create arrays of Rb atoms and translate the tweezer position in the xy-plane. The principle of operation has been discussed in detail in the context of our first AOD [164]. Briefly, the deflection angle of the beam exiting the AOD is proportional to the frequency of the RF signal input into the AOD [177]. The following section describes the characterisation of the newly-installed 2D AOD. Of particular interest is understanding how the RF signals driving the AODs determine the diffraction efficiency, with the aim of creating an array of tweezers with uniform intensity.

Figure 2.5(d) displays the basic operation of the 2D AOD. It is composed of a pair AODs which are mounted such that they deflect the input beam in the horizontal (x) and vertical (y) directions respectively. Two separate RF signals control the deflection angle. The signals are sourced from arbitrary waveform generators (AWGs, see Section 2.2.7) which feed 35 dB amplifiers (AA Opto-Electronic AMPA-B-34-20.425). In the following discussion we refer to the amplitude of the RF signal output by the AWG; before it is amplified. The deflection angle is proportional to the frequency of the RF signal. A piezo-electric transducer is bonded to each AOD crystal at an angle such that the Bragg condition [178] is met for an incident beam at normal incidence to the input face. The result is that the first diffracted order from both AODs (1, 1), henceforth called the first order beam, is colinear with the input beam when driving the AODs at their centre frequencies of ~ 100 MHz. An iris blocks the beam paths from other combinations of orders of diffraction as we are interested only in the first order.

The setup in Figure 2.5(e) includes an optical relay system and polarisation

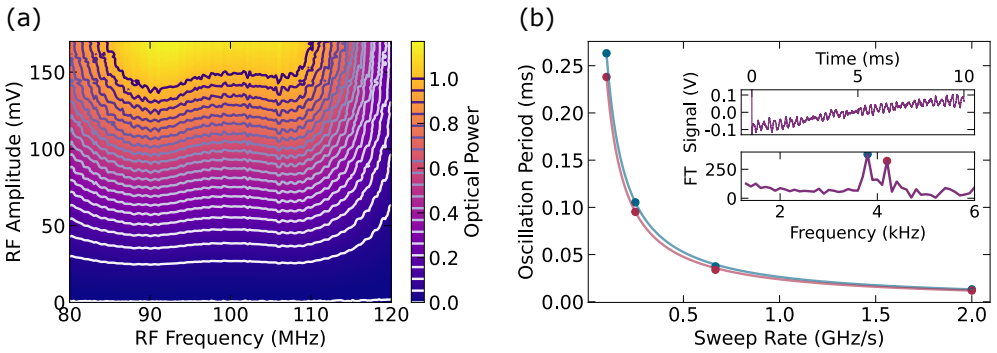

Figure 2.6: The diffraction efficiency of the 2D AOD used for the 817 nm tweezer varies with the driving frequency. (a) For a chosen frequency driving the horizontal AOD, we find the RF amplitude required to reach the contours of constant optical power. (b) Linearly sweeping the horizontal AOD's driving frequency reveals oscillations in the diffraction efficiency. The inset shows the AC component of a photodiode signal and its Fourier transform when sweeping the frequency 1 MHz in 10 ms (0.1 GHz s^{-1}). Oscillations at two distinct frequencies are observed, plotted in blue and red. The oscillation period is inversely proportional to the sweep rate.

correction. A 4-f optical relay images the vertical AOD onto the first lens of the magnifying telescope such that deflections from the AOD are refocused, preventing aberrations associated with lens curvature when the incident beam is displaced from the optical axis. The relay targets the vertical AOD since this is the direction we plan to move 817 nm tweezers during an experimental sequence and the aberrations would modify the desired trajectory. It is important that the tweezer beams have linear polarisation in order to avoid deleterious effects from vector light shifts, as discussed in Chapter 5. After the work in Chapter 5, we inserted a polariser after the 2D AOD that cleans up the polarisation without significant effect on the power.

Figure 2.6(a) displays a contour map of the 2D AOD's diffraction efficiency as a function of the frequency and peak amplitude of the RF signal driving the horizontal AOD. We evaluated several methods of measuring the diffraction efficiency and found that the quickest was to drive the AOD with a single tone signal that takes 10 ms steps between a randomised list of 120 different amplitudes. A data acquisition device measures the output power using a photodiode in the first order beam and tracks the variation of optical

power. The process is repeated at 160 different frequencies and takes a total of $\sim$ 5 minutes. The reference optical output power of 1 corresponds to a diffraction efficiency of 75 % when both AODs are driven at 100 MHz with a peak amplitude of 150 mV.

If we now sweep the driving frequency of the horizontal AOD by 1 MHz we observe a periodic modulation of the diffraction efficiency. Figure 2.6(b) plots the period of the oscillations which are inversely proportional to the frequency sweep rate. The oscillation period is extracted from the Fourier transform of the photodiode signal, and the inset shows the recorded photodiode signal for a sweep rate of 0.1 GHz s^{-1}. The amplitude of the oscillations is $\sim$ 2 % of the optical output power. For reference, similar measurements using the AOD in the 938 nm tweezer beam path had oscillations with $\sim$ 1 % amplitude [164]. The modulation is explained by the AOD crystal acting as an etalon as a result of acoustic standing waves [179–181]. The AOD uses Bragg diffraction from a travelling acoustic wave that periodically modifies the refractive index of the crystal. Reflections from the opposite face of the crystal allow detrimental interference between forwards-propagating and backwards-propagating acoustic waves, observed as periodic modulation of the diffraction efficiency as the wavelength of the acoustic wave varies relative to the cavity length. Figure 2.6(b) clearly demonstrates beating between two similar frequencies, suggesting that there are two relevant cavity lengths. Using the speed of sound in the crystal, $v_\mathrm{s} = 617\,\mathrm{m\,s^{-1}}$, the cavity length is given by $L = v_\mathrm{s}/(2\nu_\mathrm{FSR})$ where the cavity free spectral range is $\nu_\mathrm{FSR} = d\left(\frac{dF}{dt}\right)/df_\mathrm{osc}$ for sweep rate $\frac{dF}{dt}$ and oscillation frequency f_osc. For the horizontal AOD we calculate cavity lengths of 11.73(4) mm and 12.97(5) mm. Repeating the measurements for the vertical AOD we calculate cavity lengths of 11.38(4) mm and 12.70(10) mm. These lengths are roughly consistent with the internal dimensions of the AOD crystal and the $\sim$2 mm deep absorber bonded onto the far face.

To create an array of tweezers, we drive an AOD with a multitone RF signal $\sum_{k=1}^{N} a_k \sin(2\pi f_k t + \phi_k)$ where the phase offset ϕ_k, frequency f_k, and amplitude a_k of each tone k are all important independent variables. First we consider the effects of the relative phases. Nonlinearities in the amplifier and AOD lead to frequency mixing and result in destructive interference [4, 145,

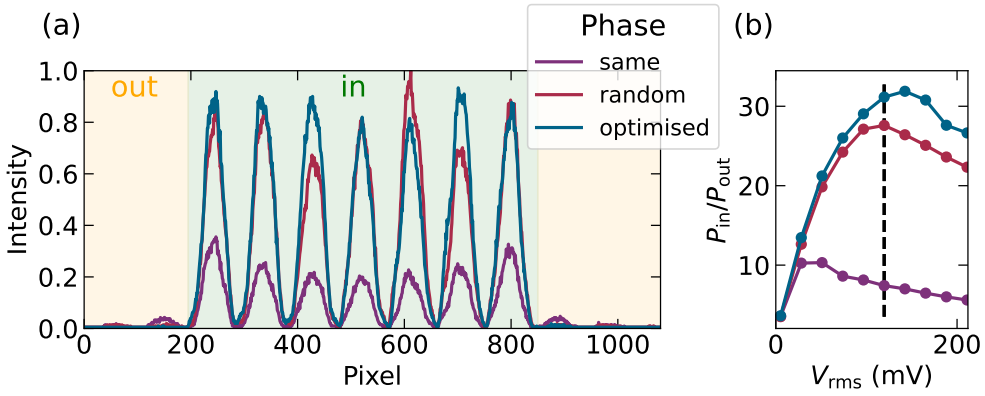

Figure 2.7: Effect of nonlinear mixing on a 1D array of 7 traps. (a) Slices of images when the RF signal into the 2D AOD's amplifier has $V_{\mathrm{rms}} = 120\,\mathrm{mV}$ (dashed line in (b)). When all tones have the same phase, frequency mixing in the amplifier causes destructive interference. (b) Ratio of the optical power inside (green region in (a)) relative to outside (yellow region) the desired array. Power in the array increases with the input amplitude up to the amplifier's saturation point where nonlinear effects cause frequency mixing. Optimising the phases of the tones minimises interference effects.

182, 183], as can be seen in the slices of images displayed in Figure 2.7(a). A 1D array of seven traps is imaged onto a CCD camera, and we observe the change in optical power as the phases of the tones are adjusted. The destructive interference occurs when frequency mixing creates sum and difference tones ($f_i \pm f_j$) which can then mix with the original frequencies (e.g. $f_i \pm (f_i - f_j)$). The finite power bandwidth of the amplifier is a contributor to the frequency mixing, therefore the destructive interference is increasingly deleterious as the input signal reaches or surpasses the amplifier's saturation point. When all of the tones have the same phase it is considerably more likely that their antinodes coincide and the multitone signal exhibits an instantaneous amplitude spike above the saturation point. Randomly generating the phases means that difference tones from intermodulation almost completely cancel each other out [182], and there is a significantly lower probability of instantaneous amplitude spikes. The difference can be quantified by the crest factor, defined as $\max(V)/V_{\text{rms}}$ for a periodic signal V [184]. The minimum crest factor is $\sqrt{2}$ for a single tone. With equal phases the crest factor is 3.7, compared to 2.5 for randomised phases and 1.8 for optimised phases. To optimise the phases, we start with an analytical formula, $\phi_k = \phi_1 - k(k-1)\pi/N$ for tones $k = 1$ to N, and then perform numerical optimisation of each phase in turn to minimise the crest factor [184–186]. The difference is seen in Figure 2.7(b) by measuring the optical power in the array (the green highlighted region in Figure 2.7(a)), and comparing it to the power outside the array (yellow highlighted region in Figure 2.7(a)). Each line has three regions as the input RF amplitude is increased: initially the optical power increases, then it hits a saturation point, finally the power is diverted outside of the array. The saturation point is determined by the instantaneous peak amplitude rather than the RMS amplitude. Therefore, in Figure 2.7(b) the saturation points for the three lines differ by approximately the crest factors. The relative trap powers vary by $\sim 10\,\%$ after optimising the phases and setting the RF amplitude below saturation, but this can be further improved upon.

The next adjustment to balance the trap powers in the array is iteratively optimising the amplitude of each tone in the RF signal. Figure 2.8 displays the results of our normalisation protocol for a 1D array of 4 traps generated

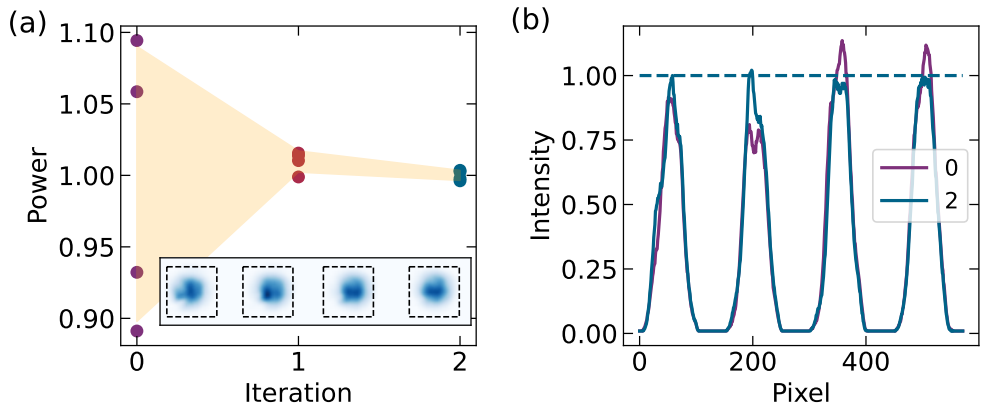

Figure 2.8: Balancing a 1D array of 4 traps using a CCD. (a) The standard deviation of the trap powers is 10 % when interpolating the diffraction efficiency calibration and optimising the phases. Optimising the amplitudes of the RF tones individually we normalise the trap powers to 0.4 % in two iterations. Inset: a CCD image of the 4 traps. (b) Slice of the images before (purple) and after (blue) the normalisation.

with frequencies separated by 4 MHz. We quantify the trap powers by taking a CCD image and integrating the pixels in a region of interest (ROI) around each trap. The inset of Figure 2.8(a) shows the final CCD image with dashed lines marking the ROIs. The measured powers are used to calculate a new set of amplitudes, and the process is iterated until the measured powers converge. Typically only a few iterations are required because in this regime there is an approximately linear relationship between the driving amplitude and the trap power. In Figure 2.8(a) the yellow shaded region is a guide to the eye, showing that the spread of powers reduces with each iteration. After two iterations the trap powers have a standard deviation of 0.4 % of the mean. Figure 2.8(b) plots the central slice of the images from iteration 0 (before normalisation) and iteration 2 (after normalisation). This normalisation method is scalable and can balance 2D arrays, although the precision is then limited by the interdependence of trap powers. For example, a 4×4 array has 8 amplitudes with which to control the power of the 16 individual traps. This is not an issue for a 1D array, and applying the normalisation process we typically balance the powers to $\lesssim 1\,\%$.

2.1.6 Spatial Light Modulator

The spatial light modulator (SLM) has become a popular tool in atomic physics for the flexibility with which it can manipulate light [78, 81, 89–91]. Of particular interest is the possibility of creating arrays of tweezer traps [78, 81, 82]. Deterministic preparation of arrays has been demonstrated using AODs to rearrange atoms amongst the static traps of the SLM [3, 97]. In this work, we use a liquid crystal SLM (PDM512-1064-DVI standard XY series) to generate a single trap with a reduced beam waist by removing aberrations [187, 188] (see Section 3.1.3). But first, we will introduce the basic principles of operation.

The SLM applies an arbitrary phase pattern to light reflected off it, acting as a combination of optical elements [189]. Classical optics apply a phase to light passing through them, but diffractive optical elements accomplish the same phase shift by making use of the 2π periodicity [190]. The SLM has an array of 512×512 pixel electrodes which modify the refractive index of a liquid crystal. Light reflected off the SLM passes through the liquid crystal and has a spatially-dependent phase imprinted on it. The next step is to determine what phase pattern (also called a kinoform) applied to the SLM will achieve the desired beam shape in the Fourier plane at the focus of the high-NA lens.

For some particular optical elements there is an analytical formula for the required kinoform. The optics of relevance to this work are: the Fresnel lens for shifting the tweezer focus in the axial direction; the diffraction grating for shifting the tweezer in the transverse plane; and the set of Zernike polynomials which describe aberrations. Fortunately, analytical formulas exist for all three. However, this is not the case for generating an array of tweezer traps. In general, the required kinoform can be found using an iterative Fourier transform algorithm such as the Gerchberg-Saxton algorithm [191–193]. Having constructed the required kinoforms, they are summed modulo 2π and uploaded to the SLM, which then acts as the combination of the optical elements.

In future work, the SLM will be used to create arrays of traps. Less total laser power is required for the array if the tweezers can be focused to a

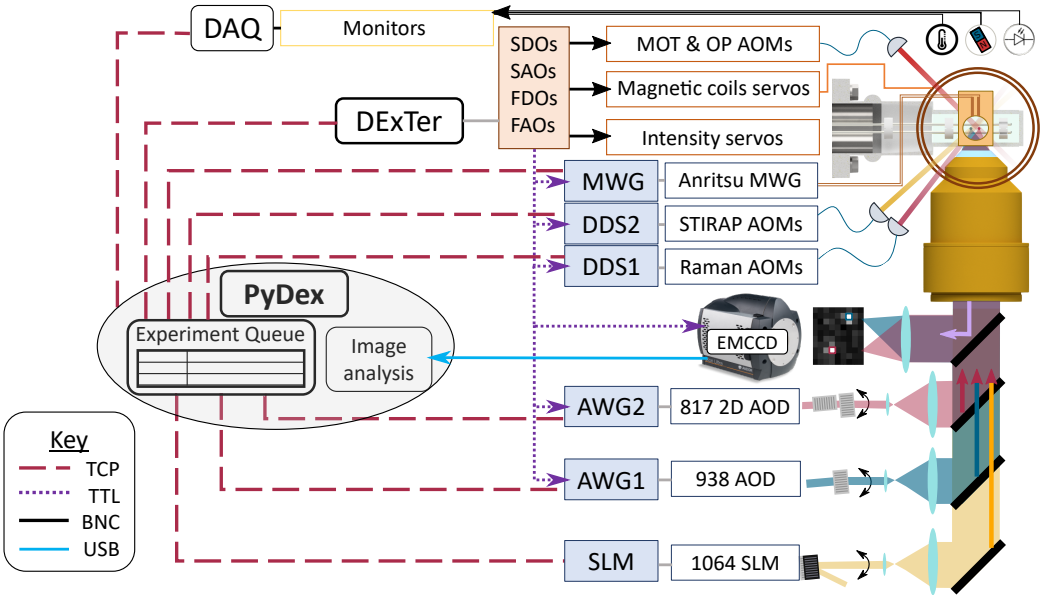

Figure 2.9: Connections between experimental control software and hardware. The PyDex script manages experiments by sending TCP messages over the network to applications running on separate computers.

smaller spot. Therefore the telescope after the SLM was modified to provide a magnification of 5.3× such that the expanded beam diameter is 31 mm, reducing the focused waists by using more of the available clear aperture.

2.2 Software and Electronics

Ultracold atom experiments require precise, reliable, and synchronised control over hundreds of output channels operating the experimental hardware. Furthermore, the control system must be flexible and adaptable to future expansion. To meet these aims, most labs develop their own experimental control software and combine it with analysis and data logging [194–202]. It is common for these programs to have a branching structure where a central hub communicates with modules over the local area network (LAN). Following a similar principle, Figure 2.9 gives an overview of the hardware and software used in our laboratory. A master application written in Python, PyDex[2], receives images from the EMCCD during the repeated running of

[2] `https://github.com/ssquantum/PyDex`.

experimental sequences and performs real-time image processing and statistical analysis. PyDex also coordinates a range of modules hosted on other computers, dictating the parameters to load for the experiment. The first module is DExTer [203], an experimental control interface written in LabVIEW that programs an FPGA (National Instruments PCI-7833R) with 24 analogue output and 72 digital output channels. Additional modules are developed mostly from commercial APIs to interface with a data acquisition device (DAQ), a microwave generator (MWG), two direct digital synthesisers (DDS), two arbitrary waveform generators (AWG), and a spatial light modulator (SLM). These modules will be discussed in turn.

2.2.1 Experiments Managed by PyDex

In our control system, PyDex is the central hub. The PyDex user interface (UI) uses PyQt5 bindings [204] to create a series of windows for queuing up experiments and displaying results. The procedure for running an experiment is as follows:

1. The user sets a list of parameters (we might change more than one parameter at a time) and metadata using the PyDex UI, then adds the experiment to a FIFO queue. All other steps are automated by PyDex.
2. When the hardware is available, pop an experiment from the queue.
3. Send messages to the modules to load the first set of parameters.
4. Each module, including PyDex, saves its parameters to a text-based file.
5. Wait for the modules to confirm the parameters have loaded.
6. Tell DExTer to run N repeats of the sequence and process the images taken in each run.
7. Perform statistical analysis on the histogram generated from the image processing and save the results in CSV format.
8. Iterate steps $3-7$ through the parameters in the list.

In this scheme, DExTer runs the sequence so that the timings are synchronised to the FPGA's 80 MHz system clock. The other modules follow the

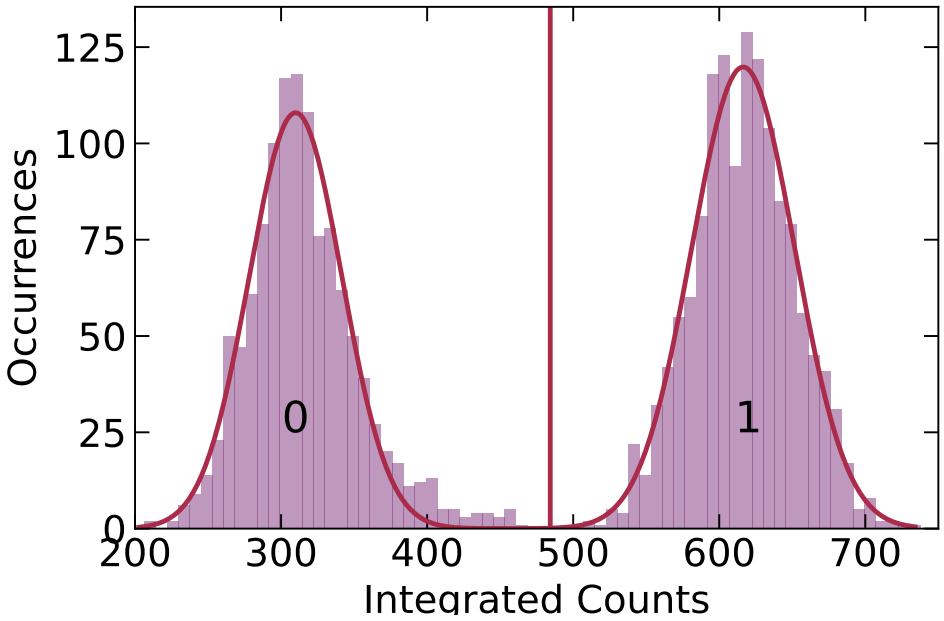

Figure 2.10: Histogram establishing the bimodal distribution of tweezer trap occupation from a collection of 2555 images. A threshold is assigned by finding a minimum between the two peaks.

sequence using external transistor-to-transistor logic (TTL) triggers from DExTer's digital output channels.

2.2.2 Image Analysis

Each run of a sequence takes images from the EMCCD which are distributed to image-processing functions using the Qt signal-slot architecture. The image signal is received by separate analysis windows that are instantiated with user-defined ROIs around the position of an atom in the image. The counts in the pixels within the ROI are summed to give a signal which is distributed around a background mean value if there is no atom in the ROI, or a higher value if there is an atom.

In Figure 2.10 we establish the probability of an atom being present by creating a histogram of the integrated ROI signal. A threshold is set which distinguishes the peaks of the histogram's bimodal distribution using a minimum method [205]. In practice, the power and detuning of the imaging

beams along with the duration of the image are chosen to give a separation of the peaks much greater than their width. Furthermore, we apply an EM gain factor of 10 to increase the signal-to-noise ratio despite the presence of additional multiplicative noise [59, 206, 207]. We define the image threshold infidelity as the probability of assigning either a false positive or a false negative. Typically the infidelity is $\sim 10^{-4}$ and we assign a fixed threshold to avoid miscalculating the threshold when there are no atoms and the histogram only has the background peak.

PyDex uses threads to prevent looping or slow functions from blocking UI updates. For example, the EMCCD acquisition includes a blocking function that waits for an image to be acquired. Spawning a thread for the blocking task to run in the background allows the main thread (including the UI) to progress simultaneously. Threads are also used for communication over the LAN, where a server must always be ready to receive a connection from a client.

2.2.3 Network Communication

Our experimental control follows a modular design using network communication to integrate applications running on separate computers. Distributing the applications across separate processors make better use of the available computing power, and the modularity facilitates future expansion. PyDex hosts a set of servers that send messages to the applications displayed in Figure 2.9 using the transmission control protocol and internet protocol (TCP/IP), which have the benefit of being platform agnostic and correcting for most data transmission loss. A client running on the application connects to the server on a specific port so that messages from other sources are not intercepted (this is an important security measure). TCP messages typically take $\sim 1 - 10\,\text{ms}$ to transfer, depending on the message size. To allow cross-platform readability, the experimental sequences are saved and sent in TCP messages using a verbose XML format, but PyDex uses an etree [208] to speed up read/write access. Parsing sequences with many time steps can still take up to $\sim 500\,\text{ms}$, but this action only occurs for the first repetition of an experiment.

2.2.4 Monitoring

Monitoring systems are a powerful resource for cold atom experiments, especially when combined with database and networking technology [209, 210]. We create a database using InfluxDB [211] with write access for sensors over the LAN. We use sensors to monitor laser powers and environmental conditions such as the temperature at several locations, pressure, humidity, and background magnetic field. To monitor laser powers, a pick-off mirror or beamsplitter directs laser light onto a home-built photodiode circuit (based on a Centronic OSD15-5T photodiode). The photodiodes send analogue voltages to an NI USB-6211 data acquisition device (DAQ). An application displays oscilloscope-style traces, saves the traces as CSV files, and can push time-stamped records to the database by TCP messages. The temperature sensors (Maxim Integrated DS18B20), magnetic field sensor (Rohm Semiconductor BM1422AGMV), and atmospheric sensor for pressure and humidity (Bosch Sensortec BME280 mounted on a SparkFun SEN-15440 breakout board) are all connected to an Arduino which is programmed to post sensor readings to the database every 0.5 s.

Collecting data from these sensors allows us to record correlations between experimental measurements and environmental conditions. The temperature and humidity oscillate with a period of $10 - 15$ minutes following the air-conditioning cycle. Temperature fluctuations affect the polarisation of light travelling through optical fibres and since we usually have a polariser on the output side of the fibre, we record correlated fluctuations in the laser power of typically $\sim 3\,\%$ after the polariser. Temperature fluctuations also affect beam pointing through the expansion and contraction of mirror mounts. Usually beam sizes are large enough that the change in pointing is insignificant, however, we measured strong correlation between the overlap of the 817 nm and 938 nm tweezers with the humidity and temperature of the lab. This was most likely due to the thermal stability of the piezo-actuated mirrors (PiezoMike N-470.110) in the 817 nm beam path, therefore when we inserted the 2D AOD we removed the piezo actuators and noticed a reduction in the correlation.

2.2.5 Microwave Generator

We use an Anritsu MG3692C MW generator operating with an external trigger which defines the duration of a square pulse. There are several modes of operation, but we use a single-tone mode. An application communicating over the LAN allows remote control of the frequency and amplitude for automated experiments[3]. The internal clock is referenced to an external 10 MHz GPS signal.

2.2.6 Direct Digital Synthesiser

A home-built DDS rack based on the Anologue Devices AD9910 chip is used to drive the AOMs for the Raman beams. A second rack will drive the AOMs used in the STIRAP optical setup, which does not feature in this thesis. Each AOM is driven by a separate DDS, but the DDS boards are mounted together in a rack. The DDS boards are programmed using a serial USB connection.

Our custom firmware implementation has two modes of operation. The first mode is used for RB1 to switch between a choice of 8 static tone profiles with a set frequency, phase, and amplitude. A delay of ~ 200 ns sets the minimum switching time. The first profile is reserved as an off state, allowing us to generate square pulses. The second mode is used for RB2, 3, and 4; the frequency is fixed and a playback of preloaded data provides the dynamic amplitude control required to create a shaped pulse. In the second mode, we have a choice of 8 pulse durations and we can also specify which section of the loaded data to playback. In both modes the frequency can be set with Hz-level precision. Although the output spectrum suffers from aliased images, these appear at beat frequencies (of the desired frequency with the clock frequency of 1 GHz) [212] and are too fast to influence the atoms in our experiments. We are more concerned with noise that is $\sim 10 - 100$ kHz from the carrier, which is mostly associated with jitter in the clock reference [213]. The DDS circuit is referenced to an external 10 MHz GPS signal with a bandwidth of 2 Hz, however the internal multiplication up to the 1 GHz system clock frequency adds phase noise and narrowband frequency noise

[3] `https://github.com/danruttley/mwcontrol`

[213]. The investigation of dephasing mechanisms for Raman transitions in Chapter 5 proves that the spectral purity of the DDS output is sufficient for our purposes.

2.2.7 Arbitrary Waveform Generator

The RF signals driving the 938 nm and 817 nm tweezer AODs are generated from two AWGs which we name AWG1 and AWG2 respectively. AWG1 is a Spectrum Instrumentation M4i.6622-x8 card with a sample rate of $625\,\mathrm{MS\,s^{-1}}$ and we only use the first of the four available output channels. AWG2 is a Spectrum Instrumentation M4i.6631-x8 card with a maximum sample rate of $1.25\,\mathrm{GS\,s^{-1}}$, but we set the sample rate to $1.024\,\mathrm{GS\,s^{-1}}$ so that 1 kB of data executes in $1\,\mu$s. The first channel of AWG2 drives the horizontal direction of the 2D AOD, and the second channel drives the vertical direction.

An object-oriented program was written to act as external memory, communicate with PyDex, and interface with the cards.[4] The cards are connected to the PCIe slots of separate computers, which run instances of our program. The program precomputes waveforms for the AWG to playback and stores them in computer memory when there is insufficient memory on the card. Having additional memory storage is particularly important for rearrangement schemes where there are many permutations of trap movements. A UI made with PyQt5 [204] allows the user to upload data to the card and change settings. Using TCP messages, the AWG program acts as a proxy between PyDex and the AWG card.

The Spectrum Instrumentation API allows several modes of operation but our implementation uses the sequence replay mode. This mode splits the card memory into a predefined number of segments, N_{seg} which hold data up to a maximum size of $2\,\mathrm{GS}/N_{\mathrm{chan}}/N_{\mathrm{seg}}$, where N_{chan} is the number of active channels. A separate sequence memory dictates the order to playback segments in a series of steps. Each step defines: a unique index, the segment to playback, the number of loops, the exit condition (continue to the next

[4] Our original implementation can be found at `https://github.com/ssquantum/PyDex/tree/master/awg` but a reboot is in development and can be found at `https://github.com/danruttley/awg`

step or loop until an external trigger is received), and the index of the next step. We create arrays of tweezers, move them around, and turn them on and off by filling the AWG segments with appropriate waveforms and forming a sequence from a list of steps.

We generate data for the segments by constructing sinusoids with time-dependent amplitudes and phases. The waveform for a tweezer array requires a sum over tones, i, which have an independent amplitude a_i, frequency f_i, and phase offset ϕ_i: $\sum_i a_i \sin(2\pi f_i t + \phi_i)$ where t is in the discrete set of time steps defined by the sample rate. We choose amplitudes which normalise the optical power by constructing a calibration from the measured diffraction efficiency as a function of RF frequency and amplitude. The measured contours are interpolated to create an inverted rectangular mesh where the frequency and optical power are the independent variables. Interpolating the inverted rectangular mesh provides a calibration between the desired optical power and the required RF amplitude at a given frequency. The calibration is also used to maintain constant power while moving tweezers. Dynamically moving the tweezers requires the time-dependent phase to have a time-dependent derivative: $\phi_i(t) = 2\pi \int_0^t f_i(\tau) d\tau$. The time-dependent frequency $f_i(t)$ is used to calibrate the required amplitude $a_i(t)$ at each time step. The amplitude can also be set to zero to turn the trap off for a well-defined period of time. Alternatively, we can ramp the trap power adiabatically to maintain the atom's motional state. With these different functions we have the required tools for manipulating the tweezer traps.

A final important consideration when playing segments of data involves removing phase slips when looping data. The finite memory storage available on the card makes looping data an essential requirement. However, a phase slip occurs when a non-integer number of periods are sampled by the segment data, such that there is a discontinuity between the phase at the end of one segment and the beginning of the next segment. Looping over the phase slip adds components to the Fourier spectrum with frequencies determined by the duration of the segment. Usually the segment durations are on the order of $10^{-6} - 10^{-3}$ s, meaning that the frequencies are comparable to trapping frequencies and can cause parametric heating. Even without causing parametric heating, the broadening of the Fourier spectrum results in a dithering

of the tweezer position. Then the time-averaged potential experienced by the atom has a broadened spatial extent. The solution is relatively simple; when looping segments of data we choose frequencies and durations such that the data samples an integer number of periods. Even when the segments are not looped, in our current work we adjust the phase offset to maintain phase continuity between segments.

Chapter 3

Single Atom Control

We now turn to discuss the use of our apparatus for the control of single atoms. Our experimental sequences follow the generic structure of loading an atom, imaging to detect its presence, performing state preparation, manipulating the atom, and then finally re-imaging to test if the atom remains trapped. This chapter focuses on the initial stages of loading an atom into a tweezer and preparing a particular hyperfine spin state.

3.1 Loading an Atom

We start by confining a cloud of atoms in a magneto-optical trap (MOT) then performing sub-Doppler cooling. The MOT relies on a magnetic field gradient Zeeman-shifting the energies of atoms displaced from the centre of the trap, such that atoms positioned away from the centre of the trap are shifted into resonance with the laser beam propagating towards the centre (on a transition determined by the laser's polarisation) [214]. The cycle of absorption and emission of photons then provides a scattering force directed towards the centre of the trap and on average reduces the kinetic energy of the atom. We cool atoms in the MOT for $\sim 100\,\mathrm{ms}$. The typical temperatures in the MOT are $\sim 100\,\mu\mathrm{K}$, but we can achieve more efficient loading into the optical tweezer trap if the temperature is further reduced. Therefore, we subsequently turn off the quadrupole coils and make the MOT beams further red-detuned to perform sub-Doppler cooling in optical molasses [169, 215].

Applying sub-Doppler cooling for $\sim 20\,\text{ms}$ cools the atoms to a temperature of $\sim 15\,\mu\text{K}$. Atoms loading into the tweezer trap undergo light-assisted collisions such that when the incident light is turned off and the cloud of atoms falls away under gravity, the trap occupancy is limited to either one atom or none [72].

We use a species-selective protocol for loading two different species of atom [87, 94, 97, 98]. The 817 nm optical tweezer is attractive for Rb atoms but repulsive for Cs atoms. On the other hand, the Cs atom has a polarisability in the 938 nm tweezer which is $2.8\times$ greater than that of the Rb atom. By choosing appropriate tweezer powers we are able to selectively load a Cs atom in the 938 nm tweezer and a Rb atom in the 817 nm tweezer [98].

We choose a sequential loading scheme that first loads a Rb atom, then the Rb MOT is dispersed and a Cs atom is loaded from a Cs MOT. This simplifies the alignment procedure of each MOT to the appropriate tweezer trap by allowing us to use different shim fields for each species. Furthermore, we eliminate the probability of loading a Rb atom into the 938 nm tweezer.

It is beneficial to increase the loading efficiency. The loading process is stochastic; an atom is loaded into the tweezer with probability ~ 0.5. To reduce statistical uncertainty in the experimental results, we run each sequence on the order of 100 times. Fewer repeats are required if the loading efficiency is increased. Greater loading probabilities might be achieved using techniques such as Λ-enhanced grey molasses [73–75], provided that significant alterations to the laser cooling system can be made. Alternatively, one can stochastically load an array of $2N$ traps and then rearrange their positions to form the desired array of N occupied traps.

3.1.1 Rearrangement

Rearrangement permits near-deterministic initialisation of an array of occupied traps. The basic principle is to image a stochastically-loaded array, then move the occupied traps into the desired pattern, removing entropy in the process. A range of possible implementations exist. One could translate atoms in optical lattices [2, 64], dynamically change the phase pattern on an SLM [82, 216], reduce the separation between traps generated by an AOD

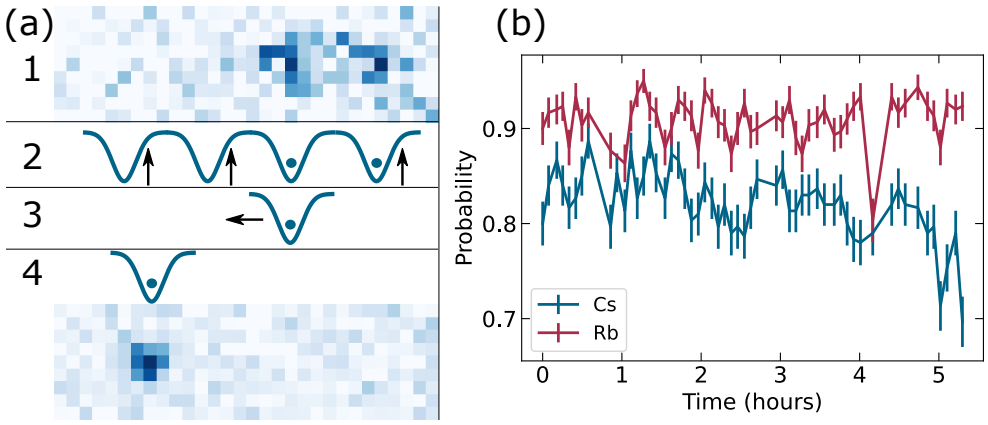

Figure 3.1: Rearrangement of stochastically loaded optical tweezer traps. (a) The rearrangement protocol has 4 steps: 1) an initial image determines the trap occupation, 2) all the traps are switched off except one, 3) the remaining trap is moved to a pre-determined position, 4) another image measures the trap occupation after rearrangement. (b) The rearrangement protocol is implemented simultaneously for Rb and Cs atoms. The probability of detecting an atom after rearrangement remains > 0.8 over a period of several hours.

[4, 92], or use an AOD to shuttle atoms between the sites of a static array [3, 21, 88]. Efficient algorithms are necessary for the initialisation of large arrays, however a simple procedure is sufficient in our case.

Our rearrangement procedure is outlined in Figure 3.1. The aim is to prepare a single occupied trap at a designated position. The same four-stage procedure is used to prepare either a Rb atom or a Cs atom. To start with, we create four tweezer traps by driving the relevant AOD with a multitone RF signal. Starting with more tweezers traps would be beneficial, but efficient loading requires a minimum trap depth of $\sim 0.3\,\mathrm{mK}$ and the total power available is currently limited by the onset of intensity noise, as discussed in Section 2.1.4. An initial image determines the trap occupation, and this information is sent to the AWG controller script. Secondly, the AWG controller selects one of a pre-loaded set of waveforms which start by turning off all traps except for one that is occupied. Thirdly, the AWG advances to play back a waveform that moves the selected trap to the designated target position. Finally, a second image reveals the success or failure of the procedure.

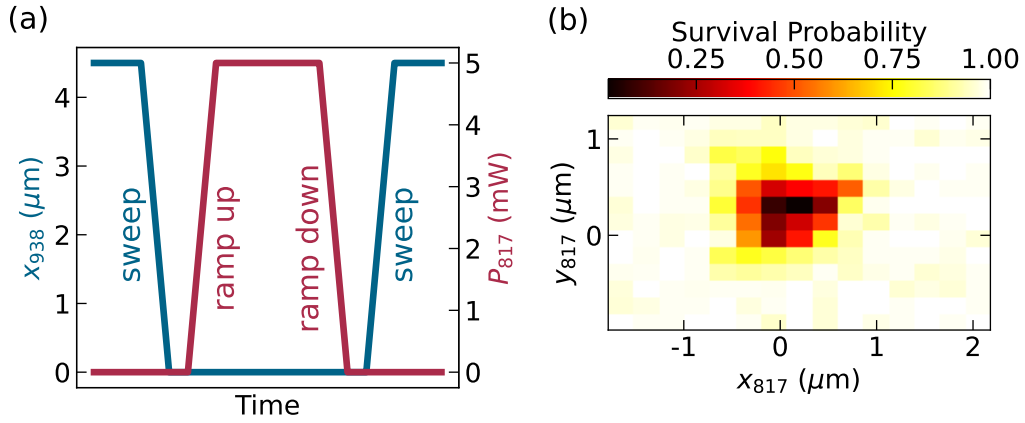

Figure 3.2: Initialising the 817 nm tweezer at different positions calibrates the overlap with the 938 nm tweezer. (a) The measurement uses the repulsive potential of the 817 nm tweezer to eject a Cs atom from the 938 nm tweezer. The 817 nm potential is only turned on after the 938 nm tweezer has been moved to a designated overlap position. (b) The 817 nm tweezer is stationary during the sequence. The probability of ejecting the Cs atom is minimised when the 817 nm tweezer is turned on at the overlap position.

Figure 3.1(b) displays the probability of detecting an atom in the second image. Each point is calculated from 300 experimental runs, and the error-bars display the binomial confidence interval using a Jeffreys prior [217]. The procedure is less effective for Cs due to a non-negligible probability of loss during imaging, as discussed in Section 2.1.4. Over a period of several hours each atom is loaded with probability > 0.8.

3.1.2 Overlapping Tweezer Positions

It is necessary to calibrate the position of the different tweezers relative to each other. We load the Rb atom and the Cs atom in tweezers that are initially separated by a distance of 4.5 μm. However, in order to associate two atoms into a molecule we must transfer them into a common trap. To avoid heating the atoms during the transfer, we must overlap the positions of the 817 nm and 938 nm tweezers to within ~ 100 nm. We experimentally determine the overlap position by ejecting Cs from a 938 nm tweezer using the repulsive potential of the 817 nm tweezer.

The sequence used to determine the overlap position of the 817 nm and 938 nm tweezers is outlined in Figure 3.2. The 938 nm tweezer is moved to a designated target position, and its power is ramped to provide a trap depth of 0.2 mK. Then the 817 nm tweezer is ramped up at a nearby position with a power that provides a repulsive barrier height of 2 mK. The repulsion is chosen to be significantly larger than the trap depth in order to eject the Cs atom; when the repulsion and trap depth are more balanced, the different spatial extent of the tweezer potentials allows the Cs atom to remain trapped in a side feature. The 817 nm tweezer is held on for 20 ms before it is ramped off and the 938 nm tweezer is swept away to re-image any surviving atoms. Figure 3.2(b) presents the results of repeating this experiment with different 817 nm tweezer positions. The survival probability is minimised when the tweezers are overlapped.

We use the SLM to position the 1064 nm tweezer at the overlap position of the 817 nm and 938 nm tweezers. The position is determined experimentally using the repulsion from the 817 nm tweezer to expel a Cs atom from the 1064 nm tweezer. The measurement follows as previously described except this time the Cs atom is transferred into the 1064 nm tweezer at a nearby position before the 817 nm tweezer is turned on. The survival probability is minimised when the 1064 nm tweezer is positioned to overlap with the 817 nm tweezer.

The aforementioned experiments can be expedited by sweeping the 817 nm tweezer. In this case the survival probability is minimised when the 817 nm tweezer sweeps through the centre of the trap. By removing one degree of freedom we decrease the required number of positions measured from $N \times M$ to $N + M$. In addition, the same survival probability is achieved for a significantly lower 817 nm tweezer power when it is swept. When comparing the different methods we found that the measured overlap positions differed by 0.19(3) μm when aligning either the x or the y direction. The most likely explanation is that the crossed AODs are not oriented perfectly perpendicular; the measured bias could be accounted for by sweeping at an angle of 89°. Regardless, neither method reveals whether the atom would be heated when merging tweezers to these positions (this is addressed in Section 5.3.1), therefore these measurements are useful as a first estimate but ultimately

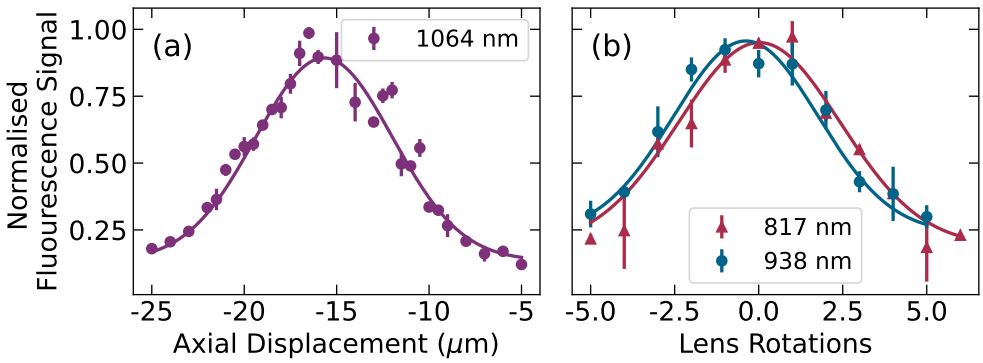

Figure 3.3: The tweezers are overlapped in the axial direction by imaging a Rb atom. By integrating the EMCCD counts in a region of interest we obtain a fluorescence signal that is maximised when the image is in focus. The focus of the tweezer is translated relative to the focus of the imaging system. (a) The SLM is used to translate the focus of the 1064 nm tweezer in the axial direction. (b) Telescope lenses are used to translate the focus of the 817 nm and 938 nm tweezers in the axial direction. 5-axis mounts hold the lenses such that one full rotation of the lens translates the focus by $\sim 2\,\mu$m.

insufficient.

In order to overlap the tweezers in the axial direction, we image the point spread function of a Rb atom after translating the tweezer focus. Figure 3.3 displays the fluorescence signal (obtained by integrating the EMCCD counts in a region of interest) as a function of the tweezer's axial position. The fluorescence signal is maximised when the images are in focus. When images of Rb atoms in the different tweezers are all in focus, it is a sign that the tweezers are positioned in the same object plane. The SLM is used to translate the focus of the 1064 nm tweezer, maximising the flourescence signal at a displacement of -15.68(6) μm, as displayed in Figure 3.3(a). For the 817 nm and 938 nm tweezers, the focus is translated in the axial direction by rotating a lens in a 5-axis mount to translate the lens axially. The effect is to make the tweezer beam either converging or diverging when it enters the high NA lens, thus shifting the focus position. One full rotation of the lens in the 938 nm tweezer beam path corresponds to a displacement of the focus position by 1.7(2) μm. After the measurement in Figure 3.3(b), the lens was

left at -0.4(1) turns, where the fluorescence signal is maximised. Similarly, a full rotation of the lens in the 817 nm tweezer beam path corresponds to a displacement of the focus position by 1.5(1) μm. After the measurement for the 817 nm tweezer, the lens was returned to its original position.

Having overlapped the tweezers, an obvious question arises: how susceptible are the tweezer positions to drifts? Vibrations might cause pointing noise, or changes in the humidity and temperature of the environment affect the mechanical stability of mounts for optics. We regularly repeated the overlap measurements over a period of several months and calculated the correlations of the results with environmental variables. The measured overlap position drifted by as much as 0.8 μm and was correlated with the mean humidity and pressure, likely due to the expansion and compression of the piezo actuators attached to a mirror in the 817 nm tweezer beam path. Therefore, we installed a dehumidifier to maintain better control over the humidity in the laboratory. Furthermore, when we installed the two-axis AOD, we removed the piezo actuators. These actions reduced the measured drift to within 0.3 μm over a period of several weeks.

3.1.3 Tweezer Characterisation

We determine the tweezer trap frequencies using parametric heating measurements. Parametric heating occurs when the trap intensity is modulated at double the oscillation frequency of an atom in the trap [218]. Figure 3.4 displays the results of experiments where the amplitude of the intensity modulation is large enough to eject an atom from the trap, either during the 50 ms of modulation or in a subsequent diabatic trap drop. In Figure 3.4(b) we measure the axial trap frequency of a Cs atom in the 1064 nm tweezer. We use the fact that arbitrary phase patterns can be decomposed into a series of orthogonal Zernike polynomials to correct optical aberrations using the SLM [187, 188]. We optimise the amplitude of one order of Zernike polynomial by measuring the effect on the axial trap frequency. This process is repeated in turn for several polynomials corresponding to the most significant aberrations in the optical system. We find optimal amplitudes $\{A[Z_2^2], A[Z_0^4], A[Z_{-2}^2], A[Z_4^4]\} =$

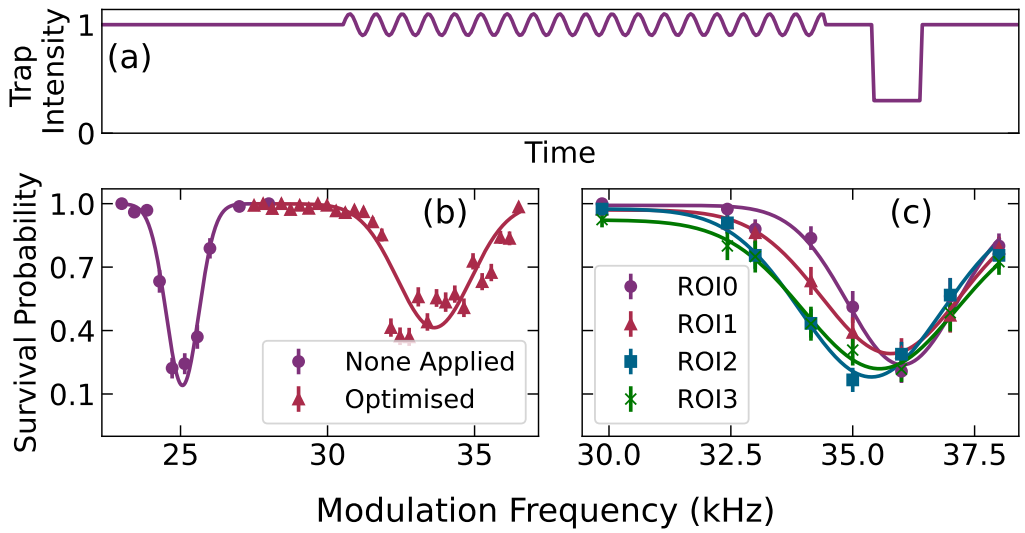

Figure 3.4: The axial trap frequency is determined by parametric heating measurements. (a) The trap intensity is modulated at a variable frequency for a duration of 50 ms. A subsequent diabatic trap drop ejects hot atoms. (b) Zernike polynomials with optimised amplitudes are added to the SLM kinoform in order to maximise the axial trap frequency of a Cs atom in a 1064 nm tweezer. (c) An array of 817 nm tweezers is used to trap Rb atoms. After using a CCD to normalise the trap powers, the axial trap frequencies are balanced to within 1 %.

$\{-0.20(2), -0.13(1), -0.087(3), 0.08(1)\}$ waves. The axial trap frequency for Cs in a 1064 nm tweezer with a power of 13 mW at the atoms was measured to be 12.54(3) kHz without any Zernike polynomials applied, which was improved to 16.81(6) kHz by the optimisation procedure. We note that the optimisation of the trap frequency does not necessarily remove optical aberrations, but it is reasonable to assume that the bottom of the potential is still approximately harmonic. We calculate an optimised beam waist of 1.19(1) μm.

When forming an array of tweezer traps it is important that their intensities are the same. Figure 3.4(c) presents the results of a parametric heating measurement for Rb atoms in a 1D array of four 817 nm tweezers. The separation between the traps is 4 μm. Before the measurement, the powers of the traps were balanced using a CCD. The range of trap frequencies measured across the array is within 1 % of the mean. We conclude that the CCD normalisation successfully balances the trap intensities.

We have performed characterisation measurements of the beam waists for the 817 nm, 938 nm, and 1064 nm tweezers along the three orthogonal trap axes. When the beam power outside of the cell and the transmission of the optical system are known, we can calculate the beam waist from a trap frequency measurement. Table 3.1 summarises results of characterisation measurements for all of the tweezers. The radial anisotropy $w_x > w_y$ is due to clipping of the tweezer beams by mirrors and their mounts before the beam reaches the high-NA lens. The aim of changing the mounting of the dichroics in the tweezer beam paths was to reduce clipping, which would in turn reduce the beam waist in the affected direction, w_x. The process did not improve the beam waists of the 938 nm tweezer. Likely this is a result of curvature on the dichroic mirror that the 938 nm tweezer beam reflects off, caused by unequal tension from the glue that fixes it to its mount. In contrast, the results show that the change was effective for the 817 nm tweezer. The improvement in beam waist for the 1064 nm tweezer is due to the application of appropriate Zernike polynomials.

Before Re-alignment				
Tweezer Wavelength (nm)	Transmission	w_{x} (μm)	w_{y} (μm)	z_{R} (μm)
814	0.66(2)	1.02(2)	0.82(2)	3.27(14)
938	0.73(2)	1.247(15)	1.036(18)	4.5(2)
1064	0.69(3)	1.530(13)	1.350(6)	6.91(18)
After Re-alignment				
Tweezer Wavelength (nm)	Transmission	w_{x} (μm)	w_{y} (μm)	z_{R} (μm)
817	0.78(2)	0.910(6)	0.815(5)	3.39(3)
938	0.78(2)	1.29(2)	1.16(2)	5.2(2)
1064 (with Zernike corrections)	0.86(2)	1.17(2)	1.05(2)	4.18(14)

Table 3.1: Tweezer transmission and beam waists before and after implementing the new dichroic mounting. The beam waists $w_{\mathrm{x,y}}$ and Rayleigh ranges z_{R} are determined in parametric heating experiments. The radial asymmetry, $w_x > w_y$, is due to clipping of the tweezer beams before they reach the high-NA lens. The re-alignment process was detrimental for the waists of the 938 nm tweezer, however the waists of the 817 nm tweezer were improved.

3.2 Temperature Measurements

The initial motional state of the atom is sampled from a thermal distribution, so we can characterise the external state using a temperature measurement. The release-and-recapture method is a well-established way of measuring the temperature of an atom in an optical tweezer trap [219, 220]. Figure 3.5(a) illustrates the required steps: the trap is turned off to release the atom and then turned back on after a variable period of time to recapture the atom. The likelihood of recapturing the atom depends on its kinetic energy and how far it travels while the trap is off. The situation can be simulated using classical equations of motion and sampling the initial position and velocity from a thermal Maxwell-Boltzmann distribution. In Figure 3.5(b) we present the results of a release and recapture measurement of a Cs atom in a 938 nm

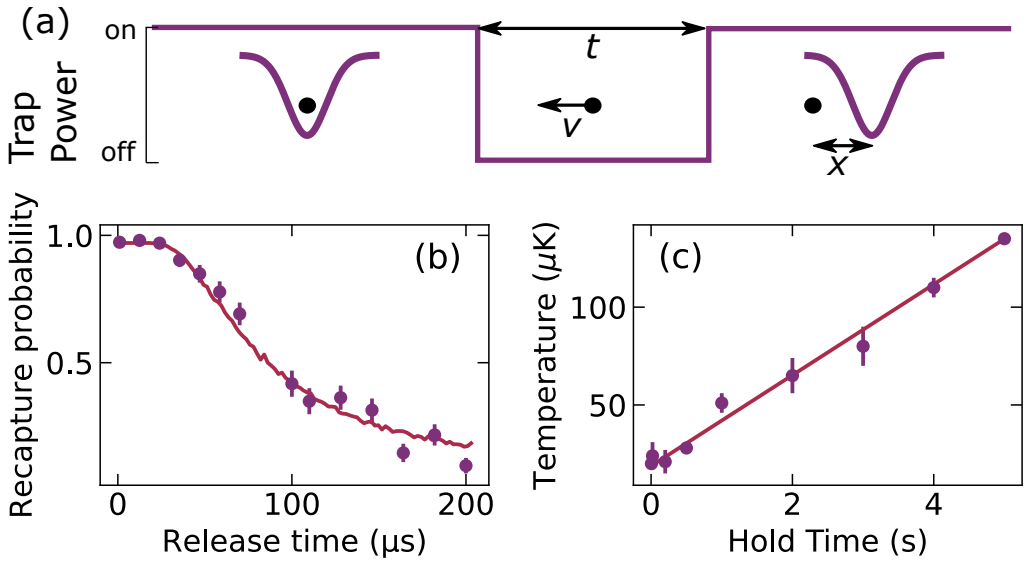

Figure 3.5: Temperature measurements of a Cs atom in a 938 nm tweezer. (a) The release and recapture method: the trap is turned off for a duration t during which the atom moves with a velocity v sampled from a thermal distribution. When the trap is turned back on, the displacement x from the trap centre determines whether the atom is recaptured. (b) Fitting a Monte Carlo simulation to a release and recapture measurement we extract a temperature of 5.3(4) μK for a trap depth of 0.88 mK. (c) Holding a Cs atom in a 2.3 mK 938 nm tweezer causes heating at a rate of 23.2(3) $\mu\mathrm{K\,s^{-1}}$.

tweezer with a depth of 0.88 mK, after polarisation gradient cooling has been applied. By comparing the recapture probability as a function of release time to a Monte Carlo simulation we extract a temperature of 5.3(4) μK. Since the cylindrically-symmetric tweezer is more tightly confining in the radial direction, we relate the measured temperature to a mean motional level of $\langle n \rangle = 1.33(13)$ averaged over the radial directions.

Three things are worth noting about the temperature measurements. Firstly, we typically measure $\langle n \rangle \sim 2$. Secondly, an adiabatic ramp of the trap power preserves the motional level and therefore changes the temperature. Finally, any recaptured atoms will likely gain energy from the process. Moving a tweezer or ramping its power after the release and recapture can easily cause additional loss of the motionally excited atoms, which can be misinterpreted as a hotter temperature. To avoid the additional loss, the atom should either be cooled straight after the release and recapture or re-imaged before there is an opportunity for additional loss. The data in Figure 3.5(b) were taken with immediate re-imaging, whereas the data in Figure 3.5(c) implemented cooling after release and recapture.

Figure 3.5(c) presents release-and-recapture measurements of the heating due to holding a Cs atom in a 2.3 mK 938 nm tweezer. In these measurements the trap depth is ramped up after loading and imaging. Both the release and recapture and the re-imaging to detect survival were performed in a 2.3 mK trap to avoid additional loss complicating the interpretation of results. We fit a linear heating rate of 23.2(3) $\mu\mathrm{K\,s^{-1}}$, which is significantly larger than the predicted 12 $\mu\mathrm{K\,s^{-1}}$ due to recoil from scattering tweezer photons. The fitted offset of 18.8(1.3) μK implies a mean motional level of $\langle n \rangle = 3.4(5)$, which is also larger than expected after polarisation gradient cooling. The increased temperature after cooling and the excessive heating rate likely originate from the intensity noise which appears when the tweezer power is above a certain threshold (see Section 2.1.4), with the measured threshold being within 10 % of the power that creates a 2.3 mK trap. However, we note that the linear increase in temperature, rather than exponential, is indicative of pointing noise rather than intensity noise [218]. This could occur through a coupling between the intensity and the trap centre position, such as in the presence of strong vector light shifts [150, 155, 221].

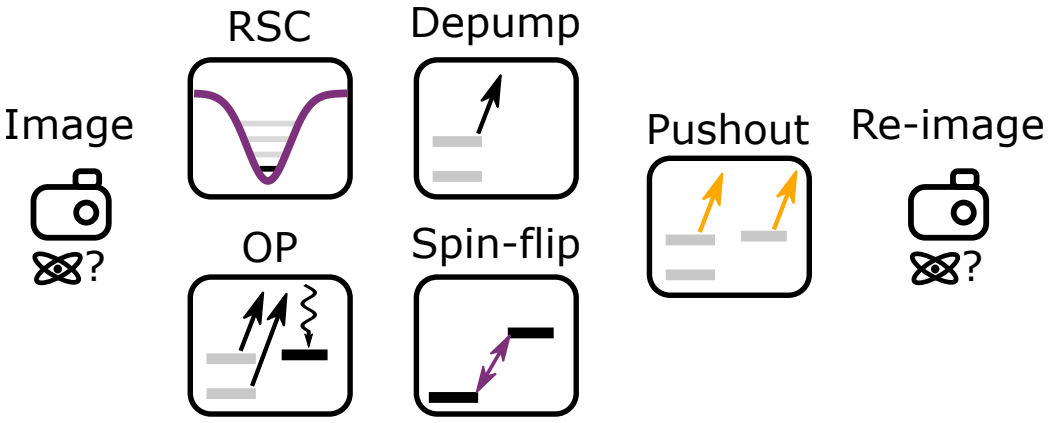

Figure 3.6: Stages of an experiment involving transfer between hyperfine spin states. An initial image determines whether an atom was loaded. Raman sideband cooling and optical pumping prepare the motional state and the spin state. A depump pulse or coherent microwave or Raman pulse transfers the atom between spin states. Finally, a state-selective pushout pulse maps the spin state onto the trap occupancy in a final image.

3.3 Internal State Control

Figure 3.6 outlines the general structure of an experiment: image, prepare the quantum state, manipulate the quantum state, then project the quantum state and re-image. The initial image determines whether the run of the experiment started with an atom. Runs that start without an atom are excluded from post-processing. Then we prepare a particular spin state, and some experiments also require preparation of a particular motional state. Our optical pumping (OP) scheme (see Section 2.1.4) prepares a specific hyperfine spin state; $|\uparrow\rangle = |f = 2, m_f = 2\rangle$ for Rb, or $|\uparrow\rangle = |4, 4\rangle$ for Cs. Implementing Raman sideband cooling (RSC) allows preparation of the motional ground state of the trap, as will be discussed in Chapters 4 and 5. If we pulse on the $\mathrm{OP}^{\uparrow}$ beam, the impurity of the polarisation or misalignment of the quantisation axis mean that the atom is no longer in a dark state and will scatter photons. The depump step is therefore used to characterise the fidelity of the OP. In other cases, coherent transfer between hyperfine spin states is required. MW radiation or the Raman beams can be used to make a spin-flip transition to the $|\downarrow\rangle = |1, 1\rangle$ state for Rb, or the $|\downarrow\rangle = |3, 3\rangle$ state for Cs. Finally, we detect the spin state by ramping down the trap depth and

ejecting atoms from the upper hyperfine manifold using a resonant pushout pulse. Only atoms in the lower hyperfine manifold survive to be re-imaged at the end of the sequence. The icons in Figure 3.6 will be used in the rest of this chapter to illustrate the stages involved in particular experiments, which are performed simultaneously for a Rb atom and a Cs atom in separate tweezers.

3.3.1 Initial State Preparation

The fidelity of the state preparation depends on the OP beams selectively driving σ^+ transitions. The selectivity depends on two criteria: that the incident light is circularly polarised with the correct handedness and that the propagation direction of the beam is parallel to the quantisation axis. We maximise the state preparation fidelity by addressing each of the criteria in turn.

Figure 3.7 outlines an experiment which tests the fidelity of the state preparation. The experiment is composed of four stages. Firstly, both OP beams are applied for 5 ms, which is a sufficient duration to saturate the probability of occupying the dark state even with suboptimal OP beam polarisation. Secondly, 0.7 μW of $\mathrm{OP}^{\uparrow}$ light is pulsed on for sufficient duration to observe depumping from the nominally dark state, $|\uparrow\rangle$. When the polarisation is impure or the quantisation axis misaligned, then the spin-stretched state is no longer dark to the incident light and the depumping rate increases. The resultant spin state after depumping has a roughly equal probability of being in the upper or lower hyperfine manifolds. Thirdly, a pushout pulse ejects atoms from the upper hyperfine manifold and finally any surviving atoms are re-imaged. When the OP successfully prepares the $|\uparrow\rangle$ state, the pushout pulse should eject every atom. In this case, optimising the OP corresponds to minimising the survival probability.

The polarisation of the OP beams is set to maximise the probability of driving a σ^+ transition. Figure 3.7(a) presents results from the depumping experiment when the quarter waveplate which both OP beams pass through was set to different angles. In this case the depump duration was 10 ms. Only small adjustments to the quarter waveplate angle are made so that the initial state preparation still has a sufficiently high fidelity. The depumping rate is

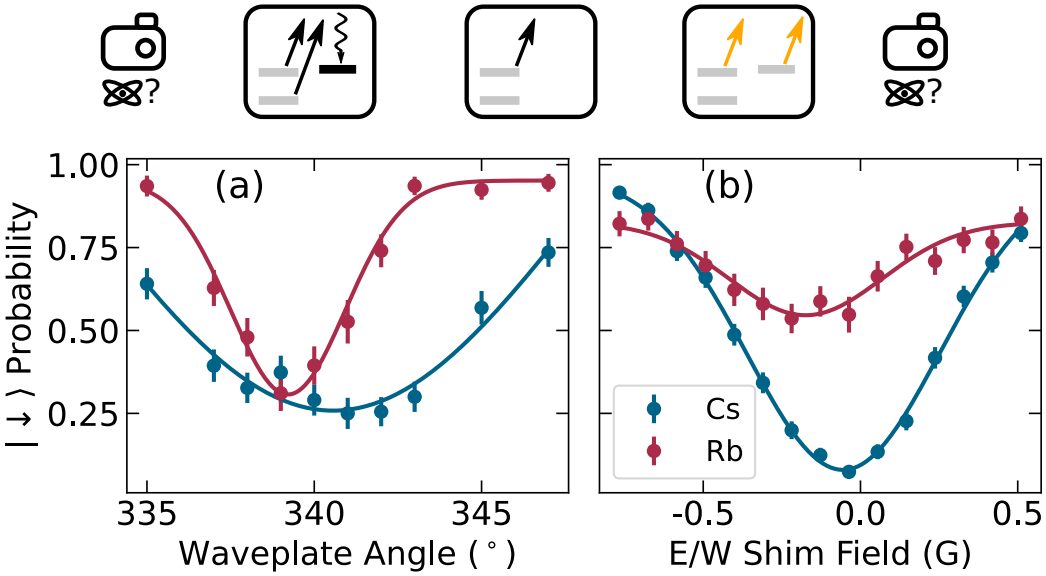

Figure 3.7: Optimising the fidelity of OP using a 4-stage experiment: 1) prepare the atom in the dark state, 2) depumping $OP^{\uparrow}$ light reduces the dark state occupation, 3) a pushout pulse ejects an atom from the upper hyperfine manifold, 4) image to measure the survival probability. (a) The angle of the quarter waveplate sets the polarisation of the OP light. The depumping rate is minimised when the OP light preferentially drives σ^+ transitions. (b) The E/W shim field modifies the direction of the quantisation axis. The depumping rate is minimised when the quantisation axis is aligned with the OP beam propagation direction. The different depumping rates of Rb and Cs lead to different widths and depths of the fitted features.

minimised for a quarter waveplate angle of 341(1) ° for Cs, or 339.2(1) ° for Rb. Notably, Rb was more sensitive to the waveplate angle, which is related to having a faster depumping rate. The optimal angle is within 1 ° of where the OP beam has maximally circular polarisation, as measured before the light reaches the cell. We conclude that there is a small modification to the polarisation due to the birefringence of the cell wall. We support this theory using measurements of the polarisation of the OP beam before and after it has passed through the cell. The same fraction of circular polarisation is achievable after passing through the cell. However, there is a phase shift of 4.6(5) °; the OP beam has maximally circular polarisation at a slightly different angle of the waveplate. We set the quarter wavplate angle to 339.2 ° so that the depumping rate is minimised.

We set the currents in the shim coils to apply a bias magnetic field in the N/S direction parallel to the propagation direction of the OP beams. Figure 3.7(b) displays results from the depumping experiment when the orthogonal E/W shim field was set at a range of different fields. For these measurements the depumping duration was 2 ms. The N/S shims are set to apply a field of 3 G, reduced from the usual 4.8 G so that the direction of the total field is more sensitive to the field applied in the E/W direction. The depumping rate is minimised for Cs when the E/W shims apply a field of 0.055(4) G in the west direction, but for Rb the optimal field was 0.17(2) G in the west direction. In practice, we compromise between the optimal fields for Rb and Cs.

3.3.2 Trap-Induced Spin Relaxation

Spontaneous Raman scattering of tweezer photons causes undesired spin relaxation. Having prepared the atoms in the dark state, any manipulation must be carried out before spin relaxation occurs. The Raman scattering rate is proportional to the intensity of the tweezer and scales with the detuning from the D_1 and D_2 lines as $1/\Delta^4$ [222]. The Raman scattering rate is therefore much less in the 1064 nm tweezer compared to the 817 nm or the 938 nm tweezer, and there is incentive to use lower intensities. However, as we shall see in Section 5.3 and Section 4.5, there are situations in which the tweezer power and wavelength are constrained by other conditions. At a typ-

ical intensity $100\,\mathrm{kW\,cm^{-2}}$ used for holding and moving atoms in tweezers, the Raman scattering rate for a Cs atom in the 938 nm tweezer is $4\,\mathrm{s^{-1}}$ [164], and the rate for a Rb atom in the 817 nm tweezer is $6\,\mathrm{s^{-1}}$.

A simple but important distinction must be made between the spontaneous Raman scattering rate and the spin relaxation rate. Not every scattering event changes f, but the measured spin relaxation rate depends upon f changing. Just as the total scattering rate is the sum of the Rayleigh scattering rate (when the state does not change) and the Raman scattering rate (when the state does change), so the Raman scattering rate can be split into f-changing or f-maintaining rates.

Intensity noise on the tweezer light can cause a transition between spin states. The intensity noise can induce transitions between m_f states when its frequency is near to the Zeeman splitting of hyperfine sublevels and the polarisation of the tweezer is impure [223]. Noise at these frequencies is most likely to occur from non-linear mixing of tones in the multitone signal used to create an array. Therefore, we test the spin relaxation rate when the tweezer AOD is driven with a multitone signal. For this experiment the depump step plays an additional role: if the atom's m_f state changes, then it is no longer dark to the $\mathrm{OP}^{\uparrow}$ light. Scattering $\mathrm{OP}^{\uparrow}$ photons is then likely to change the f state of atoms that were in a different m_f state of the upper hyperfine manifold, such that the pushout should only eject atoms that are in the dark state. We measure spin relaxation with a 1/e time of 0.18(6) s for a Cs atom in a 1 mK 938 nm trap when the AOD is driven with two tones differing by 2 MHz. Similarly, we measure spin relaxation with a 1/e time of 0.11(3) s for a Rb atom in a 1 mK 817 nm trap when the two-axis AOD is driven with four tones all differing by 2 MHz. These results are consistent with the expected spontaneous f-changing Raman scattering rates from tweezer photon scattering, which implies that we can create arrays of tweezer traps without the additional m_f state scrambling caused by intensity noise and impure polarisation.

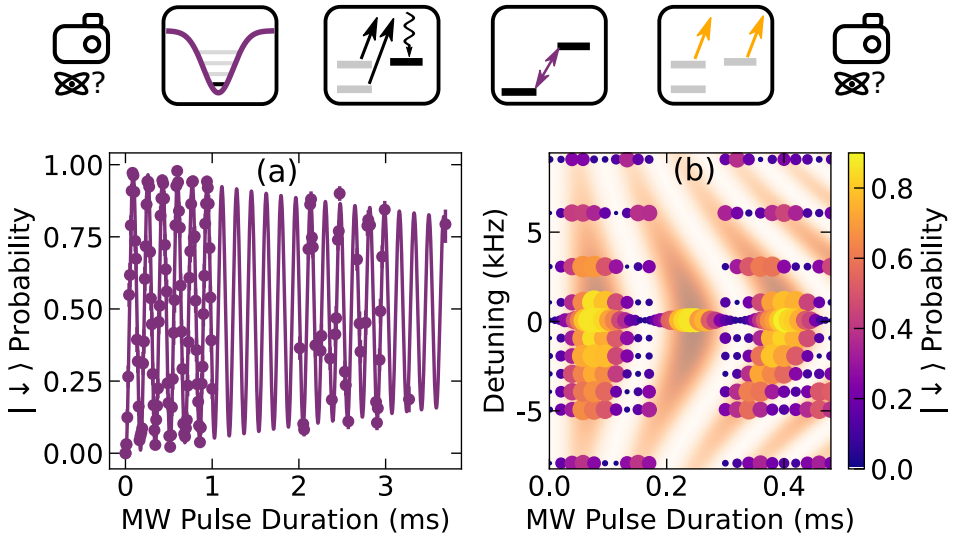

Figure 3.8: Coherent transfer between Rb hyperfine spin states is achieved using a MW pulse. (a) Rabi oscillations between hyperfine spin states with a Rabi frequency of 5.863(3) kHz and a coherence time of 9.4(9) ms. (b) When the MW frequency is detuned from resonance, the generalised Rabi frequency increases and the maximum probability of occupying the $|\downarrow\rangle$ state is reduced. The faded orange background displays a best fit to the data.

3.3.3 Coherent Transfer Between Spin States

Coherent transfer between spin states is an important step in many atomic and molecular physics experiments, which is achieved using either resonant MW radiation, or a two-photon optical Raman transition. There are pros and cons to each method. The Rabi frequency of the MW transitions is constrained to < 10 kHz by technical limitations. Furthermore, our lab only had access to one MW signal generator. Alternatively, the two-photon Raman transitions can give a stronger coupling, but also suffer from additional sources of decoherence due to fluctuations in the powers of the Raman beams and thermal dephasing as a result of spin-motion coupling. Although the spin-motion coupling could be removed by using co-propagating Raman beams, exerting control over the motional state is essential for RSC. Overall, we choose to use MW transitions to drive spin flip transitions for Rb, and we use two-photon Raman transitions to drive spin flip transitions for Cs.

MW transitions with long coherence times are achieved by removing sources

of decoherence. Figure 3.8(a) displays Rabi oscillations between the $|\uparrow\rangle$ and $|\downarrow\rangle$ spin states of a Rb atom. The best-fit curve has a Rabi frequency of $\Omega_{\mathrm{MW}} = 5.863(3)\,\mathrm{kHz}$ and a coherence time of $9.4(9)\,\mathrm{ms}$, an order of magnitude greater than the π pulse duration. In order to achieve such long coherence times, we reduce thermal dephasing from the differential light shift of the tweezer by removing kinetic energy from the atom [170]. We use RSC to prepare an atom in the motional ground state of the trap. The RSC ends with the atom in the dark state, $|\uparrow\rangle$. The trap depth is ramped down to $0.2\,\mathrm{mK}$ so that the differential light shift from the tweezer is $< 3\,kHz$. Then, A MW pulse of variable duration at a frequency near the Zeeman-shifted ground state hyperfine splitting induces Rabi flopping between the hyperfine spin states. Finally, the pushout pulse projects the spin state onto the trap occupancy measured in a final image. The long coherence time of the Rabi oscillations gives us confidence that high-fidelity transfer between the spin states is possible.

The MW frequency must be on resonance in order to maximise the transfer between spin states. The probability of detecting an atom in the $|\uparrow\rangle$ state is given by:

$$P_{\uparrow}(t,\delta) = \left(\frac{\Omega_{\mathrm{MW}}}{\Omega}\sin(\frac{\Omega t}{2})\right)^2, \tag{3.1}$$

where $\Omega = \sqrt{\Omega_{\mathrm{MW}}^2 + \delta^2}$ is the generalised Rabi frequency when the MWs are driven at a Rabi frequency Ω_{MW} and δ is the detuning from resonance. Figure 3.8(b) shows how detuning from resonance speeds up the frequency of oscillations and limits the maximum transfer. In this experiment the maximum transfer was also limited by imperfect initial state preparation. The measured transition frequency for the Rb atom in the $4.78\,\mathrm{G}$ applied magnetic field is $6844.7193(3)\,\mathrm{MHz}$.

These measurements indicate that high-fidelity transfer between hyperfine spin states is possible using a π pulse. However, a more precise test of the fidelity requires applying multiple pulses.

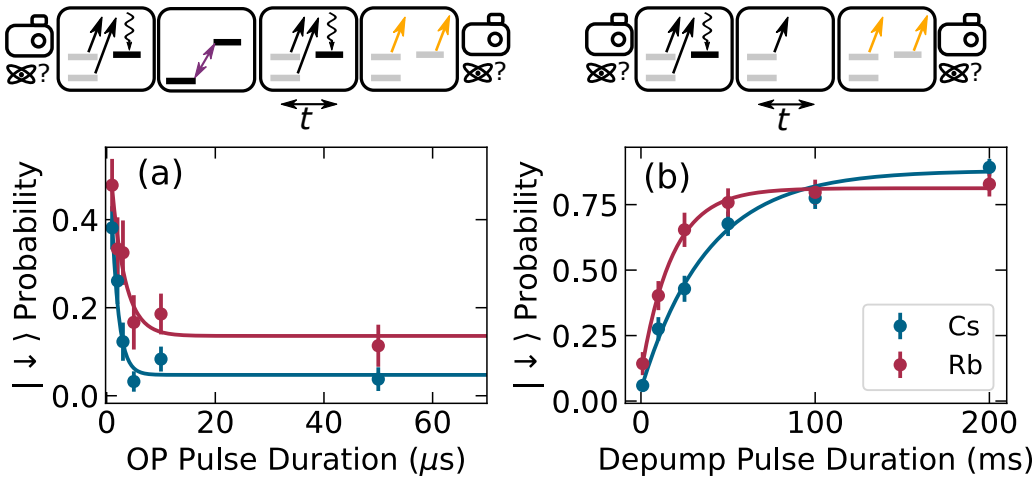

Figure 3.9: The fidelity of the OP is quantified by comparing the OP timescale to the depumping timescale. (a) The atom is prepared in the $|\uparrow\rangle$ state then transferred to the $|\downarrow\rangle$ state. An OP pulse of variable duration starts transferring the atom back to the dark state with a 1/e time of 1.3(4) μs for Cs and 3(1) μs for Rb. (b) After preparing the atom in the dark state, a depumping pulse from the $\mathrm{OP}^{\uparrow}$ beam reduces the dark state population due to the finite probability of driving σ^- or π transitions. The 1/e time is 38(5) ms for Cs and 18(1) ms for Rb.

3.3.4 Fidelity of State Preparation and Transfer

At certain stages of the experiment we require the spin to be reset to the dark state by dissipative OP. In particular, this is an essential step for RSC. It is important to reduce heating by minimising the number of photon scattering events. This is achieved by selectively driving σ^+ transitions, as previously discussed. We can characterise the performance of the OP by comparing the rate of scattering into and out of the dark state.

Figure 3.9(a) displays a measurement of the time taken to pump into the dark state from a spin-stretched state in the lower hyperfine manifold. After preparing the atom in $|\uparrow\rangle$, a π pulse transfers to $|\downarrow\rangle$. Then both OP beams are applied for a variable duration. The measured timescale for pumping into the dark state is mostly dependent on the scattering rate of the $\mathrm{OP}^{\downarrow}$ beam, and the $\mathrm{OP}^{\uparrow}$ beam acts as a repump. Since it is the scattering rate of the $\mathrm{OP}^{\uparrow}$ beam which dominates the depumping rate, it is beneficial to reduce the scattering rate of this beam. With this in mind, we set the intensity of the $\mathrm{OP}^{\uparrow}$ beam to $0.06\,\mathrm{mW\,cm^{-2}}$ and the intensity $\mathrm{OP}^{\downarrow}$ beam to $0.5\,\mathrm{mW\,cm^{-2}}$. For these intensities, with the detuning set on resonance, the 1/e time for the results in Figure 3.9(a) is $1.3(4)\,\mu$s for Cs and $3(1)\,\mu$s for Rb. The finite offset observed for Rb in Figure 3.9(a) is unexpected, but is caused either by depumping between the OP pulse and the pushout, or more likely by the pushout beam being off-resonant, resulting in incomplete pushout for this particular experiment.

Figure 3.9(b) displays a measurement of the depumping rate out of the dark state. The experiment uses the optimised quarter waveplate angle and shim fields, with the same OP beam intensities: $0.06\,\mathrm{mW\,cm^{-2}}$ for the $\mathrm{OP}^{\uparrow}$ beam and $0.5\,\mathrm{mW\,cm^{-2}}$ for the $\mathrm{OP}^{\downarrow}$ beam. Depumping from the dark state occurs with a 1/e time of 38(5) ms for Cs and 18(1) ms for Rb. The tweezer causes observable spin relaxation on these timescales, such the the measured depumping rate is $1/\tau = 1/\tau_{\mathrm{OP}^{\uparrow}} + 1/\tau_{\mathrm{tweezer}}$. Correcting for the contribution from the tweezer with trap depth 2 mK for Cs, or 1.5 mK for Rb, we calculate a depumping 1/e time due to the $\mathrm{OP}^{\uparrow}$ beam of 70(20) ms for Cs, and 24(3) ms for Rb. Comparing the depumping rate to the OP rate, we can estimate the probability of preparing the dark state as $> 1 - 1.5 \times 10^{-4}$

assuming that both rates remain constant. In reality, the OP rate will slow down once there is a significant probability of occupying the upper hyperfine manifold. To get another perspective, we can compare the purity of the $OP^{\uparrow}$ beam's polarisation.

We estimate the polarisation purity by comparing the scattering rate of the $OP^{\uparrow}$ beam to the depumping rate. The scattering rate is measured with a similar method as the depumping experiment, except that the quantisation axis is set at 45° to the OP beam propagation direction during the depump pulse. This allows the incident light to couple to all of the spin states. We ramp down the trap power during the depump step for both the scattering rate and the depump measurement, such that we remove the spin relaxation caused by the tweezer. The detuning of the OP beams is adjusted to compensate for the change in light shift. Comparing the scattering rate and depumping rate for a Cs atom, we estimate the probability of driving a σ^+ transition relative to the probability of driving a σ^- or a π transition, giving a polarisation purity of $(3.7(8)) \times 10^3 : 1$.

We characterise the fidelity of transferring between spin states by applying a series of spin flips. Figure 3.10(a) displays the results of applying an odd number of π pulses to an atom that starts in the $|\uparrow\rangle$ state. For these measurements it is important to minimise the effects of thermal dephasing by preparing the atom in the motional ground state. The error from each pulse compacts, such that after a series of N pulses, the probability of occupying $|\downarrow\rangle$ is given by [224]:

$$P_{\downarrow} = \frac{1}{2} + \frac{1}{2}(1 - d_{if})(1 - d)^N. \tag{3.2}$$

Here, d_{if} is the depolarisation probability of the initial state preparation and final state detection, including loss during imaging. d is the average error per pulse. The detuning and duration for the pulses are optimised in a preliminary experiment. The results from fitting Equation 3.2 to the data in Figure 3.10(a) are summarised in Table 3.2. For Cs, we use 2-photon Raman transitions with a pulse duration of 16 μs, which is short enough that the spin relaxation due to scattering tweezer photons contributes a depolarisation of only 2 % for a sequence of 100 pulses. The dominant contribution to the pulse error, $d = 0.048^{+0.006}_{-0.006}$, is from off-resonant spontaneous Raman scattering

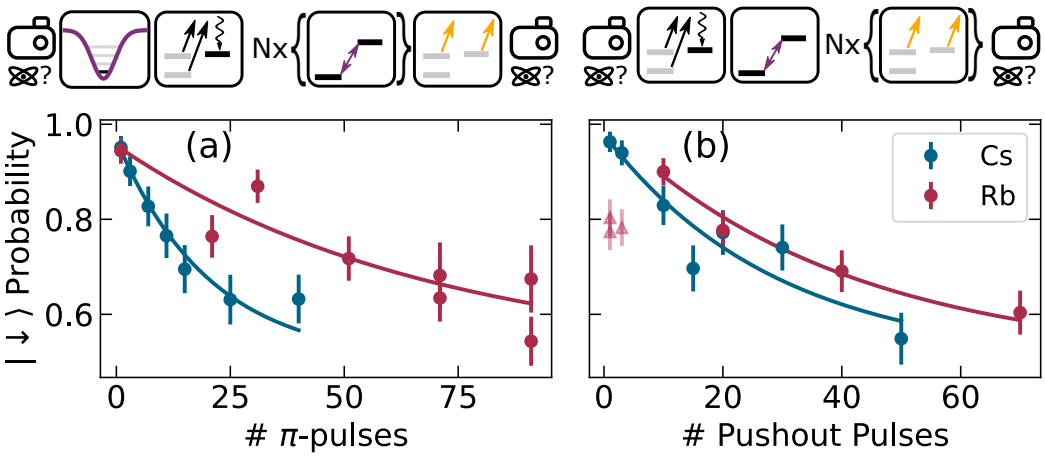

Figure 3.10: Measuring the fidelity of transferring between spin states and of detecting the spin state. (a) After preparing the atom in the dark state, we apply an odd number of spin-flip pulses before a pushout pulse and image detects the state. The spin flip is performed with a MW pulse for Rb and a 2-photon Raman carrier transition for Cs. (b) The atom is prepared in the $|\downarrow\rangle$ state by OP and a spin flip. Then, we apply a series of pushout pulses to measure the fidelity. Anomalous points in the data for Rb are plotted as faded triangles.

Measurement	Cs	Rb
Depolarisation (state preparation, imaging, and pushout)	$0.07^{+0.03}_{-0.04}$	$0.09^{+0.08}_{-0.08}$
Error per π pulse	$0.048^{+0.006}_{-0.006}$	$0.014^{+0.004}_{-0.002}$
Depolarisation (state preparation and imaging)	$0.04^{+0.05}_{-0.04}$	$0.00^{+0.08}_{-0.00}$
Error per pushout	$0.034^{+0.008}_{-0.006}$	$0.024^{+0.002}_{-0.004}$
State preparation error	0.002	0.002

Table 3.2: Results from measurements of state preparation, detection and gate fidelity.

from the Raman beams. For Rb, we use MW transitions, for which the dominant contribution to the pulse error, $d = 0.014^{+0.004}_{-0.002}$, is from dephasing caused by differential light shifts [150, 225] and magnetic field noise. The detrimental effects of differential light shifts could be further suppressed by satisfying a "magic" trapping condition [226, 227]. However, removing the dephasing due to magnetic field noise would require choosing a Zeeman-insensitive transition.

We characterise the fidelity of the state detection by applying a series of pushout pulses. This helps discern the dominant contribution to the state preparation and measurement error. Figure 3.10(b) displays the results from preparing an atom in $|\uparrow\rangle$, applying a spin-flip to transfer to $|\downarrow\rangle$, and then applying a series of pushout pulses. The trap depth is ramped up in 1 ms and down in 1 ms between pushout pulses so that scattering from the trap during this period of the sequence is accounted for. The results from Equation 3.2 to the data in Figure 3.10(a) are summarised in Table 3.2. By extracting the error due to the pushout, we find that the depolarisation due to the state preparation and imaging is negligible for Rb, but as high as $0.04^{+0.05}_{-0.04}$ for Cs. These depolarisation values are consistent with separate measurements of repeated imaging pulses, suggesting that the error in the initial state preparation is small.

These state preparation fidelities are an important part of the sequence for creating a molecule by magnetoassociation. Efficient magnetoassociation is

possible when Rb and Cs are prepared in the $|1,1\rangle$ and $|3,3\rangle$ spin states respectively, as has been demonstrated in experiments with bulk mixtures [162, 163]. The measurements above show that we can prepare this joint spin state with a probability of $0.935^{+0.007}_{-0.007}$. However, we have not yet accounted for spin relaxation during the time taken to merge the traps together. Furthermore, efficient magnetoassociation also requires preparation of the motional ground state, which is the subject of the next chapter.

Chapter 4

Designing the Protocol for Raman Sideband Cooling

Preparing an atom in a particular motional state is an important stage in a range of atomic and molecular physics experiments. Experiments have demonstrated quantum interference between motional states [86] or used motional states as a synthetic dimension [228]. Reduction in thermal dephasing improves the fidelity of the transfer between quantum states [149, 154, 225], an essential component for implementing quantum gates. Most importantly for our purposes, magnetoassociation of two atoms into a molecular state requires initiation in the relative motional ground state [99, 146]. The associated molecule inherits the motional state of the atom pair [99, 155].

It is therefore our aim to cool an atom to the motional ground state of its trapping potential. Ground-state cooling of single particles was first demonstrated for heavy atomic ions using resolved-sideband cooling [147, 148, 229], and then for lighter ions using Raman sideband cooling (RSC) [230, 231] or electromagnetically-induced transparency cooling [232]. Subsequently, similar methods were applied to neutral atoms in optical lattices using RSC [172, 233, 234]. In the following text we explain how RSC can be used to prepare a single neutral atom in the motional ground state of an optical tweezer [149–154].

A significant portion of the material in this chapter is taken from the author's work in Ref. [166].

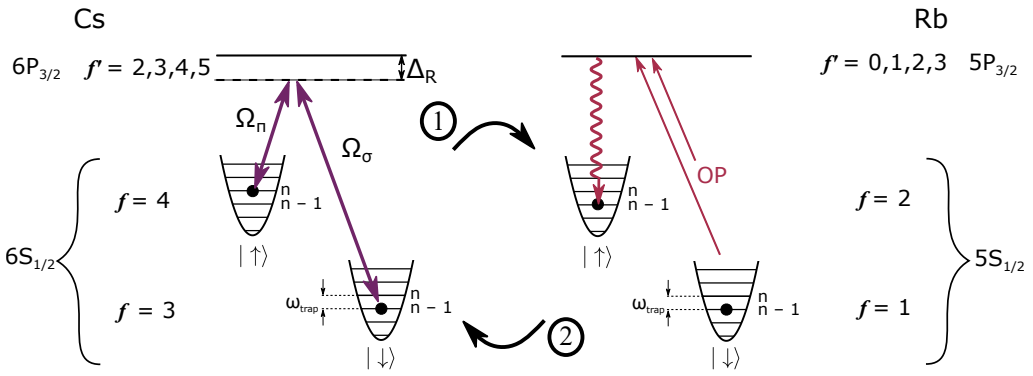

Figure 4.1: The two stages of a Raman sideband cooling iteration. First a coherent two-photon Raman transition transfers some of the population from $|\uparrow; n\rangle \rightarrow |\downarrow; n-1\rangle$. One beam is circularly polarised for σ^+ transitions with Rabi frequency Ω_σ. The other is linearly polarised for π transitions with Rabi frequency Ω_π. The single-photon detuning from the excited state is Δ_R. Then a dissipative optical pumping step resets the spin, preserving the motional level: $|\downarrow; n-1\rangle \rightarrow |\uparrow; n-1\rangle$. Each iteration of these stages removes one quantum of motional energy, $\hbar\omega_\mathrm{trap}$, where ω_trap is the trap frequency. The hyperfine spin state manifolds are labelled by the total angular momentum quantum number, f.

4.1 The Method of Raman Sideband Cooling

RSC relies on two processes to transfer the atom between the motional Fock states $|n\rangle$ of the optical tweezer trap. In the first step, a stimulated two-photon Raman transition transfers the atom between hyperfine spin states, $|\uparrow\rangle$ and $|\downarrow\rangle$. When the transition is on resonance with a lowering sideband, it performs a spin flip and reduces the motional level: $|\uparrow; n\rangle \rightarrow |\downarrow; n-1\rangle$. Then, in the second step, OP transfers the population back into the original hyperfine state while preserving the motional level: $|\downarrow; n-1\rangle \rightarrow |\uparrow; n-1\rangle$. Separating the two steps by alternating pulses between Raman and OP beams allows faster cooling than applying both sets of beams simultaneously [235]. The combination of the two processes reduces the motional level by one quantum, as illustrated in Fig. 4.1. Iterating over the procedure cools the atom into the lowest motional level, at which point there is no further level to descend to, and so the atom decouples from both the Raman and the OP light.

The effectiveness of an RSC protocol is determined by the competition between cooling rates and heating rates. The main limitation on the cooling rate is the reduced sideband transfer due to dephasing from differential light shifts, beam power fluctuations, and magnetic field noise. The important sources of heating are intensity and pointing noise from the tweezer trap, recoil from OP photons, and off-resonant Raman transitions which increase the motional level. These obstacles to effective ground-state cooling are addressed in Section 4.4.

4.2 Internal and External States

The tight confinement of optical tweezers puts the atom in the Lamb-Dicke (LD) regime, allowing control over the external motional level through atom-light interactions [236]. Atoms are illuminated by laser light, leading to photon scattering events which result in atomic recoil due to the conservation of momentum. The LD parameter $\eta = \sqrt{\omega_{\text{recoil}}/\omega_{\text{trap}}} = \sqrt{\hbar k^2/(2m\omega_{\text{trap}})}$ is determined by the trap frequency, ω_{trap}, and the photon recoil energy, $\hbar\omega_{\text{recoil}} = \hbar^2 k^2/2m$ for resultant wavevector k and mass m. The LD parameter satisfies $\eta^2(n+1) \ll 1$ in the LD regime, resulting in a suppression of motional excitation during photon scattering events [7]. Being in the LD regime is important for both of the aforementioned steps of RSC. In the OP step, the excitations and subsequent spontaneous emissions are on the carrier transition, i.e. they preserve the motional level. But it is also possible to make transitions between specific motional states - sideband transitions - provided the transition linewidth is smaller than the spacing of the energy levels. A stimulated two-photon Raman transition satisfies this condition by coupling two long-lived states via an excited state that is not populated [237, 238]. Sideband transitions that change the motional level occur at intervals of the trap frequency. In standard notation, a blue sideband (BSB) transition increases the motional level, whereas a red sideband (RSB) transition reduces the motional level. The direction of the atomic recoil momentum determines which trap axes the Raman transition can couple to. To cool to the 3D ground state, the laser beams driving Raman transitions must be arranged to allow coupling to the different trap axes.

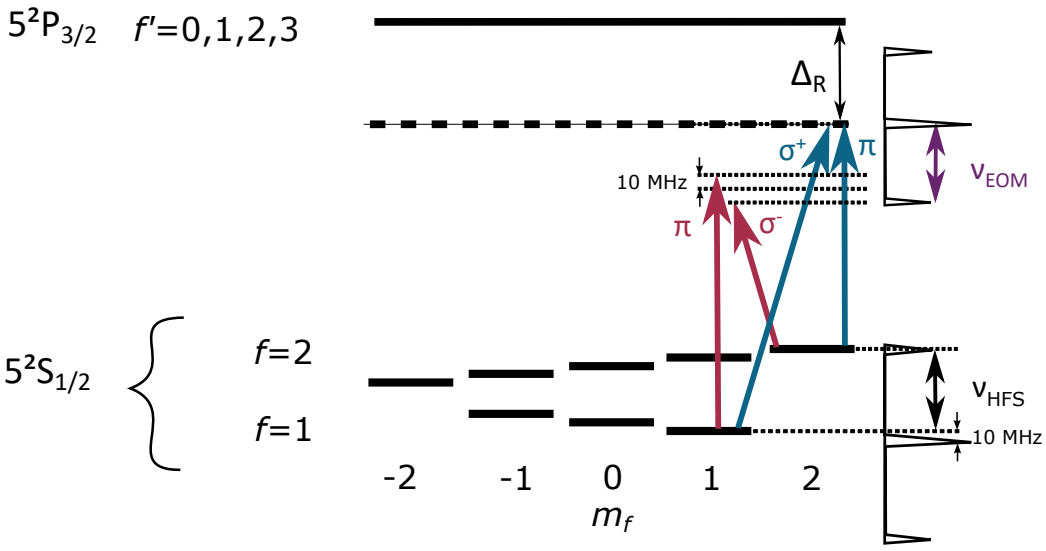

Figure 4.2: Simplified diagram of the hyperfine structure of a Rb atom showing the desired two-photon Raman transition and an undesired Raman transition. The hyperfine structure for Cs has different values for the total angular momentum quantum number f. Blue: a two-photon Raman transition between two spin-stretched states is possible when one Raman beam drives a σ^+ transition and the other drives a π transition. The energy difference is added to one of the Raman beams using the upper sideband of an EOM. Red: if the circularly polarised Raman beam has residual light of the opposite handedness, it can drive a two-photon Raman transition with the lower EOM sideband that destructively interferes with the desired transition. We suppress this possibility by offsetting the EOM frequency by 10 MHz and using the AOM frequencies to bring the desired transition back onto two-photon resonance.

Fig. 4.2 displays a desired and an undesired two-photon Raman transition coupling the spin-stretched hyperfine states used in this work. RB1 predominately drives σ^+ transitions and RB2 drives π transitions. Other two-photon transitions are forbidden by dipole selection rules. The desired transition, in blue, occurs via a single virtual excited state. The other transition, in red, requires RB1 to drive σ^- transitions with the lower EOM sideband frequency. The red transition is possible through two virtual excited states ($|f' = 1, m_{f'} = 1\rangle$ and $|f' = 2, m_{f'} = 1\rangle$). There is quantum interference when the Raman transition is possible through several pathways, which in this case makes the Raman coupling quite sensitive to the polarisation of RB1. Therefore, we suppress the undesired transition by setting the polarisation of RB1 using an 1000 : 1 polariser and a quarter waveplate with a retardance of 0.267 waves at 780 nm, and 0.243 waves at 852 nm. Assuming linearly polarised incident light and that the waveplate angle is set to within 1 degree, this maintains a polarisation purity of 500 : 1 (calculated using Jones matrices [239]). Secondly, we offset the EOM frequency by 10 MHz, $\nu_{\mathrm{EOM}} = \nu_{\mathrm{HFS}} + 10\,\mathrm{MHz}$, such that when the frequencies of AOM1 and AOM2 are set to bring the desired transition into two-photon resonance, the undesired transition is detuned by -20 MHz.

4.3 Master Equation Formulation

The evolution of the atomic state can be described by the Schrödinger equation [240] or the Lindblad master equation [241, 242], or approximated by a series of rate equations [243]. Herein I will present the master equation approach since it more naturally includes the influence of dissipation. In this formalism the time evolution of the density operator, ρ, is given by

$$\dot{\rho} = -\frac{i}{\hbar}[H, \rho] + \mathcal{L}, \tag{4.1}$$

where the Hamiltonian H describes coherent evolution and the Lindblad operator $\mathcal{L}$ describes dissipation.

An insightful model is made using the simplifying assumptions that the atom is in a harmonic potential interacting either with the coherent drive of the Raman beams, or a dissipative term from the OP beams. The time-dependent

Hamiltonian includes the coherent terms from the harmonic confinement, the internal atomic spin state, and an interaction term describing the influence of the Raman beams [244]:

$$H = \sum_n n\hbar\omega|n\rangle\langle n| \otimes \mathcal{I} - \mathcal{I} \otimes \frac{\hbar\delta\sigma_z}{2} + H_{\mathrm{R}}. \tag{4.2}$$

Here ω is the trap frequency of the harmonic potential with motional levels $|n\rangle$, δ is the 2-photon detuning, and σ_z is the third Pauli spin operator. We drop the ground state energy $\frac{\hbar\omega}{2}|\downarrow; n=0\rangle\langle\downarrow; n=0|$ which provides an arbitrary offset. The interaction Hamiltonian from the Raman beams couples the motional levels with the internal spin states [245]:

$$H_{\mathrm{R}} = \frac{\hbar\Omega_{\mathrm{R}}}{2}\left(e^{i\eta(a+a^\dagger)} \otimes \sigma^+ + e^{-i\eta(a+a^\dagger)} \otimes \sigma^-\right). \tag{4.3}$$

The momentum kick from a photon-scattering event is $\hbar\Delta k = \hbar|\mathbf{k}_\pi - \mathbf{k}_\sigma|$, with $\Delta k\hat{x} = \eta(a+a^\dagger)$ for Raman LD parameter η. We introduce the spin-flip operator $\sigma^\pm = \sigma_x \pm i\sigma_y$. The rate at which population is transferred between motional states is defined by the Rabi frequency [246]:

$$\Omega(n,m) = \Omega_{\mathrm{R}} e^{-\eta^2/2}\sqrt{\frac{n_<!}{n_>!}}\eta^{|n-m|}L_{n_<}^{|n-m|}(\eta^2). \tag{4.4}$$

Here $n_<$ is the smaller of the motional levels $\{n,m\}$, and $n_>$ is the larger. The Raman Rabi frequency, $\Omega_{\mathrm{R}} = \Omega_\pi\Omega_\sigma/(2\Delta_{\mathrm{R}})$, depends on the single-photon Rabi frequencies, Ω_π and Ω_σ, and the single-photon detuning from the $P_{3/2}$ manifold, Δ_{R}. $L_{n_<}^{|n-m|}(\eta^2)$ is an associated Laguerre polynomial [247]. In the LD regime we can simplify $\Omega(n,n-1) \simeq \eta\sqrt{n}\Omega_{\mathrm{R}}$ [248]. The dependence of $\Omega(n,m)$ on both the initial and final motional levels has two important consequences. Firstly, the coupling depends on the order of the sideband transition $|n-m|$, a fact that we will revisit in Section 4.7. Secondly, the coupling depends on the motional level n, leading to thermal dephasing when the initial motional state is sampled from a thermal distribution.

The OP step is modelled by a Lindblad operator that describes dissipation. We assume that each OP step scatters 3 photons [156], giving

$$\gamma_{OP} = \sqrt{\Gamma_{OP}}\left(e^{i\eta_{\mathrm{OP}}(a+a^\dagger)}\right)^3 \otimes \sigma^-. \tag{4.5}$$

Γ_{OP} is the scattering rate of the OP beam, and the recoil from the OP photons (spontaneously emitted in a dipole radiation pattern) defines the

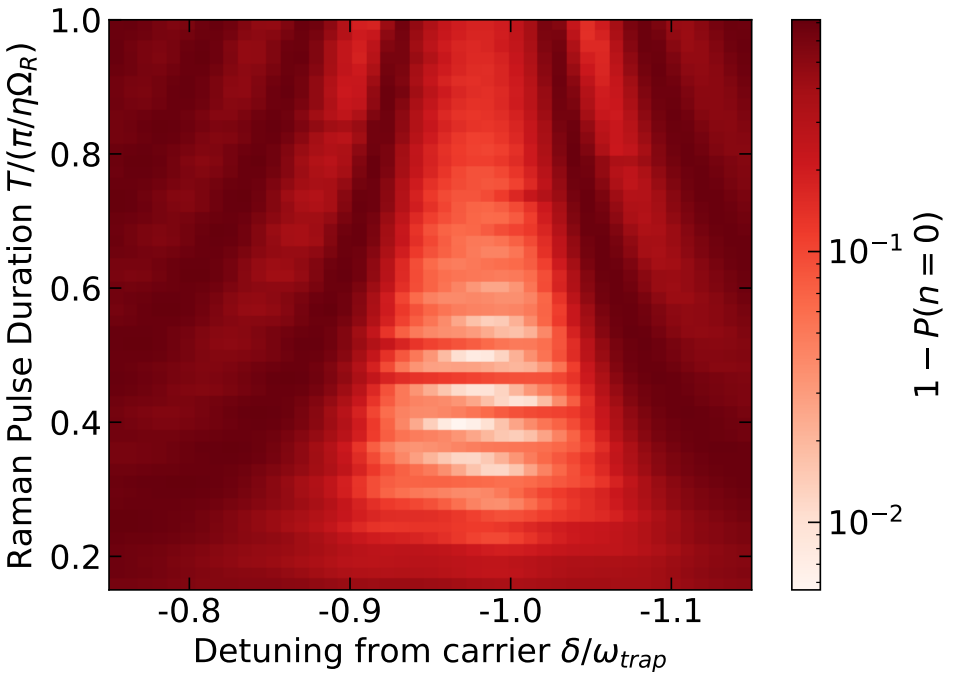

Figure 4.3: Simulations of the master equation calculate the probability of not occupying the ground state after a series of RSC pulses. 30 pulses of the same duration are applied, taking $\omega = 2\pi \times 120$ kHz, $\eta = 0.131$, and $\Omega_R = 2\pi \times 25$ kHz. The detuning is optimal at the carrier-dressed RSB transition. The pulse duration, τ, is optimal close to a π-pulse for the motional level $|n = 3\rangle$.

OP LD parameter η_{OP}. Using γ_{OP} we form the Lindblad operator:

$$\mathcal{L} = \gamma\rho\gamma^\dagger - \frac{1}{2}\rho\gamma^\dagger\gamma - \frac{1}{2}\gamma^\dagger\gamma\rho. \tag{4.6}$$

We have simplified the discussion to a single dimension. The generalisation to 3D is trivial, but since the directions are independent we retain the simplicity of using 1D and analyse each direction separately.

Two of the model parameters are particularly important for effective ground-state cooling: the two-photon detuning δ, and the Raman pulse duration τ. Fig. 4.3 displays the results of numerical simulations using QuTiP [249]. The aim is to minimise the probability of occupying motional states with $n > 0$. The initial state is taken to be a thermal distribution with a temperature of $15\,\mu$K corresponding to an average motional level $\langle n\rangle = 2.13$ when the trap

angular frequency is $\omega = 2\pi \times 120\,\mathrm{kHz}$ (a representative trap frequency for the radial direction). The state evolves under the Raman interaction Hamiltonian for a duration τ with a detuning close to the RSB transition, transferring population down a motional level. Then the Raman interaction is removed ($\Omega_\mathrm{R} = 0$) and the OP is turned on with $\Gamma_\mathrm{OP} = 100\,\mathrm{ms}^{-1}$ for a duration of $2\pi/\Gamma_\mathrm{OP} = 63\,\mu\mathrm{s}$ so that the spin state is reset with $> 99\,\%$ probability. The pair of pulses repeats 30 times, at which point the motional ground state occupation probability is approximately saturated as the cooling from the RSB pulse balances the heating from the OP pulse. The first thing to note is that the cooling is most efficient when the detuning is made resonant with the RSB transition; $\delta_\mathrm{RSB} = -\omega + \Omega_\mathrm{R}^2/2\omega$ (where the second term comes from the carrier dressing of the sideband transition). When detuned from the RSB transition, the Raman beams drive oscillations between states at the generalised Rabi frequency, $\Omega_\mathrm{g} = \sqrt{\delta^2 + \Omega(n,m)^2}$. The increase in the generalised Rabi frequency when detuned results in a broad fringe pattern; the cooling is worst when the change in generalised Rabi frequency means that the chosen pulse duration drives a 2π rotation. Secondly, the optimal pulse duration is approximately a π-pulse for $|n = 3\rangle$: $\tau_\pi(3,4) = \pi/\Omega(3,4) \simeq \pi/\sqrt{4}\eta\Omega_\mathrm{R}$. The optimal π-pulse duration targets a motional level greater than the average motional level of the initial thermal distribution so that the fraction of the population distribution in high-lying motional levels is also cooled. For the parameters of this simulation, the initial thermal distribution has a $1\,\%$ probability of occupying a motional level $n > 12$. The Rabi frequency has vanishing coupling to certain motional levels, resulting in population trapping, which is manifested in the narrow fringe pattern as the pulse duration is varied. Nevertheless, the simulation predicts a range of pulse durations and two-photon detuning for which high-fidelity ground state preparation is achieved.

Another important parameter is the trap frequency ω, which determines the motional energy-level spacing $\hbar\omega$ and the LD parameter $\eta = \sqrt{\omega_\mathrm{recoil}/\omega}$. As presented so far, our model suggests that increasing the trap frequency should be beneficial. For example, there is a reduced probability of motional excitation during the OP step, and the Rabi frequency for the sideband transition will have a weaker dependence on the motional level. However,

achieving a larger trap frequency requires increasing the tweezer intensity, which increases the heating rate due to intensity noise. This is one of several practical considerations not included in the model.

4.4 Sources of Heating

The RSC protocol performs best when heating rates are minimised. The final motional ground state occupation probability depends on the balance between cooling and heating rates. In our realisation of the RSC protocol care has been taken to minimise heating rates from various sources.

Off-resonant single-photon scattering from the Raman beams is detrimental to cooling. Firstly, the scattering event causes atomic recoil, as does the subsequent spontaneous decay from the excited state. Secondly, the spin state is likely to change and must be reset with an OP step before cooling can continue. The single-photon scattering rate is greatly suppressed by setting the frequency of the Raman lasers far-detuned from the transitions to the $P_{3/2}$ manifold: $\Delta_R > 40\,\mathrm{GHz}$.

Off-resonant two-photon Raman transitions can be similarly detrimental to cooling. These undesired transitions reduce the cooling rate by skipping a cooling step and necessitating another OP step to reset the spin, which has associated heating from photon recoil. The effect is simulated in our model and can be mitigated by controlling the spectral width using temporally shaped pulse profiles (see Section 4.6).

To perform efficient RSC it is crucial to reduce motional excitation while changing the spin state. A limiting factor is the spin-motion coupling introduced by the vector light shift of the optical tweezer trap [155, 221]. For a linearly polarised tweezer, the tight focusing of the light introduces some ellipticity to its polarisation around the focus, resulting in a vector light shift equivalent to a nonuniform magnetic field [149, 150, 250]. As the vector light shift has a spatial dependence, there is an effective magnetic field gradient that offsets the trap centre for different m_f states. The displacement in the trap centre for a spin flip with $\Delta m_f = 1$ between hyperfine states is similar to the ground-state atomic wavepacket size. Therefore, there is a high prob-

ability of motional excitation during the OP step. In our setup, the tweezer polarisation is set along the x-axis which results in an effective magnetic field that points in the y-direction. We suppress the effective field gradient, and consequently the spin-motion coupling, by applying a magnetic field of 4.8 G along the x-direction during OP and RSC which is perpendicular to the effective magnetic field [150]. This applied magnetic field contributes $\lesssim 1$ mG of magnetic field noise and we measure drifts in the ambient field of order 1 mG from day-to-day.

After mitigating the vector light shifts, the remnant heating from OP is due to recoil from photon scattering. If the polarisation of the OP beams is impure, then more photon scattering events are required to reach the same probability of occupying the dark state. The effect of OP polarisation purity is quantified in Section 4.8.

The tweezer trap introduces decoherence and heating which scale with the trap depth. The desire to mitigate these detrimental effects motivates the design of a cooling protocol which performs well at relatively low trap depths.

4.5 Reducing the Trap Depth

Our RSC protocol uses a sequence of Raman pulses to cool an atom to the motional ground state, starting from outside the LD regime. In order to accomplish this, the Raman pulses are shaped with a smoothed temporal profile and the pulse sequence targets several different sideband transitions. Using these techniques enables cooling at lower trap depths where both the decoherence caused by differential light shifts and the heating from photon scattering are reduced. More specifically, lowering the trap depth can increase the effectiveness of RSC by increasing the cooling rate and reducing heating rates. The cooling rate is proportional to the sideband transfer efficiency, which is improved by reducing dephasing from differential light shifts that scale proportional to the trap depth [150, 225]. The differential light shifts are significant in our case because the tweezers are near-detuned to ensure species-selectivity [98]. Furthermore, the heating rates from tweezer photon scattering, intensity noise, and pointing noise are reduced by using lower

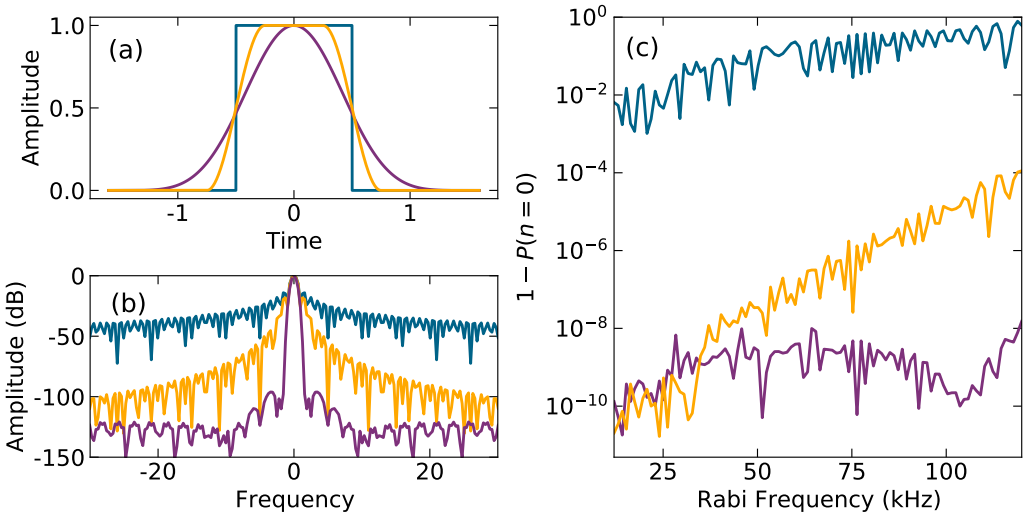

Figure 4.4: The temporal and spectral profiles of different pulse shapes. (a) The Tukey (with a cosine fraction of 2/3) and Blackman-Harris pulse shapes have the same pulse area as a square pulse if the durations are 1.5 and 2.79 times longer respectively and the peak amplitude is the same. (b) The Fourier spectrum of a square pulse demonstrates broad sidelobes. The temporal smoothing of the Tukey and Blackman-Harris pulse shapes suppresses the sidelobes. (c) Starting in $|n = 0\rangle$, the probability of excitation after applying a Raman pulse on the RSB increases with the Rabi frequency, Ω_{R}. The peak Rabi frequency is scaled to keep the pulse area the same for the different pulse profiles. The pulse shapes with a broad Fourier spectrum have a higher probability of excitation. The trap frequency is $\omega = 120\,\mathrm{kHz}$ and the pulse duration is $\tau = \pi/\eta\Omega_{\mathrm{R}}$, with LD parameter $\eta = 0.13$.

trap depths [218, 251]. Finally, given the practical limit of maximum tweezer power available, using less power per trap allows the production of larger arrays. Therefore there is high incentive to design a cooling protocol that works for shallow traps where the atom is initially outside the LD regime. Below we provide more details of the measures we have implemented to overcome the challenges of implementing RSC in relatively shallow traps.

4.6 Pulse Shaping

Pulse shaping is required when using lower trap depths to reduce the probability of off-resonant Raman carrier or BSB transitions. Lowering the trap depth decreases the sideband splitting such that the finite width of the Raman pulse's Fourier spectrum results in an increased probability of off-resonant excitation. These undesired transitions reduce the cooling rate by skipping a cooling step and necessitating another OP step to reset the spin, which has associated heating from photon recoil.

A suitable pulse shape is chosen based on the balance between its spectral width and the temporal duration required to achieve a π-pulse. Fig. 4.4(a) compares a square pulse profile to a Blackman-Harris profile and a Tukey profile with cosine fraction 2/3 [252]. The first consideration is to minimise the spectral width to avoid off-resonant excitation from two-photon Raman transitions. The abrupt change in amplitude of the square pulse results in the appearance of sidelobes in the Fourier spectrum in Fig. 4.4(b). The Tukey profile smooths the edges of the pulse to suppress sidelobes:

$$A(t) = \begin{cases} \frac{1}{2}\left[1 - \cos\left(\frac{2\pi t}{a\tau}\right)\right] & \text{for } 0 \leq t \leq a\tau/2 \\ 1 & \text{for } a\tau/2 < t < \tau(1 - a/2) \\ \frac{1}{2}\left[1 - \cos\left(\frac{2\pi t}{a\tau}\right)\right] & \text{for } \tau(1 - a/2) < t \leq \tau \end{cases} \tag{4.7}$$

The pulse area is $a = 2/3\times$ that of a square pulse with the same pulse duration and peak amplitude. The Blackman-Harris profile is shaped to minimise the sidelobes in the Fourier spectrum:

$$A(t) = 0.35875 - 0.48829\cos\left(\frac{2\pi t}{\tau}\right) + 0.14128\cos\left(\frac{4\pi t}{\tau}\right) - 0.01168\cos\left(\frac{6\pi t}{\tau}\right). \tag{4.8}$$

The pulse area is $0.35875\times$ that of a square pulse with the same pulse duration and peak amplitude. Fig. 4.4(c) displays the results of solving the Schrödinger equation for the application of a Raman π-pulse on the RSB, having started in the motional ground state. Here we consider the radial direction, using a trap frequency of $\omega = 120\,\text{kHz}$ and LD parameter $\eta = 0.13$. The square pulse profile has a significant probability of off-resonant excitation. The excitation probability is reduced by using a Tukey profile, but still increases with the Rabi frequency. For our radial trap frequencies, the Tukey

profile maintains the minimal excitation given by the Blackman-Harris profile provided that the Rabi frequency is $< 40\,\mathrm{kHz}$. The side effect of smoothing the pulse profile is a lower mean Rabi frequency; in order to achieve the same pulse area either a longer duration or a higher peak Rabi frequency is required. Longer pulses are undesirable as they allow time for spontaneous scattering from the tweezer or the Raman beams. And given that there is limited laser power available for the Raman beams, we choose the Tukey profile for the radial directions so that a lower peak Rabi frequency is required. However, in the axial direction the smaller trap frequency necessitates using a Blackman-Harris profile. In practice, RB1 is always a square pulse, so the Raman coupling is the convolution of the RB2, RB3 or RB4 pulse profile with a square pulse. In the radial directions, the resultant square-root Tukey profile still maintains an acceptable excitation probability of $< 10^{-5}$ for Rabi frequencies $< 30\,\mathrm{kHz}$. However, for the axial direction we shape the RB4 pulse with the square of a Blackman-Harris profile, such that the convolution of RB1+RB4 is a Blackman-Harris profile.

4.7 Higher Order Sideband Cooling

Using shallow trap depths means that the atom starts outside the LD regime, such that the Raman coupling has a stronger dependence on the motional level. In the LD regime, the Rabi frequency has only a weak dependence on the motional level. However, in the axial direction where $\eta_\mathrm{z} \sim 0.3$, the initial thermal distribution with $\langle n_\mathrm{z} \rangle \sim 10$ starts outside of the LD regime. Fig. 4.5(a) shows the result of solving the Schrödinger equation for the application of a Raman pulse on the first RSB, demonstrating population trapping where the Raman coupling vanishes at $n = 35$. In contrast, Fig. 4.5(b)-(d) demonstrate how higher order sideband transitions can be used to achieve strong coupling to motional levels of $n > 20$. The higher order sideband transitions can also achieve a faster cooling rate as they reduce the motional level by several quanta in one step [243]. In order to address a wide range of motional states, the pulse duration is set to a π-pulse for n_max, the motional level that maximises the sideband Rabi frequency: $\tau = \pi/\Omega(n_\mathrm{max}, n_\mathrm{max}+\Delta n)$ where $d\Omega(n_\mathrm{max}, n_\mathrm{max} + \Delta n)/dn = 0$. Cooling from outside the LD regime is

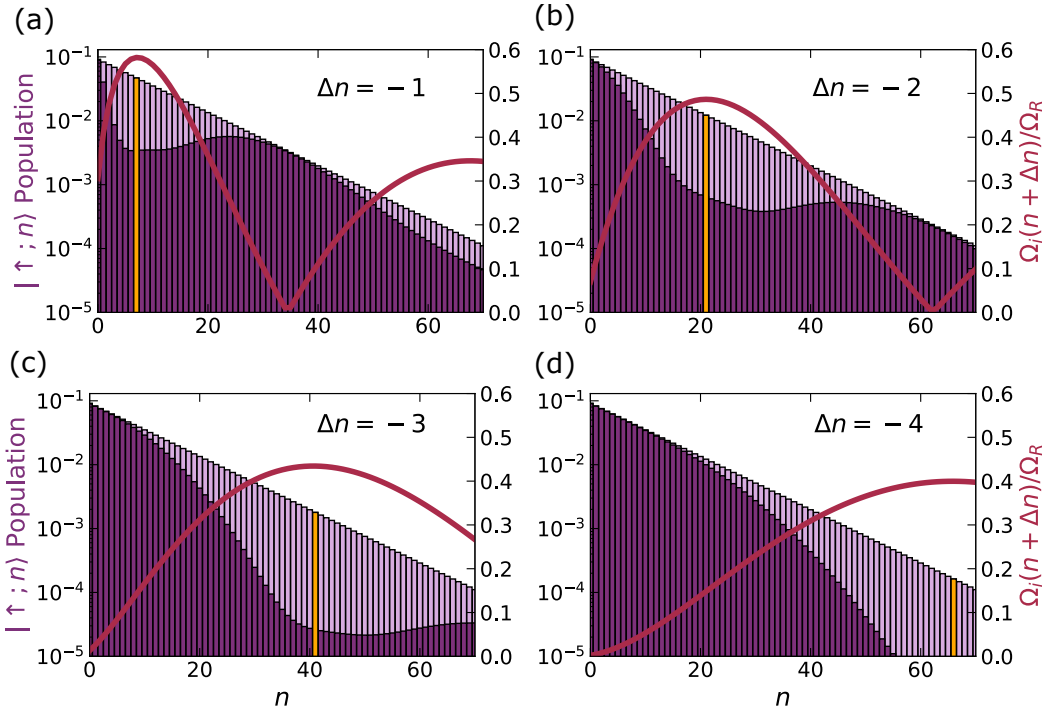

Figure 4.5: Outside of the LD regime, higher-order sideband transitions enable coupling to the full thermal distribution of motional levels. A simulation of applying an $n \rightarrow n+\Delta n$ sideband π-pulse for the motional level, $n_{\max}$, that maximises the sideband Rabi frequency: $\tau = \pi/\Omega(n_{\max}, n_{\max} + \Delta n)$ where $d\Omega(n_{\max}, n_{\max} + \Delta n)/dn = 0$, with a LD parameter $\eta = 0.35$. Lilac: the initial thermal population distribution for the $|\uparrow\rangle$ spin state with $\langle n \rangle = 10$. Purple: The population distribution after applying the Raman pulse. Gold: $n_{\max}$. Red curve: the sideband Rabi frequency Ω normalised by the peak Raman Rabi frequency Ω_{R} demonstrates the variation of coupling as a function of the initial and final motional levels: $\Omega(n+\Delta n)/\Omega_{\mathrm{R}} = |\langle n|e^{i\eta(a+a^{\dagger})}|n+\Delta n\rangle|$. (a) $\Delta n = -1$, $n_{\max} = 7$. (b) $\Delta n = -2$, $n_{\max} = 21$. (c) $\Delta n = -3$, $n_{\max} = 41$. (d) $\Delta n = -4$, $n_{\max} = 66$.

achieved using a sequence of pulses targeting different sideband transitions.

4.8 Optimising the Pulse Sequence

We design a RSC pulse sequence that cools an atom to the 3D motional ground state. To cool the radial axes it is sufficient to use pulses targeting the first RSB. Using a fixed pulse duration achieves a similar fidelity of motional ground-state preparation compared to an optimised routine where each pulse duration is an independent variable [253]. However, having identified that the axial direction involves cooling from outside the LD regime, we use numerical simulations in QuTiP [249] to design an effective RSC protocol.

The first observation is that the start of the pulse sequence should address the upper end of the motional state distribution. The initial thermal distribution with $\langle n \rangle \sim 10$ has a 1 % probability of occupation in a state $|n > 48\rangle$. We address this portion of the population distribution using pulses on the $\Delta n = -4$ RSB until $P(n = 66) < 10^{-3}$. Subsequent groups of pulses address the $\Delta n = -3$ and $\Delta n = -2$ sideband transitions, bunching the population distribution in the lower motional levels. Then the Rabi frequency becomes particularly important in the final stage of the pulse sequence transferring the bunched population distribution into the motional ground state.

The choice of Raman Rabi frequency is a compromise between minimising off-resonant excitation and maintaining robustness against detuning fluctuations. Fig. 4.6 applies 30 repetitions of a set of 3 Blackman-Harris pulses to an initial bunched population distribution resulting from a sequence of higher-order sideband pulses. The Rabi frequency for a Blackman-Harris pulse is time-dependent, but the mean Rabi frequency represents the amplitude of a square pulse with the same pulse duration and the same pulse area. The 3 pulses have durations and frequencies which address $n = 21$ using the $\Delta n = -2$ sideband, $n = 7$ using the $\Delta n = -1$ sideband, and $n = 1$ using the $\Delta n = -1$ sideband respectively. Before each pulse the two-photon detuning is sampled from a normal distribution with standard deviation 3 kHz to simulate realistic experimental noise. The mean of the normal distribution is detuned by (0, 2, or 4) kHz from the relevant RSB transition to simulate

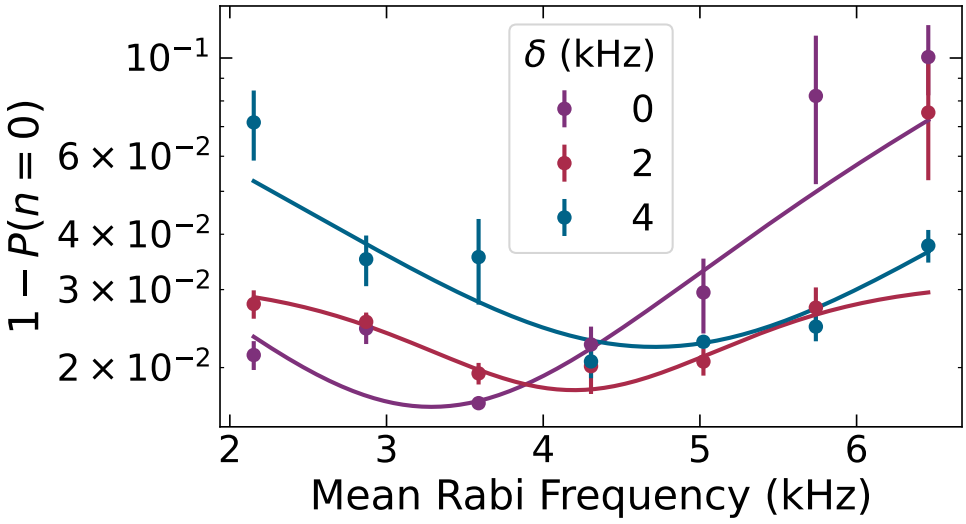

Figure 4.6: Simulation of an axial RSC pulse sequence in the presence of detuning fluctuations. A set of 3 pulses with π-pulse duration for $n = 21, 7,$ and 1 on the $\Delta n = -2, -1,$ and -1 sidebands respectively is repeated 30 times. Before each pulse the two-photon detuning, δ, is sampled from a normal distribution with standard deviation 3 kHz and mean as shown in the legend. A mean Raman Rabi frequency of 4 kHz maintains high-fidelity ground state preparation even with finite detuning from the RSB transitions.

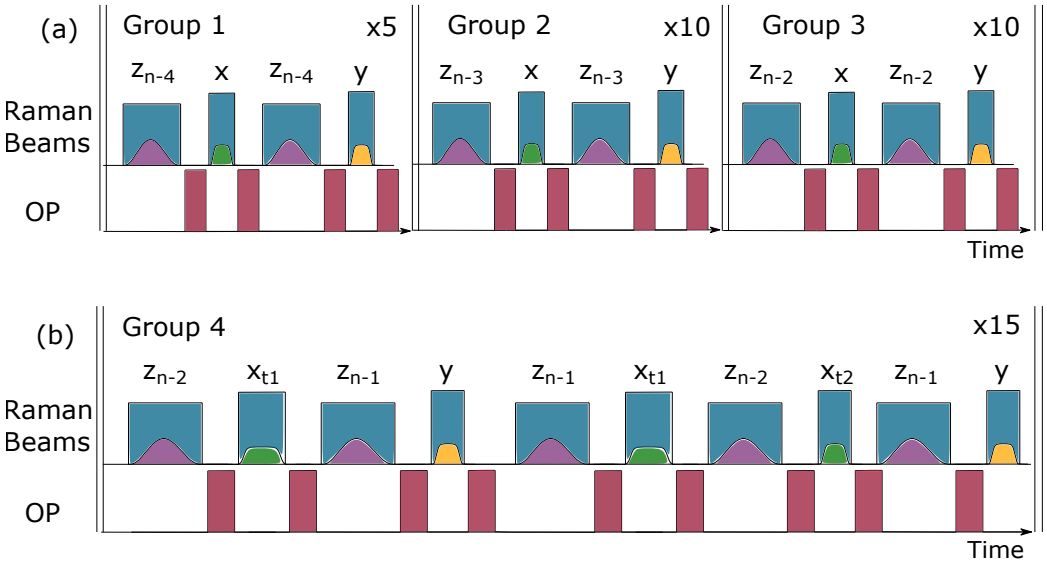

Figure 4.7: Overview of the final RSC pulse sequence. The sequence is split into groups that are repeated, and each group alternates pulses between a pair of Raman beams and an OP step. The labels denote the axis (x,y,z) addressed by each beam pair. The subscripts on z denote which axial sideband transition is driven. (a) Groups 1, 2, and 3 have the same format. RB1 (blue) uses a square pulse, whereas RB2 (green) and RB3 (yellow) use a Tukey pulse shape and RB4 (purple) uses the square of a Blackman-Harris pulse shape. (b) The pulse structure used for group 4 of the full sequence. Here we target the $n-2$ and $n-1$ sidebands in the axial direction, and the inner radial direction (x) uses two different durations denoted by the subscripts t1 and t2.

long-term drifts in beam powers affecting the sideband transition frequency. The errorbars in Fig. 4.6 correspond to the standard deviation of 3 repeats. If the Raman Rabi frequency becomes too similar to the trap frequency (here $\omega = 20\,\mathrm{kHz}$), the cooling efficiency is impeded by off-resonant excitation on the carrier transition. However, reducing the Rabi frequency reduces the width of the sideband transition. A narrower sideband transitions implies an increased sensitivity to changes in the two-photon detuning. Therefore, guided by simulations, we compromise by choosing a mean Rabi frequency of 4 kHz for the axial direction.

We bring the previous considerations together to construct a pulse sequence that cools an atom to the 3D motional ground-state starting from an initial

temperature of 10-30 μK. The resulting pulse sequence, displayed in Fig. 4.7, is composed of 4 groups of pulses which are repeated 5, 10, 10, and 15 times, respectively. Groups 1, 2, and 3 have the form shown in Fig. 4.7(a). The radial pulses target the $n-1$ sideband with a duration that corresponds to a π-pulse for atoms in $n = 3$. In the axial direction, the pulse duration is chosen to maximise the Raman coupling for the desired sideband transition: $T = \pi/\eta\Omega(n_{\max}, n_{\max} + \Delta n)$. Group 1 applies pulses on the $n-4$ sideband with $n_{\max} = 66$, group 2 applies pulses on the $n-3$ sideband with $n_{\max} = 41$, and group 3 applies pulses on the $n-2$ sideband with $n_{\max} = 21$. Group 4 is the final set of pulses illustrated in Fig. 4.7(b). In the radial direction with the smaller trap frequency, x, we alternate the pulse duration between a π-pulse for $n = 1$ or $n = 3$ on the $n-1$ sideband. In the axial direction, we alternate between pulses on the $n-2$ and $n-1$ sidebands with $n_{\max} = 21$ and $n_{\max} = 7$, respectively. The whole pulse sequence takes 45 ms. See Appendix A for a table with full details of the pulse sequence.

Simulating imperfect polarisation of the OP beams tests the performance of the RSC pulse sequence. In order to obtain efficient ground state cooling, the heating from photon recoil must be minimised. After implementing mitigations, the remaining recoil heating mostly comes from the OP steps, and is minimised when the polarisation is pure so that fewer scattering events are required to pump. To investigate the required level of OP purity, we insert a depump operator in direct opposition to OP [235]:

$$\gamma_{DP} = \sqrt{\Gamma_{DP}}\sigma^{+}\left(e^{i\eta_{OP}(a+a^{\dagger})}\right)^{3}. \tag{4.9}$$

To quantify the required OP purity we run simulations of the aforementioned RSC pulse sequence cooling the axial direction with trap frequency 20 kHz, using Blackman-Harris pulse shapes with a mean Raman Rabi frequency of 4 kHz. The 2-photon detuning is randomised between pulses using a normal distribution with standard deviation 5 kHz. 95 % ground state occupancy is achieved for a ratio of $\Gamma_{OP}/\Gamma_{DP} > 2500$, as plotted in Fig 4.8. Having designed a pulse sequence and constrained the parameters, the next task is to test it with experimental measurements.

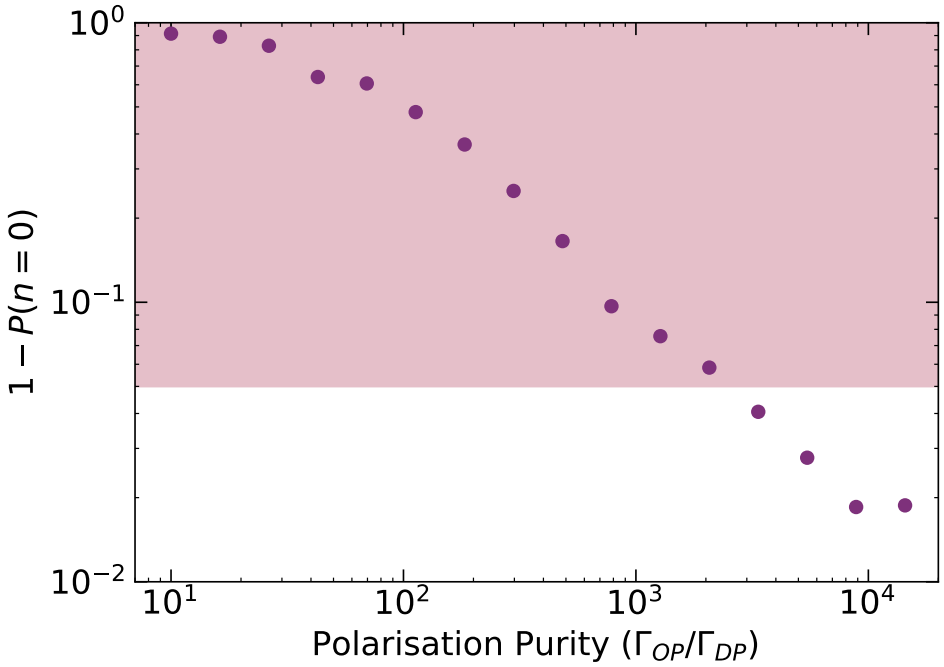

Figure 4.8: Simulation of the effects of polarisation impurity on an axial RSC pulse sequence. A depump operator directly counteracts OP, limiting the dark state fidelity. Here a full axial pulse sequence is simulated with $\omega = 20$ kHz, Blackman-Harris pulse shapes with a mean Raman Rabi frequency 4 kHz, and two-photon detunings repeatedly sampled from a normal distribution with a standard deviation of 5 kHz. A final motional ground state occupation probability of 95 % is achieved when the polarisation purity is better than 2500:1.

Chapter 5

Preparing an Atom Pair in the Motional Ground State

In this chapter we present experimental results verifying the effectiveness of the RSC pulse sequence. Practical considerations for the implementation of a RSC protocol are introduced. Raman sideband spectroscopy is used to determine the 3D motional ground-state fraction. After preparing ground-state atoms in separate optical tweezers, the atoms are merged into a common tweezer with minimal motional excitation. The end product is an atom pair in the relative motional ground state of a common trap; the initial state required for magnetoassociation into a molecular state.

5.1 Experimental Realisation

Some precursor measurements are required in order to find the optimal parameters for the RSC pulse sequence. Namely, we need to know the Rabi frequency and the 2-photon detuning to set for each pulse. As we have seen in the previous chapter, both of these parameters have a significant impact on the cooling efficiency. In this section we will describe the initial measurements required to get a close first estimate of the optimal values.

The AOM frequencies are set to give a 2-photon detuning resonant with the desired sideband transition. The frequency of the transition depends on the light shift from the Raman beam, the differential light shift from the tweezer,

Zeeman shifts from the ambient magnetic field, and the trap frequency. In principle, these quantities can be calculated in advance of any measurement, providing an estimate of the sideband transition frequency.

To more precisely set the AOM frequencies, we measure the sideband spectrum. The measurement involves initiating an atom in a hyperfine sublevel using OP, then pulsing on two of the Raman beams simultaneously at a variable 2-photon detuning (the spectroscopy pulse), and finally applying a pushout pulse to detect whether the spin state of the atom has changed. If the Rabi frequency of the Raman beams is unknown, one might choose a spectroscopy-pulse duration significantly longer than the expected coherence time in order to decrease the chance of unwittingly performing a $2n\pi$ phase rotation and ending in the initial state. The longer pulse durations have the added benefit of decreasing the Fourier width of the pulse, allowing a higher resolution measurement of frequencies. However, the best contrast between sideband peaks and the background is achieved by applying a π-pulse. Red and blue sidebands should be visible in the sideband spectrum when the initial motional state is sampled from a thermal distribution. The AOM frequencies for the RSC pulse sequence are set to target the desired RSB transitions.

Unfortunately, the differential light shift from the tweezer is likely to change as the atom is cooled during RSC and the spatial extent of the atomic wavefunction shrinks [225]. Furthermore, anharmonicity in the trapping potential would broaden and shift the sideband transition for a thermal state [152]. Therefore, it is advisable to optimise the AOM frequencies using a measurement of the motional ground-state fraction.

It is important to set the Raman Rabi frequencies for the beam pairs by choosing appropriate beam powers. The Raman Rabi frequency, $\Omega_R = \Omega_1\Omega_2/2\Delta_R$ can be calculated if the beam waists, beam powers, and transition dipole moments are known quantities. The Rabi frequency of the individual beams can be calculated from their light shift, $\Omega_{1,2}^2/2\Delta_R$, or scattering rate, $\Gamma\Omega_{1,2}^2/4\Delta_R^2$. Alternatively, the Raman Rabi frequency can be directly measured from Rabi oscillations, provided that the coherence time is long enough to measure several periods. After measuring the carrier Raman Rabi frequency for a pair of Raman beams, we adjust the beam powers so that

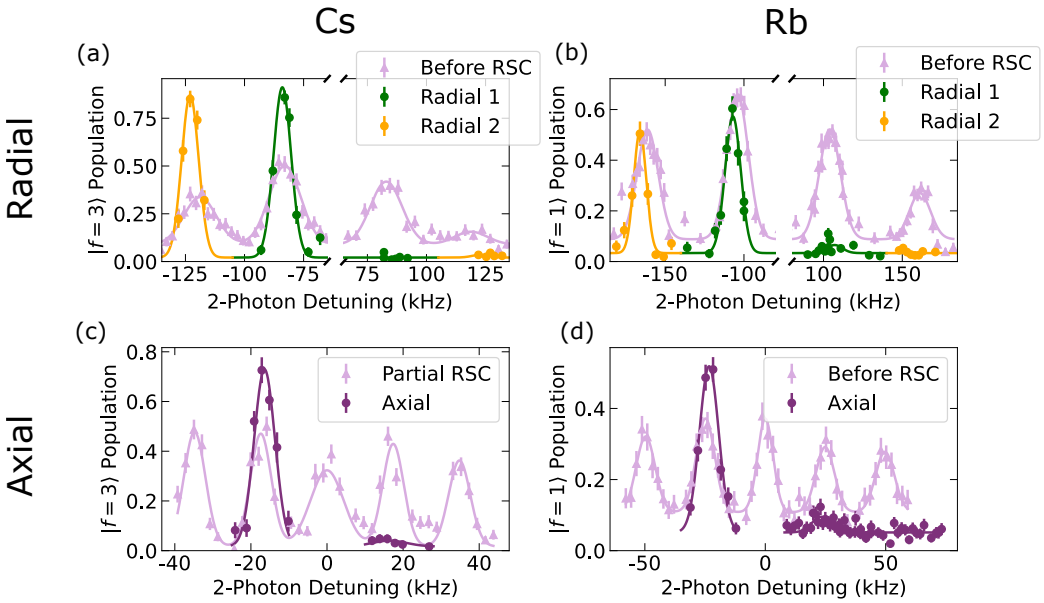

Figure 5.1: Raman sideband spectroscopy before and after the RSC pulse sequence. In (a) and (b) a 100 μs Tukey pulse with RB1+RB3 targets the radial directions. Trap asymmetry allows the two orthogonal radial axes to be resolved. Before RSC, plotted in lilac, both the BSB and RSB transitions are visible. After RSC the amplitudes of the RSB peaks vanish. In (c) and (d) a 400 μs Blackman-Harris pulse with RB1+RB4 targets the axial direction. Initially, the atom is outside of the LD regime, as is manifest in the visibility of higher order sideband transitions. The lilac line in (c) was taken after applying part of the RSC protocol on the $n-4$ and $n-3$ sidebands. The nonzero offsets in (a)–(d) are attributed to spin-changing photon-scattering events and imperfect state preparation and detection.

the sideband π-pulse durations for Rb and Cs are similar. A table of the parameters used for our RSC pulse sequence is given in Appendix A.

5.2 Ground-state Cooling in Separate Traps

The majority of the results and discussion in the rest of this chapter are taken from the author's work in Ref. [166], based on experiments before the new dichroic mounts and 2D AOD were installed.

The RSC pulse sequence is designed for high-fidelity preparation of single atoms in the motional ground state. We confirm the effectiveness of the RSC pulse sequence using sideband thermometry in Fig. 5.1. Assuming a thermal distribution, the ratio of the RSB and BSB peak amplitudes gives the probability of occupying the motional ground state $P(n=0) = 1 - A_{\mathrm{RSB}}/A_{\mathrm{BSB}} = 1 - \langle n\rangle/(\langle n\rangle + 1)$, where $\langle n\rangle$ is the mean motional level [254]. Once the RSC protocol has transferred the atom to the motional ground state, the probability of driving a RSB transition vanishes. The difference between the sideband spectra before and after applying RSC is clearly manifest in Figure 5.1. Panels (a) and (b) show data from experiments using a 100 μs pulse with RB1+RB3 to target the radial directions. Panels (c) and (d) show data from experiments using a 400 μs pulse with RB1+RB4 to target the axial direction and in this case higher order sideband transitions are visible because the atom starts outside the LD regime. After RSC, we extract mean motional levels of $\{n_{\mathrm{x}}, n_{\mathrm{y}}, n_{\mathrm{z}}\}_{\mathrm{Cs}} = \{0.000^{+0.014}_{-0.000}, 0.02^{+0.02}_{-0.02}, 0.03^{+0.03}_{-0.02}\}$ for Cs, and $\{n_{\mathrm{x}}, n_{\mathrm{y}}, n_{\mathrm{z}}\}_{\mathrm{Rb}} = \{0.06^{+0.02}_{-0.02}, 0.00^{+0.04}_{-0.00}, 0.10^{+0.02}_{-0.02}\}$ for Rb. This corresponds to a 3D motional ground-state fraction of $0.95^{+0.03}_{-0.04}$ for Cs in a 2 mK deep 938 nm trap, and $0.86^{+0.03}_{-0.04}$ for Rb in a 1.5 mK deep 814 nm trap. The distribution after RSC is not thermal, but the sideband ratio method is still expected to give a sufficiently accurate estimate of the ground-state probability.

5.2.1 Robustness of the Raman Sideband Cooling Protocol

The RSC protocol is resilient against fluctuations in the two-photon detuning and Rabi frequency. This resilience is achieved by applying enough pulses to saturate the ground-state probability. The required number of pulses depends on the detuning from two-photon resonance and the pulse duration, but in the radial direction we can saturate the ground-state probability after $\sim$ 30 pulses. Our protocol uses 55 pulses on each radial axis so that the radial sideband detuning can drift by 6 kHz with minimal effect on the final ground-state probability given the 20-30 kHz Rabi frequencies. Similarly, the axial sideband detuning must be set to within 2 kHz. This insensitivity to frequency offsets is promising for the extension of this scheme to larger arrays;

normalisation of the array's trap intensities to within 10% should result in comparable cooling performance across the array. The Raman beam powers fluctuate by $< 3\,\%$ ($< 2\,\mathrm{kHz}$ change in light shift), such that the variations in the two-photon Rabi frequency and two-photon detuning are within the boundaries previously stated. Furthermore, the reported 3D ground-state probabilities are achieved when simultaneously cooling Rb and Cs, demonstrating that crossover effects from the influence of the 780 nm light on the Cs RSC, or 852 nm light on the Rb RSC are negligible. All together, our simultaneous RSC protocol is a robust method of achieving 3D ground-state probabilities of $> 80\%$ for both species.

It is possible to further increase the robustness of the RSC protocol by repeating the pulse sequence. Over a period of several weeks, this can save time correcting for changes in the optimal 2-photon detunings. Naturally, by avoiding optimising the detunings one concedes a lower final ground-state fraction. Nevertheless, we found that using two repeats of the RSC protocol instead of optimising the detunings gave a typical 3D ground-state probability of $\gtrsim 80\%$ for both atomic species. The results in this work were taken shortly after experimental optimisation of the parameters to demonstrate the best performance of the RSC protocol.

The use of both RB2 and RB3 in the pulse sequence is not strictly necessary. As previously stated, the geometry of the Raman beams means that the wavevectors of both RB1+RB2 and RB1+RB3 have a finite projection onto both trap axes. The trap asymmetry means sideband transitions along both radial axes can be spectrally resolved. It follows that only one of RB2 or RB3 is required for the RSC protocol. Although the measurements in this chapter use both RB2 and RB3, we subsequently verified that the cooling protocol reaches the same final ground-state fraction using only RB2.

5.2.2 Dephasing of Rabi Oscillations

The effectiveness of the RSC protocol can be seen by examining Rabi oscillations on the Raman carrier transition before and after cooling. Fig. 5.2 displays a measurement of carrier Rabi oscillations of a Rb atom using RB1+RB3 which can couple to the motion in the radial direction. The

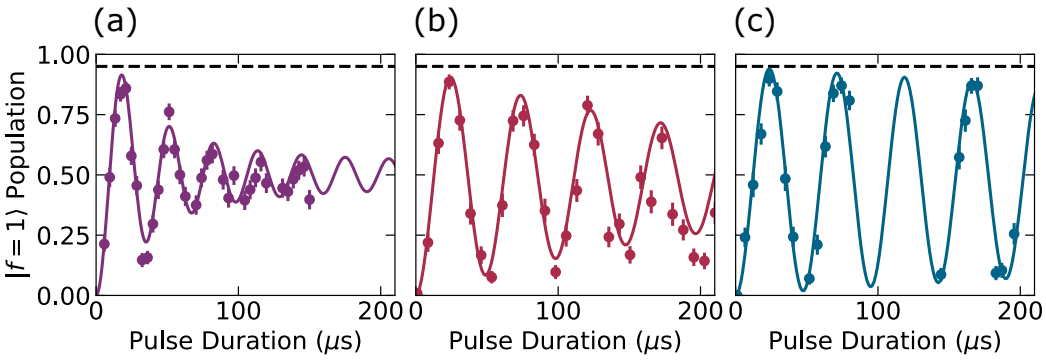

Figure 5.2: Carrier Rabi oscillations for a Rb atom with and without applying the RSC pulse sequence. (a) In an 814 nm tweezer without applying RSC we fit a temperature of 25(2) μK and a Raman Rabi frequency of 32.8(3) kHz. Strong thermal dephasing is evident, so fitting a damped sine gives a 1/e time of 0.053(8) ms. (b) In an 814 nm tweezer after applying RSC the thermal dephasing is removed and we fit a Rabi frequency of 20.32(11) kHz and a 1/e time of 0.25(4) ms. The remaining dephasing is due to the spread of differential light shifts from the tweezer. (c) The effect of differential light shifts is reduced by trapping in a 938 nm tweezer, which is much further detuned from atomic transitions. We fit a damped sine with Rabi frequency 21.06(9) kHz and 1/e time 1.2(6) ms. This data was taken using RB1+RB2, where RB1 uses a square pulse shape and RB2 uses a Tukey pulse shape. The dashed line shows the expected state preparation and detection fidelity of 0.95.

carrier Rabi frequency can be evaluated using Eq. 4.4 with $m = n$. Without applying the RSC pulse sequence, the thermal distribution of motional levels leads to a distribution of Rabi frequencies and hence causes dephasing. This is evident in Fig. 5.2(a), taken in an 814 nm tweezer without any RSC, where fitting a damped sine function allows us to extract a $1/e$ time of 0.053(8) ms. We can extract the temperature by instead fitting a sum over the Rabi oscillations from the different motional levels [149];

$$P_{F=1}(t) = \sum_n P_{\mathrm{MB}}(n, T) \left[1 - \cos(\Omega_{\mathrm{r}}(n, n)t)\right]/2, \tag{5.1}$$

where $P_{\mathrm{MB}}(n, T)$ is the Boltzmann probability of occupying motional state n for a thermal distribution with temperature T. We include the coupling to both radial axes using $\Omega_{\mathrm{r}}(n, n) = \Omega_{\mathrm{x}}(n, n)\Omega_{\mathrm{y}}(n, n)/\Omega_{\mathrm{R}}$ in order to extract the mean temperature. We fit a Raman Rabi frequency of 32.8(3) kHz and a temperature of 25(2) μK. For comparison, the mean temperature from the radial sideband spectroscopy before RSC shown in Fig. 5.1(b) is 15(2) μK. Typically, we expect a temperature of $\sim 30\,\mu$K, as measured using the release and recapture method.

Fig. 5.2(b) shows the extended coherence time of carrier Rabi oscillations straight after applying the RSC protocol in the 814 nm tweezer. The fitted 1/e decay time is 0.25(4) ms. In a precursor sideband thermometry measurement we measured a motional ground state probability of $0.86^{+0.06}_{-0.06}$. This high fidelity preparation into the motional ground state removes the effect of thermal dephasing. We attribute the remaining dephasing to a combination of factors stemming from the bare diode laser source used for the tweezer. Firstly, the tweezer wavelength of 814 nm is relatively near-detuned to the Rb D1 and D2 lines, leading to significant differential light shifts of ~ 15 kHz. Secondly, we measure increased broadband intensity noise on the tweezer light after it has passed through the optical fibre which delivers light to the experiment and a subsequent polariser. We believe this noise originates from multiple modes propagating in the fibre. Together, these factors result in an enhanced spread of differential light shifts and increased dephasing. Note that this additional dephasing is also present in Fig. 5.2(a), meaning that the fitted temperature is likely an overestimate. To confirm that the additional dephasing is a result of differential light shifts from the tweezer, Fig. 5.2(c)

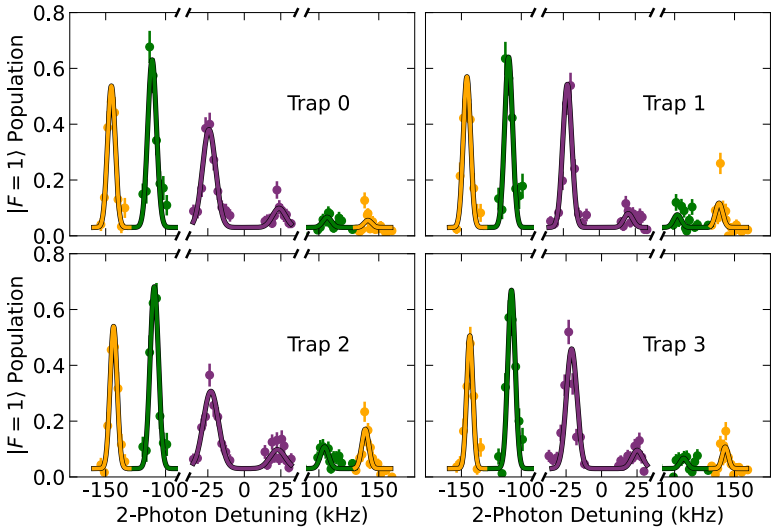

Figure 5.3: Sideband spectroscopy of an array of four optical tweezers that trap Rb atoms. Applying the RSC protocol simultaneously to the array achieves a probability of occupying the 3D motional ground state of $0.72^{0.05}_{0.05}$, $0.70^{0.07}_{0.10}$, $0.48^{0.08}_{0.12}$, and $0.67^{0.07}_{0.09}$ for trap 0, 1, 2, and 3 respectively. The tweezer wavelength is 817 nm, different from the wavelength used in the rest of this thesis. The traps are spaced 4 μm apart.

displays Rabi oscillations for Rb in a 938 nm tweezer after applying the RSC protocol, where we extract a $1/e$ time of 1.2(6) ms. The 938 nm tweezer has a similar level of intensity noise, and hence we measure fast dephasing of Rabi oscillations for a Cs atom. Yet for Rb the dephasing due to the tweezer is greatly suppressed owing to the greater detuning from the Rb D1 and D2 lines. We note that the additional dephasing associated with the bare diode laser can be removed by using a single frequency laser source. However, the robustness of our RSC protocol is demonstrated by the fact that we still prepare a single motional state with high fidelity despite the presence of this additional dephasing.

5.2.3 Cooling an Array

In order to prepare an array of ultracold RbCs molecules, we must first prepare an array of atoms in the motional ground state. Installing the 2D AOD in the 817 nm tweezer beam path made it possible to generate an array of

traps for Rb atoms. Fig. 5.3 displays sideband spectroscopy after applying the RSC protocol simultaneously to four tweezers trapping Rb atoms in a 1D array with separation 4 μm. The measured motional ground-state probability is $0.72^{0.05}_{0.05}$, $0.70^{0.07}_{0.10}$, $0.48^{0.08}_{0.12}$, and $0.67^{0.07}_{0.09}$ for trap 0, 1, 2, and 3. The trap frequencies of the array were normalised to within $< 3\%$ of the mean value so that the two-photon detuning was within the bounds of efficient cooling by the RSC protocol; this level of array intensity normalisation has been achieved for arrays of over 100 atoms [255]. The motional ground-state preparation has a lower fidelity than a single trap because of two technical issues that can be easily resolved in future work. Firstly, the intensity noise on the tweezer light previously mentioned increases with the laser power. Secondly, the polarisation purity measured straight after the 2D AOD is reduced by a factor of between 10 - 70 across the array. This leads to a reduction in purity as measured using the atoms and to a decrease in the efficiency of the cooling. After this work we installed a polariser after the AOD to restore the intended linear polarisation. Therefore, we conclude that our RSC protocol is suited for effective cooling of atoms in an array.

5.3 Transferring Atoms to a Common Trap

Once a Rb and a Cs atom have been prepared in the motional ground states of their respective tweezers, the next step on the route to creating molecules is to merge the traps in order to prepare an atom pair in a single optical tweezer. For molecule creation the atom pair must be in the relative motional ground state of the trap. Therefore, it is important that the transportation of the atoms and merging of the traps maintains the motional state. A balance must be found between merging slow enough to avoid motional excitation from the movement and not leaving excess time for photon scattering. Our merging sequence, displayed in Fig 5.4(a), moves the Cs atom in the 938 nm tweezer to the position of a Rb atom in a stationary 814 nm tweezer, before transferring both atoms into a 1064 nm tweezer at the same position. We optimise the merging by decomposing the sequence to isolate the effects on each atom, as described below. We find that in order to avoid heating, we must carefully choose the trajectory and duration of movement for the 938 nm

tweezer in conjunction with the powers of both tweezers.

5.3.1 Choosing a Trajectory

First, we place a limit on the total duration of the merge by considering photon scattering. As previously mentioned, off-resonant scattering from the tweezers causes heating from photon recoil through Rayleigh scattering or changes to the spin state through Raman scattering which necessitates an additional OP step with associated photon recoil. We calculate a heating rate in the axial direction of $0.02\,\text{quanta}\,\text{ms}^{-1}$ for Rb in the 814 nm tweezer with a typical power of 1 mW, and $0.004\,\text{quanta}\,\text{ms}^{-1}$ for Cs in the 938 nm tweezer for a typical power of 4 mW. These heating rates limit the merge duration to a few milliseconds.

Secondly, we consider the limitations on the movement of the Cs atom in the 938 nm tweezer alone. The position of the 938 nm tweezer is dynamically controlled in the x-direction by an AOD, as previously described in Ref. [98, 165]. Chirping the frequency of the RF signal driving the AOD translates the tweezer, but the duration of the sweep must be slow enough to avoid excitation. The probability of excitation depends on the trajectory; a linear sweep has significant jerk, whereas using a minimum-jerk trajectory reduces heating [156, 256]. The minimum-jerk trajectory is given by:

$$x_{\text{mj}}(t, d, \tau) = d\left(10\,(t/\tau)^3 - 15\,(t/\tau)^4 + 6\,(t/\tau)^5\right). \tag{5.2}$$

Where d is the total distance travelled after a duration $t = \tau$. Assuming that the trap frequency remains constant during the merge, the heating caused by the transport is dominated by classical inertial forces. The average quanta of motional excitation from inertial forces after following a minimum-jerk trajectory is given by [257]:

$$\begin{aligned}\langle \Delta n \rangle &= \frac{m}{2\hbar\omega}\left[\left(\int_0^\tau \sin(\omega(\tau - t'))\ddot{x}_{\text{mj}}(t')dt'\right)^2\right. \\ &\qquad \left. + \left(\int_0^\tau \cos(\omega(\tau - t'))\ddot{x}_{\text{mj}}(t')dt'\right)^2\right] \\ &= \frac{md^2}{2\hbar\omega}\frac{14400}{\omega^8\tau^{10}}\left[6\omega\tau\cos(\omega\tau/2) + (\omega^2\tau^2 - 12)\sin(\omega\tau/2)\right]^2.\end{aligned} \tag{5.3}$$

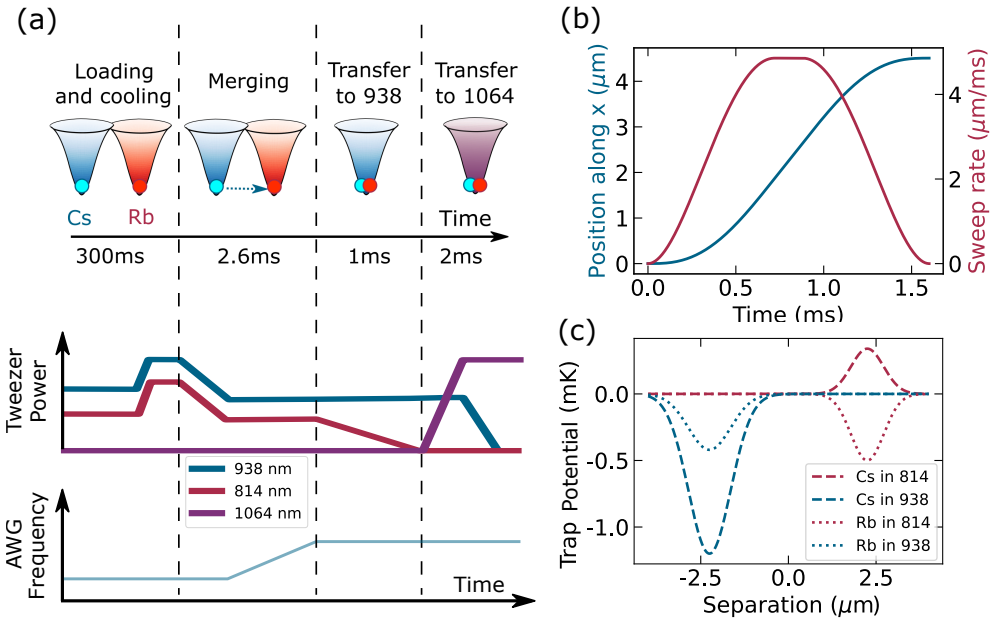

Figure 5.4: (a) The time sequence for merging atoms in the motional ground-state. A Rb atom and a Cs atom are loaded, imaged, and cooled in separate tweezers. The 938 nm tweezer is moved to the position of the 814 nm tweezer and the 814 nm tweezer is ramped off. Subsequently, both atoms are transferred into the 1064 nm tweezer. In order to re-image the atoms, the process is reversed. To avoid pair loss caused by spin relaxation from most combinations of spin states, the sequence is followed while only loading one of the atomic species. The lower time sequence depicts the relative powers of the tweezers. The AWG frequency shows when the 938 nm tweezer is moved to overlap with the 814 nm tweezer. (b) The hybrid minimum-jerk trajectory (blue) moving the 938 nm tweezer a distance of 4.5 μm has a sweep rate (red) that is constant for the central 10 % of the 1.6 ms duration. (c) The potentials experienced by a Rb atom (dotted line) or a Cs atom (dashed line) in the 814 nm tweezer with power $P_{814} = 0.64\,\mathrm{mW}$ (red) or the 938 nm tweezer with power $P_{938} = 3.8\,\mathrm{mW}$ (blue).

A sweep duration of $\tau > 0.11\,\text{ms}$ is required to keep the average motional excitation < 0.01 quanta when transporting a Cs atom with mass $m = 2.21 \times 10^{-25}\,\text{kg}$ a distance $d = 4.5\,\mu\text{m}$ in a 938 nm tweezer with a radial trap frequency $\omega = 2\pi \times (70\,\text{kHz})$. Faster transport while maintaining the motional state is possible using shortcuts to adiabaticity [258–264], but there are other limiting factors in our situation.

Unfortunately, the diffraction efficiency of the AOD has an oscillatory dependence on the driving frequency, F, which can cause resonant intensity modulation at certain sweep rates:

$$\frac{dF}{dt} = \nu_{\text{FSR}}\nu_{\text{trap}}, \tag{5.4}$$

where $\nu_{\text{FSR}} = v_{\text{s}}/(2L)$ is the cavity free spectral range for a cavity of length L with speed of sound v_{s}, and ν_{trap} is the trap frequency in kHz. Intensity noise causes parametric heating when the modulation frequency is $2\nu_{\text{trap}}$, or beam-pointing noise causes heating for a modulation frequency of ν_{trap} [218]. To determine the origin of the heating, we performed release and recapture temperature measurements after a round-trip sweep. The measurements showed significant heating for sweep rates satisfying Eq. 5.4, suggesting that the heating is from beam-pointing noise rather than intensity noise, and that there is a coupling between the tweezer intensity and the position of the atom. This coupling could arise from the presence of strong vector light shifts or the tilting of the trap due to inertial forces during the sweep.

The heating from resonant intensity modulation can be avoided by choosing a constant sweep rate such that the modulation frequency is not close to the trap frequency. However, the linear chirp has significant jerk, which will heat the atom. Therefore, we form a hybrid minimum-jerk trajectory that starts and ends with a minimum-jerk function [156]:

$$x_{\text{hybrid}} = \begin{cases} x_{\text{mj}}(t, 2\Delta f, 2\Delta t) & \text{for } 0 \le t \le \Delta t \\ \frac{15}{4}\frac{\Delta f}{2\Delta t} & \text{for } \Delta t < t < \tau - \Delta t \\ x_{\text{mj}}(t - \tau + 2\Delta t, 2\Delta f, 2\Delta t) + \alpha\tau\frac{15}{4}\frac{\Delta f}{2\Delta t} & \text{for } \tau - \Delta t < t \le \tau \end{cases} \tag{5.5}$$

$$\Delta f = \frac{d}{\left(2 + \frac{15\alpha}{4(1-\alpha)}\right)}. \tag{5.6}$$

Here, Δf is the distance travelled during the minimum-jerk portion of the

trajectory, and $\Delta t = \tau(1-\alpha)/2$ is the time elapsed during each minimum-jerk portion. The fraction of the total duration which follows the linear trajectory ($\alpha = 0$ for fully minimum-jerk and $\alpha = 1$ for fully linear) is colloquially named the hybridicity. Both the duration of the sweep, τ, and the hybridicity, α, determine whether we scan across a bad sweep rate. Fig. 5.4(b) displays a trajectory with a duration of 1.6 ms where the sweep rate is constant for the central 10 %. In this work an AOD with a measured $\nu_{\mathrm{FSR}} = 180(10)$ kHz translates the 938 nm tweezer a distance of 4.5 μm (a frequency chirp of 14 MHz) along a trajectory with a hybridicity of $\alpha = 0.1$. This implies that the intensity modulation will be resonant with the radial trap frequencies of 64 kHz and 92 kHz for sweep durations of 2.1 ms and 1.5 ms respectively. By avoiding these sweep durations we can transport the atom without significant motional excitation.

To maintain both atoms in the motional ground state, we must also consider the effect of combining the potential of the 938 nm tweezer with that of the 814 nm tweezer. We investigate this experimentally using the merging sequence displayed in Fig. 5.4(a). We perform the experiment separately for each atomic species in order to avoid pair loss and interaction shifts complicating the interpretation of the sideband spectra used to measure any heating. The pair loss is a result of spin relaxation from all spin state combinations except when Rb is in $|f = 1, m_f = 1\rangle$ and Cs is in $|f = 3, m_f = 3\rangle$. The final motional state of each atom is sensitive to both the trap depths (set by the tweezer powers, P_{938} and P_{814}) and the overlap of the tweezers. We overlap the tweezers to within 100 nm in both radial directions by pushing out a Cs atom from the 938 nm or 1064 nm tweezer using the repulsive potential of the 814 nm tweezer. With the tweezers well overlapped, we observe that sweep durations longer than 1 ms are required to avoid heating. Therefore we choose a sweep duration of 1.6 ms which avoids resonant intensity modulation without leaving excess time for off-resonant scattering from the tweezer. All that remains is to choose the balance of the trap powers during the merge sequence. The Rb atom could be transferred to an excited motional state if the trap depths of the merging potentials are similar [265]. Alternatively, when the combined potential experienced by Cs is very shallow, the close spacing of axial harmonic levels means there is a high probability of motional exci-

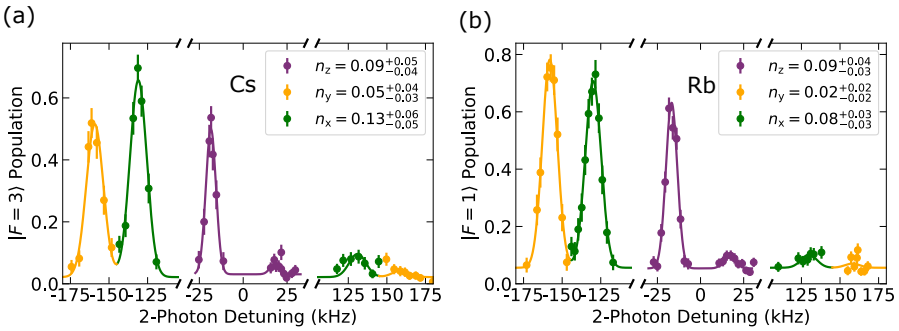

Figure 5.5: Ground state occupation of a Rb atom or a Cs atom in a common 1064 nm tweezer. Raman sideband spectroscopy following the optimised merging sequence described in the text is used to measure a 3D ground-state probability of (a) $0.78^{+0.05}_{-0.06}$ for Cs and (b) $0.83^{+0.04}_{-0.04}$ for Rb.

tation. We explore the balance of trap powers by fixing $P_{938} = 3.8$ mW and varying P_{814}. The powers are adiabatically ramped in 1 ms before merging the traps. The Rb atom starts to spill into the 938 nm tweezer when the power ratio $P_{938}/P_{814} > 7$. In contrast, the trapping potential for the Cs atom vanishes when $P_{938}/P_{814} < 2$. In practice, we find that the heating of the Cs atom is more severe than that of the Rb atom, and a power ratio of $P_{938}/P_{814} \sim 6$ is required.

The last step of the merging sequence transfers the atoms to a 1064 nm tweezer at the same position. An atom in the 1064 nm tweezer experiences a lower scattering rate and therefore permits a greater precision for the sideband thermometry used to assess the merging performance. The wavelength is chosen in anticipation of the subsequent transfer to a molecular state, as the molecular polarisability in the rovibrational ground state is similar to that of the Feshbach molecule at 1064 nm [116, 266, 267].

5.3.2 Estimating the Relative Motional Ground-State Fraction

Finally, we use the constraints previously discussed to determine parameters for merging a Rb atom in its motional ground-state with a Cs atom in its motional ground-state. The tweezer powers are set at $P_{938} = 3.8$ mW and $P_{814} = 0.64$ mW. This power for the 938 nm tweezer gives trap depths of

$U_{\mathrm{Cs}}^{938} = 1.2$ mK and $U_{\mathrm{Rb}}^{938} = 0.42$ mK, whereas the 814 nm tweezer provides a trap depth of $U_{\mathrm{Rb}}^{814} = 0.50$ mK for Rb but functions as a barrier for Cs with $U_{\mathrm{Cs}}^{814} = -0.34$ mK. The separated potentials are plotted in Fig 5.4(c). The trap powers are ramped in 1 ms and the hybrid minimum-jerk trajectory has a duration of 1.6 ms, with 10 % of the total duration being a linear sweep. The whole merging sequence is completed within 6 ms. Testing the sequence with a Cs atom, the mean motional levels extracted from the sideband spectroscopies in Fig. 5.5(a) are $\{n_{\mathrm{x}},\ n_{\mathrm{y}},\ n_{\mathrm{z}}\}_{\mathrm{Cs}} = \{0.13^{+0.04}_{-0.04},\ 0.05^{+0.03}_{-0.03},\ 0.09^{+0.04}_{-0.04}\}$. Repeating the measurements with a Rb atom, we extract mean motional levels of $\{n_{\mathrm{x}},\ n_{\mathrm{y}},\ n_{\mathrm{z}}\}_{\mathrm{Rb}} = \{0.08^{+0.03}_{-0.03},\ 0.02^{+0.02}_{-0.02},\ 0.09^{+0.03}_{-0.03}\}$ from the sideband spectroscopies in Fig. 5.5(b). This corresponds to a 3D ground-state probability of $0.78^{+0.05}_{-0.06}$ for Cs and $0.83^{+0.04}_{-0.04}$ for Rb. While the decrease in ground-state probability of the Rb atom is consistent with heating from tweezer scattering, the optimised parameters have not completely prevented motional excitation of the Cs atom. We expect an increase of 0.028 quanta due to tweezer scattering. Yet, the mean motional level in the x-direction has increased by $0.13^{+0.04}_{-0.04}$ quanta. Most likely this is a consequence of heating from the resonant modulation of the AOD's diffraction efficiency, and the heating is greater than measured with just Cs in the 938 nm tweezer because the trap frequencies are modified when the two tweezer potentials combine.

The proportion of atoms in the relative motional ground state can be estimated using [99]

$$P(n_{\mathrm{rel}} = 0) = \frac{P(n_{\mathrm{Rb}} = 0)P(n_{\mathrm{Cs}} = 0)}{1 - \frac{m_{\mathrm{Cs}}}{m_{\mathrm{Cs}}+m_{\mathrm{Rb}}}\frac{\bar{n}_{\mathrm{Cs}}}{\bar{n}_{\mathrm{Cs}}+1} - \frac{m_{\mathrm{Rb}}}{m_{\mathrm{Cs}}+m_{\mathrm{Rb}}}\frac{\bar{n}_{\mathrm{Rb}}}{\bar{n}_{\mathrm{Rb}}+1}}. \tag{5.7}$$

The derivation of this formula makes three assumptions. Firstly, that the centre-of-mass and relative motion are separable. In the 1064 nm tweezer the Rb and Cs trap frequencies are similar, satisfying $\omega_{\mathrm{Cs}} \approx 1.08\omega_{\mathrm{Rb}}$, such that the centre-of-mass and relative motion are approximately separable. Secondly, that the distribution of motional levels follows a Boltzmann distribution. Thirdly, the derivation ignores interactions between the atoms. While the interactions between the atoms will shift the energy eigenstates [268], the motional ground state that we prepare is adiabatically connected to $|n_{\mathrm{rel}} = 0\rangle$ as the interaction strength is tuned to zero, provided that we can ignore the effects of trap-induced shape resonances [269, 270]. Therefore, the

probability of preparing an atom pair in the relative motional ground state, which becomes $|f_{\mathrm{Rb}} = 2, m_{f,\mathrm{Rb}} = 2; f_{\mathrm{Cs}} = 4, m_{f,\mathrm{Cs}} = 4; n_{\mathrm{rel}} = 0\rangle$ in the limit of weak interactions, is $P(n_{\mathrm{rel}} = 0) = 0.81^{+0.08}_{-0.08}$ following our optimised sequence. Using a MW or a Raman carrier π-pulse before merging, we can transfer to the desired hyperfine spin state with a probability of 0.935(7). Accounting for a 4(1) % probability of spin relaxation for each atom during the merge, we expect that 71(7) % of atom pairs will be transferred into the $|1, 1; 3, 3; n_{\mathrm{rel}} = 0\rangle$ state. This is the state from which magnetoassociation to a molecular state can be achieved following a similar scheme employed with bulk mixtures of Rb and Cs [162, 163].

Chapter 6

Association

Having prepared an atom pair in the relative motional ground state of a single optical tweezer, we now turn our attention towards manipulating the interactions between the atom pair, with the aim of creating a molecule. Coupling between a free atom-pair state and a molecular bound state occurs at a magnetic Feshbach resonance [271–274]. In bulk gas experiments there is a long history of using Feshbach resonances to investigate collisional processes [275, 276], enhance thermalisation rates [277, 278], study many-body physics [120, 279], and provide a method for associating molecules [54, 55, 280–282]. More recently, the association of a single molecule in an optical tweezer has been demonstrated [87, 99, 155].

This chapter will outline background theory and report results from our experiments involving Feshbach resonances. Atomic scattering theory for two-body collisions provides the background for understanding Feshbach resonances. However, for atoms trapped in a tightly-confined optical potential it is also important to consider the effect of the trapping light. The first consideration is that not all of the energy eigenstates of the harmonic potential can associate into a molecular bound state. Secondly, the trapping light can shift the magnetic field at which the Feshbach resonance occurs [283, 284]. Having explored the consequences of these two facts, we will present results verifying magnetoassociation into a molecular state and characterising the lifetime holding the molecule in a trap.

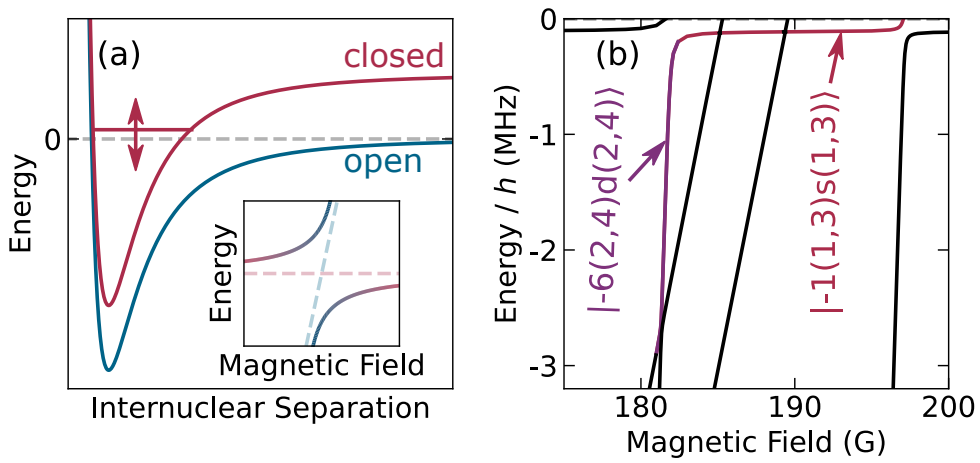

Figure 6.1: Feshbach resonances for a Rb and a Cs atom (a) Elastic collisions between atoms in the open channel can resonantly couple to bound states in the closed channel when their energies become degenerate. Inset: a magnetic field tunes the energy difference between the scattering and bound states until the states mix at an avoided crossing. (b) The energy of relevant RbCs molecular bound states relative to the free atom dissociation threshold. Feshbach resonances occur at 181.6 G and 197.1 G. We access the highlighted molecular states using adiabatic magnetic field ramps.

6.1 Scattering Theory

To understand the physics of Feshbach resonances, we first start with a system of two colliding atoms [134, 214, 285, 286]. The initial quantum state of the atom pair is called the scattering state and is also referred to as the open (or entrance) channel, as displayed in Figure 6.1(a). As the atoms approach each other, the interaction energy follows a potential energy curve, which might permit bound states. Atoms in different quantum states (closed channels) would follow a different potential energy curve. Energies are usually defined with respect to the energy of the scattering state at the dissociation threshold. The following text provides an overview of how elastic collisions in the presence of a Feshbach resonance can change the quantum state so that the atoms transfer to a closed channel. The reader can find further explanation in textbooks on the topic [287–289].

Two atoms interacting in an external magnetic field are described by the Hamiltonian [290, 291]:

$$\hat{H} = \sum_{X=\mathrm{Rb,Cs}} \left[-\frac{\hbar^2}{2m_X}\nabla_X^2 + \sum_{i=x,y,z} \frac{m_X \omega_{i,X}^2 \hat{r}_{i,X}^2}{2} + \hat{H}_X \right] + \hat{V}(R),$$

where m_X is the mass of atom $X = \{\mathrm{Rb,Cs}\}$ with position $r_{i,X}$ and trap frequency $\omega_{i,X}$ in the $i = \{x, y, z\}$ direction. The interaction term $\hat{V}(R)$ depends only on the internuclear separation, R. $\hat{H}_X = A_X \hat{\imath}_X \cdot \hat{s}_X + g_e \mu_\mathrm{B} B \hat{s}_{z,X} + g_n \mu_\mathrm{B} B \hat{\imath}_{z,X}$ is the internal Hamiltonian for atom X with hyperfine constant A_X, nuclear spin $\hat{\imath}_X$, and electron spin $\hat{s}_X$. g_e and g_n are the electron and nuclear g-factors respectively. If we assume that centre-of-mass (COM) and relative motion are separable, the relative coordinates satisfy:

$$\hat{H} = \frac{\hbar^2}{2\mu}\left(\frac{-1}{R}\frac{d^2}{dR^2}R + \frac{\hat{L}^2}{R^2}\right) + \hat{H}_\mathrm{Rb} + \hat{H}_\mathrm{Cs} + \hat{V}(R), \tag{6.1}$$

for reduced mass μ and orbital angular momentum operator $\hat{L}^2$. The interaction term, $\hat{V}(R)$, has two components: an isotropic potential that projects onto the potential energy curves, and a magnetic dipole-dipole interaction between electron spins. The Schrödinger equation can be solved computationally using coupled-channel methods to extract the wavefunction, bound-state energies, and scattering properties [292, 293].

Two parts of the two-body Hamiltonian are of particular importance. Firstly, the energy difference between hyperfine spin states with different magnetic moments can be tuned using a magnetic field. There exists some magnetic field where a vibrational bound state of one spin state becomes degenerate with the other spin state at the dissociation threshold. Secondly, the interaction couples different spin states. The coupling between near-degenerate states strongly modifies the collisional properties.

In certain limits, analytic formulas can be used to determine collisional properties. Scattering theory generally frames the collision in terms of an initial incident plane wave interacting with a static particle. The probability of scattering off the particle is determined by the collisional cross section, which can be expanded in terms of partial waves. For the ultracold collisions discussed in this thesis, the low energies exclude collisions in anything except the lowest partial wave [288, 289]. In this limit, the scattering properties

are determined completely through the scattering length, a. For collisions between distinguishable particles the collisional cross-section is then given by $\sigma = 4\pi a^2/(1+k^2a^2)$ where k is the wavevector [287, 288]. Near to a Feshbach resonance the scattering length is given by the formula [294]:

$$a(B) = a_{\mathrm{bg}}\left(1 - \frac{\Delta B}{B - B_0}\right). \tag{6.2}$$

Here, a_{bg} is the background scattering length away from the resonance, B_0 is the magnetic field at which the resonance occurs, and ΔB characterises the width of the resonance. Around the energies where the scattering length diverges, coupling of the near-degenerate quantum states creates an avoided crossing, as displayed in the inset of Figure 6.1(a). Following the avoided crossing, one can adiabatically transform the quantum state from the open channel into the closed channel.

Magnetoassociation involves a magnetic field ramp across a Feshbach resonance. When the field ramps downwards sufficiently slowly, the avoided crossing permits adiabatic transfer into the bound state, creating a Feshbach molecule (the name refers to the fact that this is a weakly-bound state). The probability of adiabatically transferring to the bound state is $1 - P_{\mathrm{LZ}}$, where the Landau-Zener formula gives [295]:

$$P_{\mathrm{LZ}} = \exp\left(-\frac{\epsilon_{12}^2}{\hbar|\frac{d}{dt}[E_1 - E_2]|}\right). \tag{6.3}$$

Here, ϵ_{12} is the Hamiltonian's off-diagonal matrix element coupling the eigenstates with energies E_1 and E_2. For a pair of atoms in an isotropic harmonic trap, the confinement length scale is given by the harmonic oscillator length, $a_{\mathrm{ho}} = \sqrt{\hbar/\mu\omega}$. When the scattering length satisfies $|a_{\mathrm{bg}}| \ll a_{\mathrm{ho}}$, the Landau-Zener formula can be rephrased in terms of the parameters of the Feshbach resonance [133]:

$$P_{\mathrm{LZ}} = \exp\left(-\omega\sqrt{\frac{24}{a_{\mathrm{ho}}}}\left|\frac{a_{\mathrm{bg}}\Delta B}{\partial B/\partial t}\right|\right). \tag{6.4}$$

Figure 6.1(b) displays Feshbach resonances at 181.6 G and 197.1 G for a Rb-Cs atom pair. Following the red and purple lines transfers into the least-bound state and subsequently a more deeply bound state.

We classify the molecular states by their vibrational level and angular momentum quantum numbers: $|n(f_{\mathrm{Rb}}, f_{\mathrm{Cs}})L(m_{f,\mathrm{Rb}}, m_{f,\mathrm{Cs}})\rangle$. The vibrational

level, n, counts down from from the least bound state: $n = -1$. f_X is the hyperfine level for the atom $X = \{\text{Rb, Cs}\}$ which has a projection $m_{f,X}$ onto the quantisation axis. Finally, L is the quantum number for end-over-end rotation of the molecule which is labelled by $\{s, p, d, f, ...\} = \{0, 1, 2, 3, ...\}$. Using this nomenclature, the least-bound state is $|-1(1,3)s(1,3)\rangle$ and the more deeply bound state is $|-6(2,4)d(2,4)\rangle$. Our model so far describes how atoms in specified spin states interact in a magnetic field and can bind to form a molecule.

6.2 Harmonic Confinement

A full description of the interacting atom pair must include the influence of the trapping potential. We shall see that in order to associate into a molecular state the atom pair must be in a specific motional state, as well as the particular spin state for which the Feshbach resonance occurs.

6.2.1 Fermi Pseudopotential

Consider the system of a heteronuclear atom pair confined in the same 3D harmonic trap. The energy eigenstates are found by diagonalising the Hamiltonian from Equation 6.1. We relate the positions of the separate atoms, $r_{i,X}$, to the relative, R_i, and COM, d_i, coordinates, which can be a more intuitive basis given that the interaction is a function of the separation of the atoms. In the limit of low energy and large separations, R, (relative to the effective range of the interaction) we can approximate the interaction term with a Fermi pseudopotential, $\hat{V}(R) = \frac{2\pi a\hbar^2}{\mu}\delta^{(3)}(\mathbf{R})\frac{\partial}{\partial R}R$, for scattering length a, reduced mass μ, and internuclear separation R [283, 296]. We estimate the validity of using the Fermi pseudopotential by comparing the interaction length scale to the harmonic oscillator length scale. The van der Waals interaction for the RbCs $a^3\Sigma^+$ state has a characteristic length scale $\beta_6 = (2\mu C_6/\hbar)^{1/4} = 10\,\text{nm}$ using $C_6 = 5694 E_\text{h} a_0^6$ for Hartree energy E_h and Bohr radius a_0 [162, 297]. The effective range of the interaction is significantly less than the harmonic oscillator length which is typically $a_{\text{ho,ax}} \sim 100\,\text{nm}$ using axial trap frequencies $\sim 20\,\text{kHz}$, or $a_{\text{ho,rad}} \sim 40\,\text{nm}$ using radial trap

frequencies $\sim 140\,\mathrm{kHz}$.

Using the Fermi pseudopotential with decoupled COM and relative motion, the energy eigenstates are given by analytical formulas for an isotropic [146] or cylindrically-symmetric [298] trap. Optical tweezer traps tend to be cigar-shaped, with the axial confinement being significantly weaker than the radial confinement. For now we assume that the trap is radially symmetric: $\omega_x = \omega_y$. The solutions for the energy levels of the atom pair in a cylindrically-symmetric trap using a Fermi pseudopotential interaction term are given by [298]:

$$-\frac{\sqrt{\pi}}{a} = \mathcal{F}(-(E-E_0)/2, \kappa), \tag{6.5}$$

$$\mathcal{F}(x,\kappa) = \int_0^\infty dt \left(\frac{\kappa e^{-xt}}{\sqrt{1-e^{-t}}(1-e^{-\kappa t})} - \frac{1}{t^{3/2}} \right) \text{ for } x > 0, \tag{6.6}$$

where E_0 is the harmonic oscillator ground-state energy, and $\kappa = \omega_r/\omega_z$. Although the integral is defined for $E < E_0$, it can be extended to $E > E_0$ by analytic continuation. When $\kappa \in \mathbb{N}$, the integral is of the form [298]:

$$\mathcal{F}(x,\kappa) = -2\sqrt{\pi}\frac{\Gamma(x)}{\Gamma(x-1/2)} + \sqrt{\pi}\frac{\Gamma(x)}{\Gamma(x+1/2)} \sum_{m=1}^{\kappa-1} {}_2F_1(1, x; x+1/2; e^{2i\pi m/\kappa}), \tag{6.7}$$

where ${}_2F_1(a,b;c;x)$ is the hypergeometric function, and $\Gamma(x)$ is the Gamma function [299].

Figure 6.2(a) plots the energy eigenstates for the ground state and first few axially excited states of the relative motion in the case of a cylindrically-symmetric trap with $\omega_r/\omega_z = 6$. In the limit $a \to 0 \Rightarrow 1/|a| \to \infty$, the eigenstates are of non-interacting atoms in a harmonic oscillator, and the motional level n_{rel} is a good quantum number. In Figure 6.2(a) the motional states with odd n_{rel} are drawn, but they are not influenced by the interaction because their wavefunction vanishes at the origin. However, the even-order motional states are mixed by the interaction when the scattering length diverges and $1/a \to 0$. Crossing over a pole in the scattering length either changes the motional level by 2 quanta (since the pseudopotential conserves parity), or transfers atoms between the relative motional ground state and a bound molecular state. Crucially, only atoms in the relative motional ground state can be associated into a molecular bound state. Here $n_{\mathrm{rel}} = 0$ refers to the relative motional ground state along all trap axes:

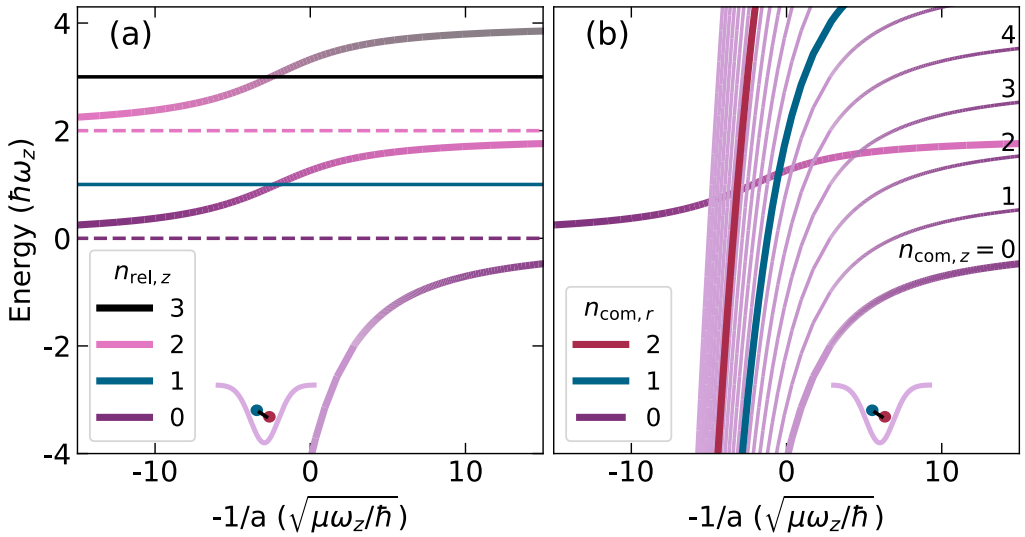

Figure 6.2: Energy eigenstates of an atom pair in a cylindrically-symmetric harmonic potential with $\omega_r/\omega_z = 6$. (a) An interacting atom pair in the relative motional ground state $n_{\mathrm{rel}} = 0$ can associate into a bound state by crossing the pole in the scattering length at $1/a = 0$. An excited atom pair with $n_{\mathrm{rel}} > 0$ will not associate into a bound state. (b) When the motion is separable, the eigenstates with excited centre-of-mass motion are replicas of the relative motion displaced in energy. Eigenstates with $n_{\mathrm{com}} > 0$ still associate into a bound state provided that $n_{\mathrm{rel}} = 0$. In both plots, the energy is shown relative to the harmonic oscillator ground state energy.

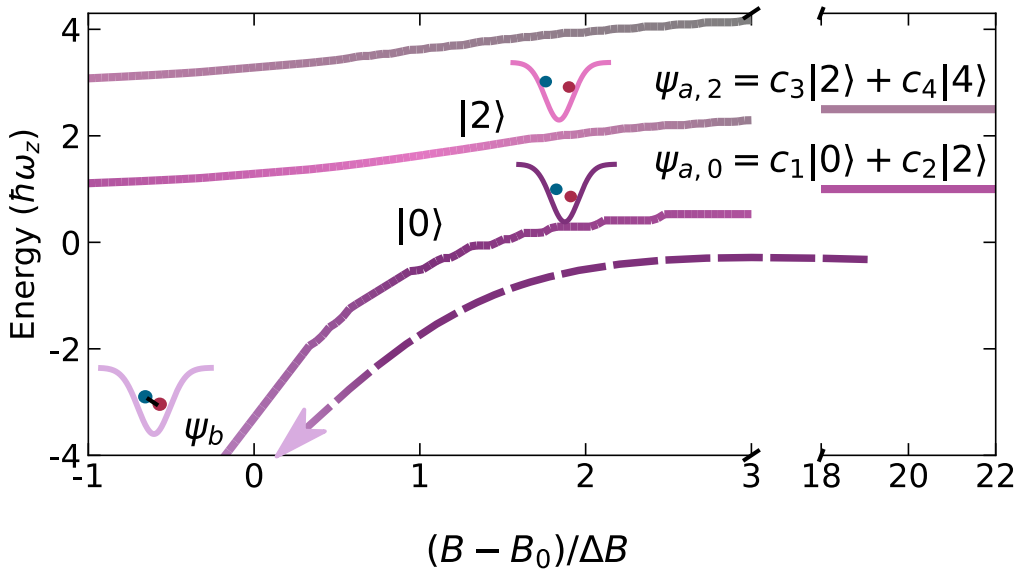

Figure 6.3: Energy eigenstates for an interacting atom pair near to a Feshbach resonance. The interspecies background scattering length for RbCs is large enough that the interaction mixes motional states away from the Feshbach resonance. The relative motional ground state, $\psi_{a,0}$, becomes the ground harmonic oscillator state $n_{\mathrm{rel}} = 0$ in the limit of vanishing scattering length. A magnetic field ramp following the dashed arrow associates into the molecular bound state if the atom pair start in $\psi_{a,0}$. The energies shown are relative to the harmonic oscillator ground state energy.

$|n_{\mathrm{rel},x} = 0, n_{\mathrm{rel},y} = 0, n_{\mathrm{rel},z} = 0\rangle$. Since the COM and relative motion are separable, the eigenstates with excited COM motion are copies of the relative motion eigenstates displaced by $n_{\mathrm{com},z}\hbar\omega_z + n_{\mathrm{com},y}\hbar\omega_y + n_{\mathrm{com},x}\hbar\omega_x$, as illustrated in Figure 6.2(b) for $n_{\mathrm{rel}} = 0$. The $|n_{\mathrm{rel}} = 0, n_{\mathrm{com}} \geq 0\rangle$ states can associate into the bound state, in which case the molecule inherits its motional state from the atom pair.

6.2.2 Energy-dependent Scattering Length

Although the pseudopotential is sufficiently accurate for typical background scattering lengths, an energy-dependent scattering length is required when the interaction strength diverges near a Feshbach resonance [269, 283, 298,

300], which can be approximated by:

$$a(E) = a_{\rm bg}\left(1 - \frac{\Delta B(1+\frac{E}{E_b})}{B - (B_0 + \frac{E}{\mu_m} - \Delta B\frac{E}{E_b})}\right), \tag{6.8}$$

where $E_b = \hbar^2/(\mu a_{\rm bg}^2)$ is the binding energy associated with the background scattering length, and μ_m is the difference between the magnetic moments of the open and closed channels. A more accurate calculation of the energy-dependent scattering length can be derived from a two-channel model [301], but Equation 6.8 is sufficiently accurate for qualitative conclusions.

Figure 6.3 displays the results of solving Equation 6.5 using the energy-dependent scattering length in Equation 6.8. Away from the Feshbach resonance, the background scattering length of $670\,a_0$ is sufficiently large that the interactions mix even-order motional states and $n_{\rm rel}$ is not a good label for the quantum state. Therefore, we label the relative motional ground state as $\psi_{a,0}$, which becomes $|n_{\rm rel} = 0\rangle$ in the limit of vanishing scattering length: $a \to 0$. For the motional ground state, the scattering length vanishes at $B = B_0 + \Delta B$, but the energy-dependence shifts the zero-crossing for the excited states. Starting at a magnetic field above the Feshbach resonance and sweeping down across the resonance associates the atoms into the molecular bound state, $\psi_{a,0} \to \psi_b$. Alternatively, starting below the Feshbach resonance and sweeping the field up across the resonance excites the relative motion by 2 quanta. We label the motionally excited state $\psi_{a,2}$ as it becomes $|n_{\rm rel} = 2\rangle$ in the limit of vanishing scattering length.

6.2.3 Trap-induced Resonances

In several circumstances the effect of the confining potential is to significantly modify the effective scattering length between the two trapped atoms. The first proposal for elastic confinement-induced resonances (CIRs) came from studying a quasi-1D harmonic trap [302]. Since then, there has been interest in studying inelastic CIRs [303] and trap-induced shape resonances (TISRs) [304] which both involve coupling between a molecular bound state and atom-pair harmonic oscillator states. The coupling between an atomic open channel and molecular closed channels is analogous to a Feshbach resonance [305]. In fact, a likely place for a CIR to occur is near a magnetic

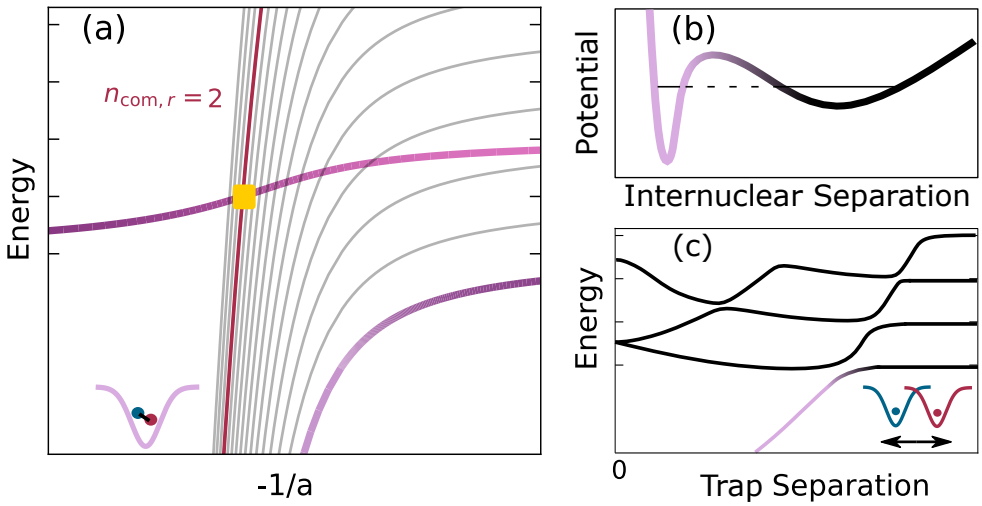

Figure 6.4: Avoided crossings in the energy spectrum of a confined interacting atom pair. (a) Coupling between centre-of-mass and relative motion creates inelastic CIRs between an atomic unbound state and bound states with excited centre-of-mass motion. The yellow square marks the position of one of the strongest couplings between the unbound relative motional ground state and a bound state with $n_{\mathrm{com},r} = 2$. (b) For atoms confined in separate harmonic potentials, a TISR occurs when an internal molecular bound state becomes degenerate with a harmonic oscillator state of the atom pair. (c) Shape resonances cause avoided crossings between harmonic oscillator states and a molecular bound state. Inset: illustration of two atoms in separate potentials.

Feshbach resonance where the scattering length is sensitive to the magnetic field. In studying this situation, the theory must be able to explain experiments where multiple resonances were observed as a function of trap anisotropy [306, 307].

One way to expand the theory is to include the effects of anharmonicity in the trapping potential [303, 308–310]. Anharmonic terms in the two-body Hamiltonian couple the COM and relative motion, creating avoided crossings between motional states that might have axial or transverse excitations. An anharmonic CIR occurs when a molecular bound state with excited COM motion crosses the relative motional ground state [310], as illustrated in Figure 6.4(a). These resonances have also been called inelastic CIRs to reflect the exchange of molecular binding energy with kinetic energy [303]. Selection rules dictate which states can couple; the parity of the wavefunction is conserved when the anharmonicity is from a quartic term. Then for a cigar-shaped trap with $\omega_r \gg \omega_z$, the most significant coupling is when the unbound $|n_{\mathrm{rel}} = 0, n_{\mathrm{com}} = 0\rangle$ state couples to the molecular bound state with radial COM excitation $n_{\mathrm{com,r}} = 2$ [303]. Note that the additional resonance splits in two when there is anisotropy $\omega_x \neq \omega_y$. As well as quartic terms, the anharmonic potential might have a cubic term which enables a coupling to states with odd n_{rel}, although the coupling strength is expected to be weaker [310]. It is possible then to observe more than two resonant features as several states with excited COM motion (odd or even excitations) become degenerate with the relative motional ground state at different scattering lengths. Anharmonic CIRs have been used to explain loss measurements [303, 310] and coherent molecule formation [311].

Coupling between COM and relative motion also occurs for atomic species with different trap frequencies, $\omega_{i,\mathrm{Rb}} \neq \omega_{i,\mathrm{Cs}}$. The coupling term is $C_i d_i R_i$ where for the trap axis $i \in \{x, y, z\}$, $C_i = \mu(\omega_{i,\mathrm{Cs}}^2 - \omega_{i,\mathrm{Rb}}^2)$ is the coupling coefficient, d_i is the COM position, and R_i is the relative separation [268, 312]. The motional coupling might be expected to produce an inelastic CIR when bound states with excited COM motion become degenerate with the relative motional ground state [308]. However, the different symmetry of the bound and unbound states prevents coupling between these states [313]. To reach the molecular state would require the introduction of an additional

coupling such as those produced by magnetic field modulation or an RF pulse [56, 312]. In our case, the trapping frequencies for Rb and Cs in the 1064 nm tweezer satisfy $\omega_{\mathrm{Cs}} = 1.08\omega_{\mathrm{Rb}}$, such that the motion is approximately separable.

Further complications arise if the atoms are in separate harmonic potentials, for example during the merging stage of the sequence. Theoretical analysis of two atoms in separate harmonic traps predicts the appearance of TISRs [269, 304, 314], as illustrated in Figure 6.4(b). The shape resonance occurs when there is a potential barrier between a molecular internal bound state and a nearly-degenerate atomic harmonic oscillator state. Figure 6.4(c) depicts how adiabatically crossing a shape resonance by decreasing the trap separation could coherently associate atoms into a molecular bound state [270, 315]. On the other hand, separating the traps could transfer from a molecular bound state to an unbound atom-pair state, effectively pulling apart the molecule. Interestingly, the external potential couples motional states with different parity, such that it is possible to transfer an atom pair to a motionally excited state with either even or odd symmetry after traversing a series of avoided crossings [269].

In summary, modelling the harmonic confinement of the interacting atom pair with a pseudopotential describes the relationship between harmonic trap states and molecular bound states. Ramping the magnetic field down across a Feshbach resonance can associate an atom pair from the relative motional ground state into a molecular bound state. Ramping the magnetic field up across a Feshbach resonance should dissociate the least-bound state or excite the relative motion of an atom pair. Complications arise when we consider the anharmonicity of the trap and nonseparability of COM and relative motion: avoided crossings appear in the energy spectrum. The first consequence is the appearance of additional loss features in Feshbach spectroscopy measurements [303]. There could also be a reduction in the molecule-association efficiency if atoms with excited COM motion follow an avoided crossing into a state other than the bound state. Moreover, it is possible that the presence of a TISR causes the atom-pair state to cross into the bound state during the merging of the traps. The reverse also holds; a molecular state might be dissociated into an atom pair during the separation of the traps. Finally,

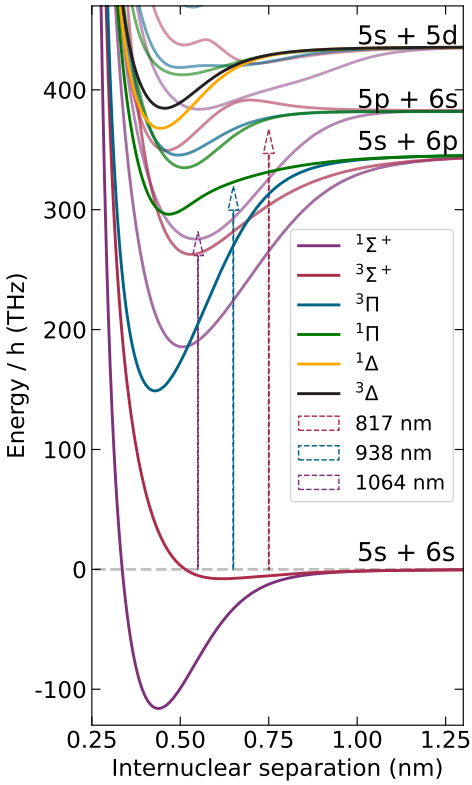

Figure 6.5: Potential energy curves of the RbCs molecule discounting spin-orbit coupling. The arrows indicate the energy of an 817 nm (red), 938 nm (blue), or 1064 nm (purple) photon relative to the dissociation threshold for the Rb 5s + Cs 6s pair state. The scattering rate for photons of these wavelengths depends on the proximity to a vibrational level of one of the molecular potentials.

applying an upwards magnetic field ramp might not dissociate a molecule, but instead retain a confinement-induced bound state [269, 316].

6.3 Trap-induced Stark Shifts

The tweezer laser induces a dipole moment in the trapped particle, causing an ac Stark shift of energy levels. Generally, the dynamic polarisability of a near-threshold bound state can be approximated by summing the polarisabilities of the individual atoms. However, the bound state's polarisability diverges when the tweezer laser frequency approaches a molecular transition. In this case, typical tweezer intensities produce a significant ac Stark shift of the molecular energy levels. This in turn shifts the magnetic field at which a Feshbach resonance is observed.

In this work we use pair loss caused by photoexcitation to detect the presence of a Feshbach resonance. Photoassociation is a method of producing molecules [317], and photoassociative loss can be used as an alternative

method to detect Feshbach resonances when incident light is tuned near to a photoassociation line [318–320]. Feshbach resonance-enhanced pair loss from scattering trap photons has been observed in optical tweezers even when the light is $> 20\,\mathrm{GHz}$ detuned from any photoassociation lines [223]. The loss is better described as photoexcitation from the weakly-bound molecular state which is coupled to the atomic unbound state by the Feshbach resonance [284]. It is easy to verify that the photoassociation rate is negligible away from the Feshbach resonance, but to distinguish between photoexcitation and photoassociative loss requires investigation into the dependence on the laser frequency.

To help understand which molecular states the laser light might couple to, we plot molecular potential energy curves ignoring spin-orbit coupling in Fig 6.5. The photon energies for the wavelengths of the optical tweezers used in this thesis could excite to an electronically excited state. While there is a comparatively high density of photoassociation lines near the tweezer wavelengths, the spacing between vibrational levels is expected to be $\sim 1\,\mathrm{THz}$, which is much larger than the expected transition linewidth of $\sim 10\,\mathrm{MHz}$. The laser frequency would need to be within approximately a linewidth in order for the photoassociation rate to be significant, whereas the photoexcitation rate can be significant even when the frequency is 100's of GHz detuned from resonance. To predict the frequency of relevant transitions requires calculations of transition dipole moments (TDMs) using knowledge of the molecular potentials [321]. Calculations from Olivier Dulieu's group suggest that the closest transition to 1064 nm with a significant TDM is from $a^3\Sigma^+ \rightarrow c^3\Sigma^+$, where the $a^3\Sigma^+(v = -6)$ vibrational level has the strongest dipole moment. However, we can distinguish between photoassociative and photoexcitation without knowledge of the particular excited molecular state. Photoassociative loss from the bare atomic state would imply a linear relationship between the laser frequency and the magnetic field at which the loss feature is observed.

We model the Stark-shifted Feshbach resonance and photoexcitation using a three-level system [284]. The model involves an atomic scattering state at the dissociation threshold $|a\rangle$, a near-threshold bound state $|g\rangle$, and an electronically-excited molecular state $|e\rangle$. Firstly, the scattering state $|a\rangle$

couples to the weakly-bound state $|g\rangle$ at the Feshbach resonance. In turn, the weakly-bound state $|g\rangle$ is strongly coupled to the excited state $|e\rangle$ by the tweezer light. The decay from the excited molecular state populates states which are not detected and is observed as loss with a rate γ_e. Since the rate of photoexcitation and subsequent decay is much faster than the transfer into the weakly-bound state, both molecular states can be adiabatically eliminated. It is then possible to obtain a complex-valued scattering length, where we make the simplifying assumption that the photoassociation rate from $|a\rangle$ to $|e\rangle$ is negligible [284, 322]:

$$\frac{a}{a_{\mathrm{bg}}} = 1 + \frac{\mu_{ag}\Delta B}{\hbar}\left(\frac{\Delta_e - i\gamma_e/2}{|\Omega/2|^2 - \Delta_g(\Delta_e - i\gamma_e/2)}\right). \tag{6.9}$$

Here, μ_{aj} is the differential magnetic moment between $|a\rangle$ and $|j\rangle = \{|g\rangle, |e\rangle\}$ which leads to an energy shift of $\Delta_g = \mu_{ag}(B - B_0)/\hbar$ for state $|g\rangle$ and $\Delta_e = -\Delta_{\mathrm{L}} + \mu_{ae}(B - B_0)/\hbar$ for state $|e\rangle$. Δ_{L} is the detuning of the laser from the $|g\rangle \leftrightarrow |e\rangle$ transition, and the Rabi frequency $\Omega = \langle e|\hat{d}|g\rangle\sqrt{I/(c\epsilon_0)}/\hbar$ is determined by the TDM $\langle e|\hat{d}|g\rangle$ and the laser intensity I. In the limit of large detuning $\Delta_{\mathrm{L}} \gg \Omega$, the scattering length diverges at a magnetic field of

$$B - B_0 = -\frac{\hbar\Omega^2}{4\mu_{ag}\Delta_{\mathrm{L}}}. \tag{6.10}$$

The imaginary part of the scattering length is related to the two-body photoexcitation rate [286, 323]:

$$\dot{N}_{2\to 0} = n_2 k_2 = \frac{4\pi\hbar n_2 \mathrm{Im}(a)}{\mu(1 + k^2|a|^2 + 2k\mathrm{Im}(a))}, \tag{6.11}$$

where n_2 is the pair density and μ is the reduced mass.

6.4 Measuring Two-body Loss

We experimentally detect the presence of a Feshbach resonance by preparing a pair of atoms in the motional ground state of separate tweezers, then merging and holding the atoms together in a common tweezer at a set magnetic field. In order to maintain a constant scattering length during the merging stage, we turn on the magnetic field at a value far from any Feshbach resonance (typically 210 G) while the atoms are held in separate traps. The

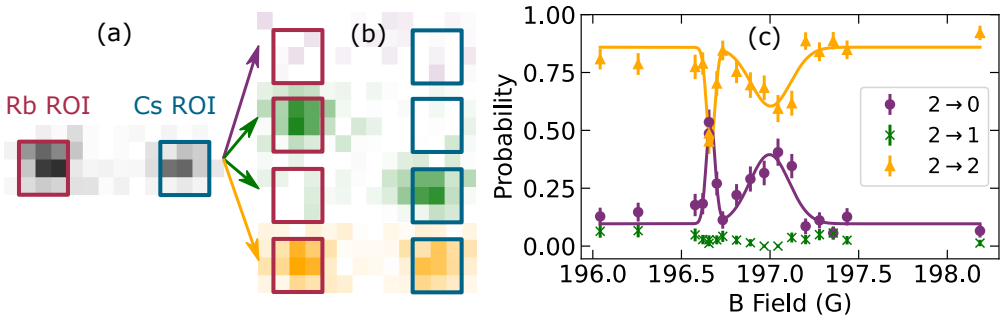

Figure 6.6: Analysis of collisions between a Rb atom and a Cs atom. (a) Sequence runs are post-selected on the condition of initially imaging two atoms. (b) A final image at the end of the sequence measures the number of atoms remaining. (c) two-body loss occurs when holding the atoms at magnetic fields near a stark-shifted Feshbach resonance. In some cases, an additional loss feature is observed, presumably due to an avoided crossing with a bound state that has excited COM motion.

tweezer trap depths are reduced to $\sim 0.1\,\mathrm{mK}$ to mitigate scattering during the 10 ms it takes for the magnetic field to turn on. Once the field has settled to within 0.2 G, the atoms are transferred into a common tweezer. Then the magnetic field is suddenly changed to a value near the expected position of the Stark-shifted Feshbach resonance (although the inductance of the coils means that it can take $\sim 1\,\mathrm{ms}$ for the field to settle to within 0.2 G). The atoms are held together for a sufficient duration to observe loss, which is typically between $10 - 50\,\mathrm{ms}$. Then the magnetic field is suddenly changed to a value far from the Feshbach resonance before the unmerging stage separates any surviving atoms into separate traps for imaging. There are a few practicalities to consider when analysing the data from these experiments.

In our experiments, the presence of the Feshbach resonance is signified by not re-imaging atoms in a final image, as displayed in Figure 6.6. For the purpose of these experiments, we assume that our high-fidelity imaging allows us to ignore detection errors; if an atom is in the trap, it is detected in the image. In post-processing we select only the experimental runs where both a Rb and a Cs atom were detected in the first image, as in Figure 6.6(a). Figure 6.6(b) shows the possible outcomes in the final image at the end of the sequence. We choose the probability of re-imaging zero atoms, $P_{2\to 0}$, as the dependent

variable since it is the most robust against experimental imperfections. In the Feshbach resonance experiments, the most likely reasons for not re-imaging an atom are because it has escaped the trap, or because it has been associated into an undetectable molecular state (which might also escape from the trap). These two outcomes are incorporated into our three-level model as two-body loss and observed as an increase in $P_{2\to 0}$. The issue with $P_{2\to 2}$ is that it decreases when there is any loss, including single-atom loss. The distinction is of no consequence when single-atom loss is negligible, as illustrated in Figure 6.6(c). However, the choice of dependent variable is important in experiments aiming to optimise the association efficiency, as we will come to in Section 6.5.3.

In several of the two-body loss measurements we observe multiple loss features. Figure 6.6(c) displays two-body loss after holding the atom pair for a duration of 150 ms in a tweezer with a frequency of 281.364 THz and an intensity of 20 kW cm^{-2}. Two loss features are observed at magnetic fields of 197.00(3) G (close to the expected value of a magnetic Feshbach resonance at 197.1 G [162, 163, 324]) and 196.665(6) G. The most likely explanation for the additional loss feature at a lower field is that the atom pair state couples to a bound state with excited COM motion; an inelastic CIR [303, 313]. Allocating the CIR to a particular motional state requires an accurate calculation of the energy eigenstates and energy-dependent scattering length. Using Equation 6.5 and Equation 6.8 we predict that an avoided crossing with the $n_{\mathrm{COM},r} = 2$ bound state should occur at a magnetic field of 196.84 G, which is not in agreement with the experimental measurement. The discrepancy is likely due to the inaccuracy of the energy-dependent scattering length formula, but a more accurate calculation is beyond the scope of this work. Nevertheless, the additional loss feature is evidence that inelastic CIRs influence our system.

6.4.1 Measurements of Feshbach Resonances

Measurements of the Stark-shifted Feshbach resonance are presented in Fig 6.7 where the tweezer intensity, tweezer frequency, and magnetic field are independent variables. The experiment follows the previously-described

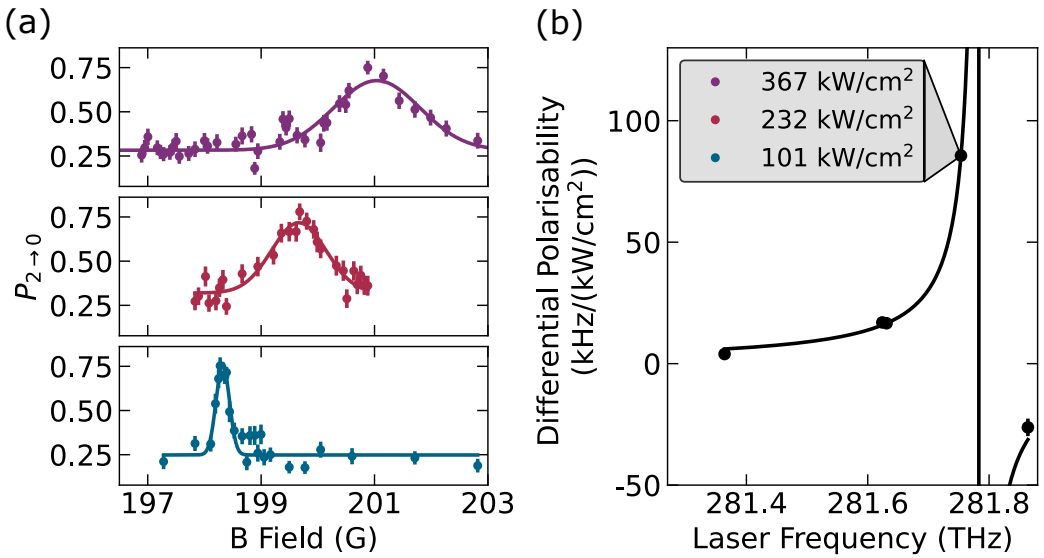

Figure 6.7: The Stark shift of the Feshbach resonance near 197 G is dependent on the intensity and frequency of the tweezer laser. (a) Loss features are observed as the magnetic field is tuned with a fixed laser frequency of 281.75 THz and a fixed intensity as labelled in the legend in (b). We extract the energy difference between the free atom and bound states. (b) The change in differential dynamic polarisability as a function of laser frequency is used to fit a resonance with a molecular transition at a frequency of 281.783(17) THz (black vertical line) with a transition dipole moment of $0.064(2)\,ea_0$.

sequence where the atom pair is held in a common tweezer at a constant magnetic field. For a given tweezer laser frequency and intensity, the Stark-shifted resonance position is extracted from a Gaussian fit. The resonance position increases linearly with intensity, as is determined from the data in Fig 6.7(a) by comparing the centre of the loss feature when the laser frequency is 281.75 THz and the intensity is 101 kW cm^{-2}, 232 kW cm^{-2}, and 367 kW cm^{-2} for the blue, red, and purple plots respectively. The observed shift is a manifestation of a change in the energy separation between the initial atom-pair state and the molecular bound state responsible for the Feshbach resonance. The gradient of the resonance position as a function of intensity gives us the difference between the dynamic polarisabilities of the atom-pair state and the bound state: $\Delta\alpha = d(B/2\mu_{ag})/dI = |\langle e|\hat{d}|g\rangle|^2/(2c\epsilon_0\Delta_L)$. The differential polarisability is plotted against laser frequency in Figure 6.7(b); the pole at a frequency of 281.783(17) THz indicates resonance with a transition between molecular states. We fit a TDM of 0.064(2) ea_0, assuming that the frequency is sufficiently far detuned from other transitions between molecular states so that their influence is negligible. The fitted dipole moment is the same order of magnitude as predicted for the transition between the $a^3\Sigma^+(v = -6) \leftrightarrow c^3\Sigma^+$ molecular states. A more precise estimation would require calculation of Clebsch-Gordan coefficients between rotational and hyperfine states. Nevertheless, the three-level model accurately predicts the Stark shift of the Feshbach resonance, justifying our description of photoexcitation instead of photoassociative loss.

Previous measurements of this Feshbach resonance in bulk gas experiments have reported the position of the pole to be 196.8 G [324], 197.06(5) G [162], or 197.10(3) G [163]. By extrapolating the Stark-shifted Feshbach resonance experiments to where the laser intensity is zero, our measurements predict that the unshifted Feshbach resonance appears at a magnetic field of 197.15(3) G.

It is desirable to set the tweezer laser frequency away from resonance with the molecular transition. The main reason is to avoid two-body loss, as the imaginary component of the scattering length increases near the resonant frequency. Therefore, we perform association experiments using a tweezer laser frequency of < 281.65 THz and intensity < 50 kW cm^{-2}. The following association experiments were taken before the full characterisation of the ac

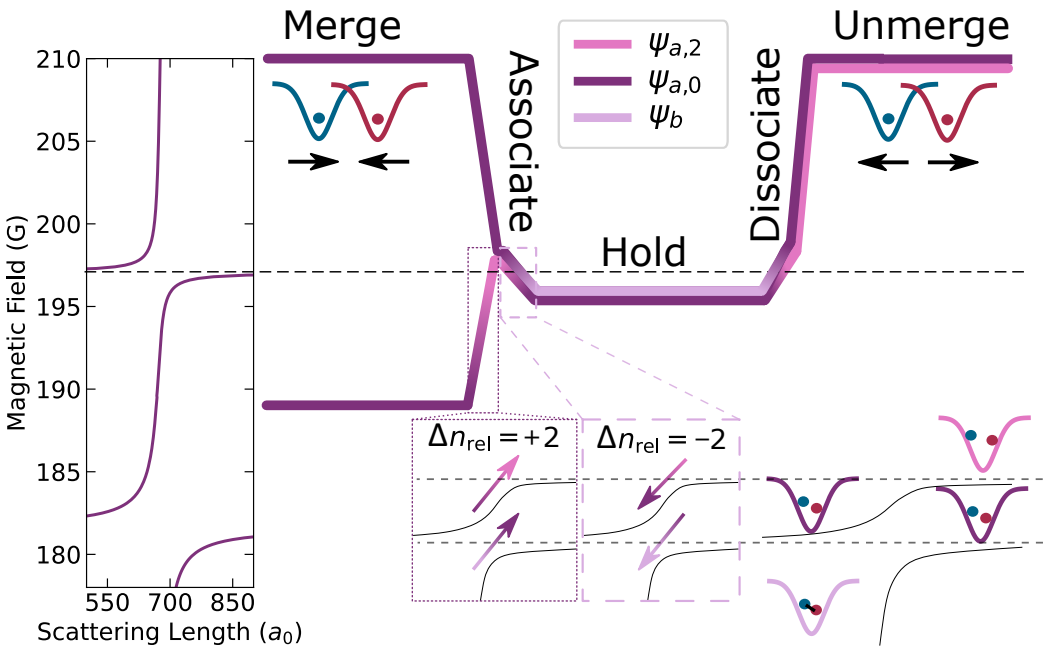

Figure 6.8: The magnetic field ramps used in association experiments. Similar sequences prepare an atom pair in the relative motional ground state or an excited state by merging tweezers at a magnetic field of 210 G or 189 G respectively, and then ramping to 199 G. An "associate" ramp from 199 G to 196.7 G then reduces the relative motional level or associates into a molecular state. The particles are held for some duration before performing a reverse ramp to dissociate molecules, then separating the traps to image the atoms. For reference, the left-hand plot shows the divergence of the interspecies scattering length at two Feshbach resonances located at magnetic fields of 197.1 G and 181.6 G.

Stark shifts was completed, and used a tweezer laser with a frequency of 281.624 THz, which is still sufficiently far detuned from resonance to ignore the effects of Stark shifts given the moderate intensity of 37 kW cm^{-2}.

6.5 Association Sequence

Figure 6.8 illustrates the sequence used to associate an atom pair. Similar to the previous experiments, the magnetic field is held far away from the Feshbach resonance while merging the atoms. The difference is that instead of suddenly changing the magnetic field once the atoms are in a common

tweezer, we now perform a field ramp over the Feshbach resonance in order to adiabatically follow the avoided crossing and change state. Ramping the field down across the Feshbach resonance reduces the relative motional level by two quanta, $\psi_{a,2} \rightarrow \psi_{a,0}$, or enters a bound state from the relative motional ground state, $\psi_{a,0} \rightarrow \psi_b$, or transfers the least-bound state into a different bound state. After a hold time, reversing the field ramp reverts the change of state, and surviving atoms are separated into their respective tweezers to be re-imaged. In order to detect the presence of a molecule, we extend the hold time so that molecules with a sufficient photoexcitation rate are lost and $P_{2\rightarrow 0}$ increases. The hold duration is significantly shorter than the lifetime of an atom pair held in the trap, such that an atom pair is not lost. Although it is not guaranteed, we expect that the lifetime of a molecular state is significantly shorter than that of the atom pair, since there is increased coupling to the excited molecular state. Therefore, the observation of two-body loss is indicative of transfer to a molecular state.

As a further demonstration of coherently manipulating the quantum state, we compare the sequence that associates molecules to one which first ramps the field up across the Feshbach resonance. Figure 6.8 illustrates a second sequence where the magnetic field is held at 189 G during the merge and then swept up across the Feshbach resonance to 199 G. Atoms initially in the relative motional ground state would then be transferred to an excited state. The rest of the sequence follows the same as the association sequence. When the magnetic field is swept back down across the Feshbach resonance, the initial state is restored, for which the loss rate is low.

6.5.1 Association Pathways

Before analysing the results of association experiments, we must consider the implications of having several possible association pathways. As previously discussed, there are two possible methods of associating a molecule: crossing a TISR during the trap merge, or crossing the Feshbach resonance with a magnetic field ramp. The association sequence permits either association pathway.

There are a few ways that we can distinguish between the association path-

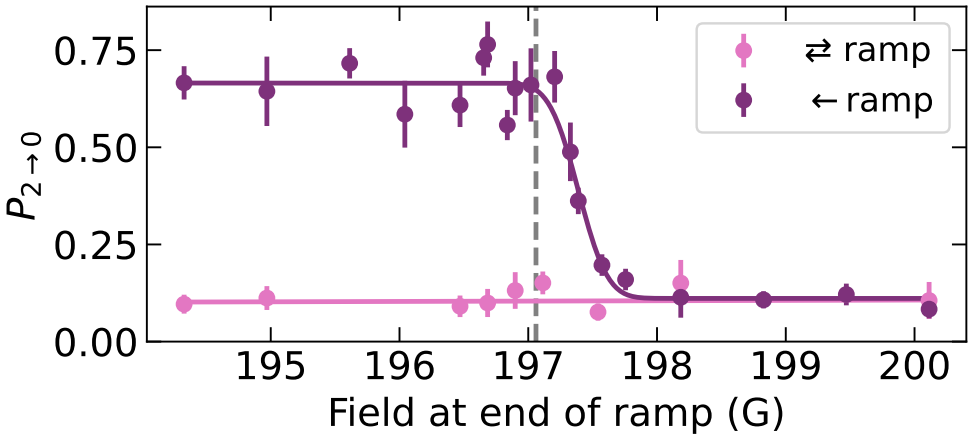

Figure 6.9: Association using a sequence with a magnetic field ramp. The 15 ms hold duration is much shorter than the lifetime of the initial state. If the field is ramped down across the Feshbach resonance, there is transfer into a state that is lost. However, if the downwards ramp is preceded by an upwards ramp from 189 G to 199 G, then crossing the resonance with the second ramp restores the initial state. The dashed line marks the position of the Feshbach resonance at 197.1 G.

ways. While magnetoassociation associates atom pairs with excited COM motion, this is unlikely to be the case for association by merging due to avoided crossings between motional states. Another distinction is in the state of the molecule: if the atoms are associated into a bound state while merging the traps, then a subsequent magnetic field ramp over the Feshbach resonance would transfer into a different bound state. Alternatively, if during the separation of the traps the bound state follows an avoided crossing caused by a TISR, then we would detect atoms when we had expected an undetectable molecule. These differences are not always evident in the results of an experiment. Therefore, our discussion of experiments will remain agnostic to the association pathway until there is evidence to distinguish between them.

6.5.2 Association Measurements

The two different sequences illustrated in Figure 6.8 are used to search for a signal of association. Figure 6.9 displays the results of varying the magnetic field at the end of the "associate" ramp. The magnetic field is swept linearly with a variable endpoint but a fixed duration of 3 ms. No additional loss is observed when this downwards ramp is preceded by an upwards ramp. However, without the initial upwards ramp, the downwards ramp transfers the initial state into a molecular state when the endpoint is below the Feshbach resonance. A hold duration of 15 ms is long enough to observe loss. Despite using a relatively low intensity of 37 kW cm^{-2}, the onset of loss in Figure 6.9 begins at a field of 197.3 G, 0.2 G above the expected position of the Feshbach resonance. The most likely explanation is that the photoexcitation rate is significant even for this reduced tweezer intensity. To prove that the loss below 196.9 G is due to the creation and subsequent loss of a molecule, we reduce the hold duration to 1 ms at an end-of-ramp field of 196.7 G and recover $P_{2\to0} = 0.19(9)$ as the molecule is successfully dissociated back into atoms. We measure a 1/e loss timescale of 4.5(6) ms by varying the hold duration, which implies that holding the molecule for 15 ms gives a loss probability of $1 - \exp(-15/4.5) = 0.96$. Using the contrast of the fit in Figure 6.9, we estimate that 57(3) % of runs convert the loaded Rb and Cs atoms into a molecule, after correcting for the finite loss probability.

The onset of loss after ramping the magnetic field below the Feshbach resonance could occur through either association pathway. In the absence of association during merging, the loss is a result of magnetoassociation into a weakly-bound state with a photoexcitation rate significantly faster than that of the atom pair. However, it is also possible that the atoms are associated during the merge, but the weakly-bound state has a photoexcitation rate similar to that of the atom pair. Since the association by trap merging is reversible, we only observe loss when transferring to a more deeply bound state (with a greater photoexcitation rate) after ramping the magnetic field across the Feshbach resonance. Additional evidence corroborates the latter theory: we measured $P_{2\to0}$ consistent with no change in the mean when repeating the association experiment with faster magnetic field ramp speeds. Yet, a faster

ramp speed would reduce the magnetoassociation efficiency according to the Landau-Zener formula in Equation 6.3. Therefore, the insensitivity of the association efficiency to the field ramp speed is evidence for association by merging. Other parameters are expected to have a significant effect on the probability of creating a molecule with the association sequence, particularly parameters which affect the motional ground state probability.

6.5.3 Optimising Association

Before discussing the results of optimisation experiments, we note the need for careful interpretation. We are only interested in $P_{2\to 0}$ increasing as a result of a greater molecule conversion efficiency. While $P_{2\to 0}$ is not sensitive to single-atom loss, there are other causes of two-body loss, such as heating the atoms out of the trap. Therefore, after optimisation we verify (by reducing the hold time) that the molecule can be associated and also subsequently dissociated.

We also note that there are likely different optimal parameters for magnetoassociation or association by merging. If the atoms are magnetoassociated, then the merging parameters will affect only the relative motional ground state probability. However, if the association occurs during the merge, then the merging parameters will likely affect the Landau-Zener probability of adiabatically transferring to the bound state. At this stage, we reserve judgement on which association pathway dominates and optimise the conversion efficiency regardless. Subsequent measurements will better distinguish between the association pathways.

In Figure 6.10 we optimise the parameters of the association sequence using the conversion efficiency as an objective function. The conversion efficiency is determined by three factors: the probability of occupying the relative motional ground state, the probability of occupying the desired spin state, and the Landau-Zener probability of adiabatically transferring to the bound state. In our case, the limiting factor is the motional ground state probability. We have already described in detail the process of cooling the individual atoms to the motional ground state of separate traps and transferring to a common tweezer with minimal motional excitation. The benefit of using

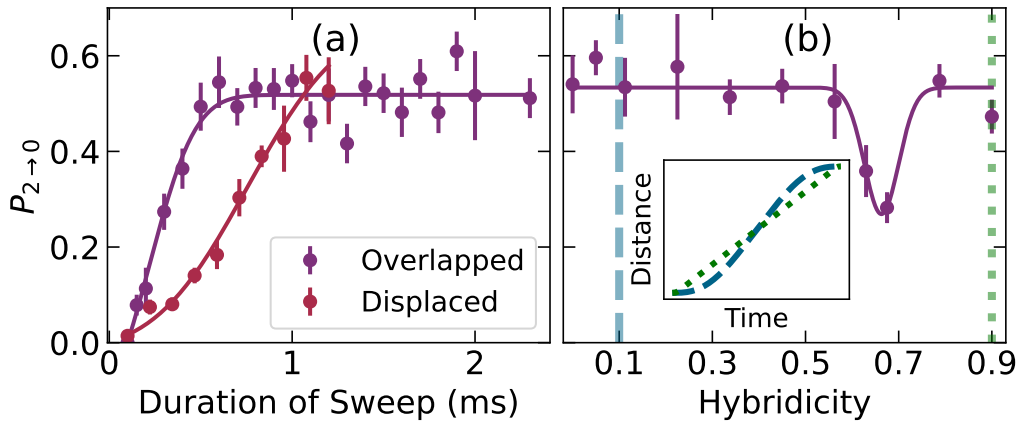

Figure 6.10: Using an association sequence to find optimal merging parameters. $P_{2\to 0}$ is proportional to the motional ground state fraction. (a) Varying the sweep duration for a trajectory with a hybridicity of 0.1. Durations of $> 0.6\,\mathrm{ms}$ are sufficient to maintain the motional ground state provided that the traps are well overlapped. When the end position of the sweep is displaced by $0.41(3)\,\mu\mathrm{m}$, a longer sweep duration is required. (b) Varying the hybridicity for a sweep duration of 1 ms. At a hybridicity of 0.66(8) the ground state fraction is reduced by heating from resonant intensity modulation. The inset displays trajectories with a hybridicity of 0.1 (blue dashed line) and 0.9 (green dotted line).

the conversion efficiency as an objective function is that it is proportional to the relative motional ground state fraction and therefore requires fewer measurements than using sideband spectroscopy.

In Figure 6.10(a) we optimise the duration of the sweep that overlaps the tweezers, using a hybridicity of 0.1. In Chapter 5 we discussed finding a compromise between merging slow enough to avoid motional excitation while avoiding excess time for photon scattering. Here, we see that a sweep duration $> 0.6\,\mathrm{ms}$ permits transport without excitation provided that the trajectory ends at (or just before) the centre of the other potential.

Figure 6.10(a) also displays the same experiment performed with a displaced trajectory. The 938 nm tweezer's displaced trajectory ends at a distance $0.41(3)\,\mu$m beyond the centre of the 817 nm tweezer potential. The centre of the 817 nm potential is located in a measurement where Cs atoms are ejected from a 938 nm trap using the repulsive 817 nm potential. For the displaced trajectory it is still possible to achieve maximal conversion efficiency, but a sweep duration of $> 1\,\mathrm{ms}$ is required.

We find that the reduction in conversion efficiency caused by displacing the traps in the direction of the sweep is not symmetrical. $P_{2\to 0}$ is lower when the trajectory extends beyond the centre of the 817 nm potential compared to stopping short of the centre. In practice this means that experiments optimising the end point of the trajectory determine an optimal position which is different from the overlap position measured by ejecting Cs atoms. Therefore, it is sensible to use the ejection method as an initial estimate for the optimal endpoint of the trajectory, then fine-tune the position by measuring its effect on the conversion efficiency. In our setup it is sufficient to correct for drifts in the tweezer pointing by optimising the trajectory endpoint once per week.

Figure 6.10(b) displays heating caused by resonant intensity modulation during the sweep. A sweep duration of 1 ms was used for this measurement. At a hybridicity of 0.66(8) heating from resonant intensity modulation significantly reduces the motional ground state fraction. Nevertheless, the experimental results suggest that a range of trajectories with hybridicity in the range 0.0-0.6 all transport the atom with minimal motional excitation.

Rearrangement fidelity (See Section 3.1.1)	
P(Rb & Cs)	0.75(4)
Motional state preparation (See Section 5.3.2)	
$P(n_{\mathrm{rel}} = 0, n_{\mathrm{com}} = 0)$	0.65(6)
$P(n_{\mathrm{rel}} = 0)$	0.81(8)
Spin state preparation (incl. relaxation during merge)	
Rb $P(f_{\mathrm{Rb}} = 1, m_{f,\mathrm{Rb}} = 1)$	0.95(3)
Cs $P(f_{\mathrm{Cs}} = 3, m_{f,\mathrm{Cs}} = 3)$	0.92(2)
Adiabaticity of magnetic field ramp $1 - P_{\mathrm{LZ}}$	0.988(5)
Conversion efficiency	
$P(f_{\mathrm{Rb}} = 1, m_{f,\mathrm{Rb}} = 1; f_{\mathrm{Cs}} = 3, m_{f,\mathrm{Cs}} = 3)\times$	
$P(n_{\mathrm{rel}} = 0)(1 - P_{\mathrm{LZ}})$	0.70(7)
Molecule creation probability	0.52(6)

Table 6.1: Estimation of the probability that a molecule is created during a run of the association sequence.

6.5.4 Conversion Efficiency

We compare the measured conversion efficiency to the expected efficiency given the fidelity of the state preparation. The results in Figure 6.9 used a trajectory with a sweep duration of 1 ms and a hybridicity of 0.1. From the experiment we measure a conversion efficiency of 0.57(3). For comparison, Table 6.1 summarises individual measurements for the preparation fidelity of the hyperfine spin state and the relative motional ground state. The preparation fidelities are combined with the Landau-Zener probability of adiabatically crossing the magnetic Feshbach resonance at 197.1 G in order to estimate the conversion efficiency. Assuming that an atom pair in $|n_{\mathrm{rel}} = 0, n_{\mathrm{com}} \geq 0\rangle$ will associate into a molecule, then $P(n_{\mathrm{rel}} = 0) = 0.81(8)$ and we estimate a conversion efficiency of 0.70(7). The measured efficiency of 0.57(3) is significantly less than predicted. In fact, the measured efficiency is more consistent with the probability of preparing the COM motional ground state, $P(n_{\mathrm{rel}} = 0, n_{\mathrm{com}} = 0) = P(n_{\mathrm{Rb}} = 0) \times P(n_{\mathrm{Cs}} = 0) = 0.65(6)$, in which case the predicted conversion efficiency is 0.56(6).

The comparison of the measured conversion efficiency with the predicted

efficiency provides insight into the coupling between motional states. If the experiment magnetoassociates the atom pairs, then we expect to associate the atom pairs in motional states with $n_{\mathrm{com}} > 0$, but the same is not necessarily true for association by trap merging. During the merging stage, the difference between the trap frequencies of the two atoms means that there is significant coupling between the COM and relative motion. Instead of associating into the bound state, the states with excited COM motion could follow an avoided crossing into a state with excited relative motion. Our experimental results are consistent with the interpretation that only atom pairs in the relative and the COM motional ground state will associate. Admittedly, the Landau-Zener probability of associating during the merge depends on the width of the relevant avoided crossing, which in this case is an unknown quantity. However, the conversion efficiency measured in Figure 6.10(a) is saturated for sweep durations $> 0.6\,\mathrm{ms}$ in the overlapped case, suggesting that the avoided crossing is sufficiently broad and the Landau-Zener probability is near unity. Therefore, a plausible interpretation of the measured conversion efficiency is that the atom pair adiabatically cross into a bound state during the merge only if they are in the relative and COM motional ground state.

Practical steps can be taken to increase the conversion efficiency regardless of the association pathway. Firstly, the initial motional ground state preparation in separate tweezers could be improved by performing RSC in 1064 nm tweezers such that the differential light shift between spin states is reduced. Secondly, the spin state preparation could be improved by reducing the duration of the merging sequence so that there is less time for spin relaxation. Finally, the merging sequence needs to transfer the atoms to a common tweezer with minimal motional excitation. The heating from resonant intensity modulation during the sweep could be removed by using electro-optic deflectors to translate the tweezer positions [179, 180].

6.6 Feshbach Molecule Characterisation

Characterising the loss rate of the molecule informs our choice of an appropriate tweezer frequency and intensity. Our route to assembling rovibrational ground state molecules relies on the weakly-bound molecule surviving for

sufficient time that we can perform STIRAP before the molecule is lost. In practice, this requires a lifetime on the order of tens of milliseconds.

Characterising the loss rate of the molecule also helps distinguish between the association pathways. As previously stated, it is reasonable to assume that the weakly-bound molecule has a stronger coupling to the electronically excited molecular state than the unbound atom pair, resulting in a greater photoexcitation rate. Moreover, the coupling to the excited state will change when transferring the molecule to a different state by ramping the magnetic field over an avoided crossing. While we lack the knowledge of the TDM required to make a quantitative prediction of the loss rate, we can use relative changes in the loss rate as a function of magnetic field to infer where the bound state changes. In the following subsections, we outline theoretical calculations of the wavefunctions of relevant RbCs bound states. The calculations allow us to predict relative changes in molecular loss rates which can be compared to experimental measurements. Since the bound state occupied at a given magnetic field depends on the association pathway, the experimental results are more consistent with association via one pathway rather than the other.

6.6.1 Bound State Wavefunctions

Figure 6.11 displays the radial wavefunctions of several bound states that are relevant to our experiment. Two features are relevant to our analysis of loss rates: the extent of the wavefunction and its composition. Firstly, the TDM depends on the Franck-Condon overlap with the molecular excited state. Since the excited state is likely deeply-bound, its radial wavefunction will be concentrated at short range ($< 40\,a_0$ in Figure 6.11(a)), and the overlap is greater when the initial bound state is similarly short-ranged. This is not true for the radial wavefunction of the least-bound $|-1(1,3)s(1,3)\rangle$ state in Figure 6.11(a)(i), where the amplitude is greatest at separations $> 40a_0$ and therefore we expect a smaller TDM. Secondly, we can consider the composition of the state. If the excited state is in the $c^3\Sigma^+$ potential, then the TDM is largest when the bound state also has majority triplet character. For the $|-1(1,3)s(1,3)\rangle$ state we calculate 86 % triplet character, whereas

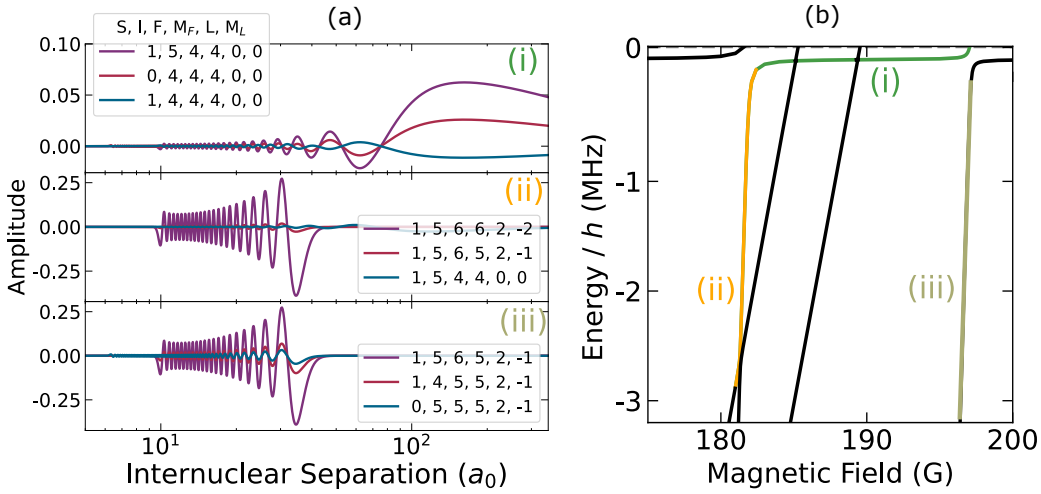

Figure 6.11: We plot the radial wavefunctions of different bound states of RbCs, which were calculated by Jeremy Hutson using the BOUND package [293]. (a) We plot the three channels with the largest contributions to each state, out of a basis of 48 channels satisfying $M_F + M_L = 4$. (i) The least-bound state $|-1(1,3)s(1,3)\rangle$ with a binding energy close to 100 kHz at a field of 193 G. (ii) The state $|-6(2,4)d(2,4)\rangle$ with a binding energy of approximately 2 MHz at a field of 181.5 G. (iii) The state $|-6(2,4)d(2,3)\rangle$ with a binding energy of approximately 2 MHz at a field of 196.7 G. (b) Energies of the states depicted in (a) relative to the atomic dissociation threshold.

for the $|-6(2,4)d(2,4)\rangle$ and $|-6(2,4)d(2,3)\rangle$ states we calculate 99.9 % and 98.7 % triplet character respectively.

Examining the wavefunctions allows us to predict relative changes in the loss rate as a function of magnetic field. The loss rate will change depending on which bound state is occupied at a given magnetic field, which in turn depends on the association pathway.

Magnetoassociating a molecule by crossing the Feshbach resonance at 197.1 G transfers into the least-bound $|-1(1,3)s(1,3)\rangle$ state. The state is dominated by the closed channel after passing several widths from the Feshbach resonance [99, 133, 325], such that transfer into the $|-1(1,3)s(1,3)\rangle$ state is completed when the field reaches < 196.9 G. We expect the loss rate from the least-bound state to be significantly less than that of the $|-6(2,4)d(2,4)\rangle$ state due to a smaller Franck-Condon overlap with the electronically excited state. Therefore, if the magnetic field is ramped below the Feshbach resonance at 181.6 G, we expect the loss rate to increase as we transfer into the more deeply bound $|-6(2,4)d(2,4)\rangle$ state.

On the other hand, association by merging transfers into the least-bound $|-1(1,3)s(1,3)\rangle$ state before the magnetic field ramp. The subsequent magnetic field ramp then transfers the molecule into $|-6(2,4)d(2,3)\rangle$, shown as the black line converting into the gold line at 197 G in Figure 6.11(b). The loss rate from the more deeply bound $|-6(2,4)d(2,3)\rangle$ state is expected to be greater than that of the least-bound state. The $|-6(2,4)d(2,3)\rangle$ state does not have an avoided crossing at 181.6 G, therefore we expect that the loss rate will not increase when the magnetic field is ramped below 181.6 G.

So, we distinguish between the two association pathways by determining whether the loss rate for molecules held at magnetic fields $181.6\,\mathrm{G} < B < 196.9\,\mathrm{G}$ is greater or less than the loss rate for molecules held at fields < 181.6 G.

6.6.2 Measurements of Loss Rates

The loss rate of a molecule is dominated by photoexcitation from tweezer photons. Figure 6.12 displays a collection of measurements of the loss rate

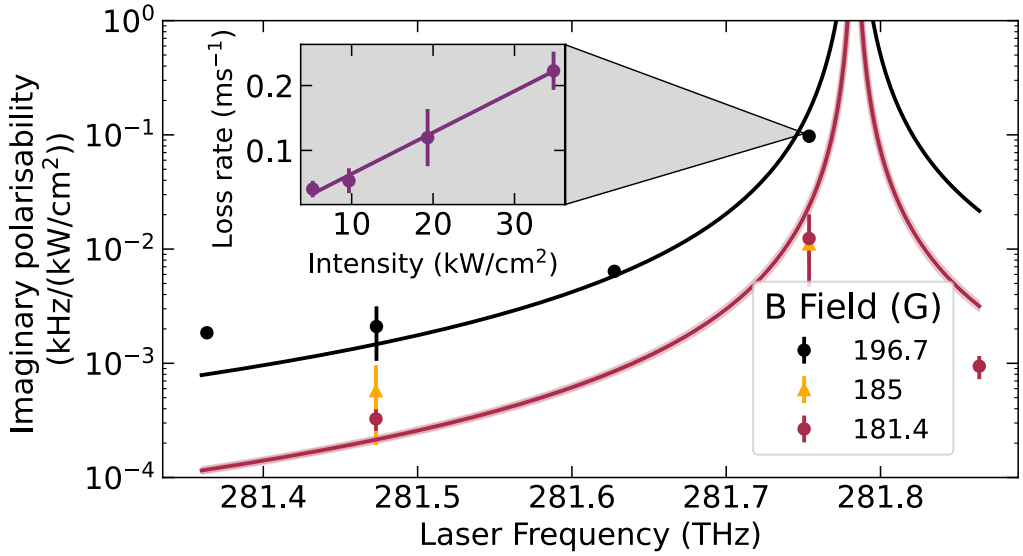

Figure 6.12: The loss rate of a molecule is limited by scattering from the trap. Precursor calculations predict the imaginary polarisability (red line). The calculations match measurements of the loss rate when the magnetic field is ramped to 181.4 G or 185 G after association at 197 G. However, if the field is held at 196.7 G after association, the loss rate is greater and we fit a transition dipole moment of 0.167(17) ea_0 (black line). Inset: Measurements of the loss rate of Feshbach molecules held at 196.7 G when the laser frequency is 281.75 THz. The imaginary polarisability is calculated from the gradient.

of molecules using the association sequence with different magnetic fields during the hold time and different tweezer laser intensities and frequencies. To be clear, the "association" ramp for these experiments is from 199 G down to 196.7 G, and subsequently the magnetic field is ramped in 1 ms to a different value for the duration of the hold. The loss rate can be predicted by estimating the scattering rate of the tweezer as the laser frequency and intensity are varied. In the limit of large detuning $\Delta_{\mathrm{L}} \gg \Omega, \gamma_e$, we can approximate the scattering rate of the tweezer as:

$$\Gamma_{\mathrm{sc}} = \gamma_e \frac{\Omega^2}{4\Delta_{\mathrm{L}}^2}. \tag{6.12}$$

We make the reasonable assumption that the excited molecular state decays at a rate similar to that of the Cs 6p atomic state, $\gamma_e = 2\pi \times 5.2\,\mathrm{MHz}$, as this is the most likely state at the dissociation threshold.

Precursor calculations of the imaginary polarisability $d\Gamma_{\mathrm{sc}}/dI$ (red line in Figure 6.12) give a reasonable fit to the data when the magnetic field is ramped to 181.4 G during the hold time. The calculations use the previously fitted resonant frequency 281.783(17) THz and TDM $0.064(2)\,\mathrm{ea_0}$ from the Stark-shifted Feshbach resonance experiments. In contrast, we measure increased loss rates when holding at a magnetic field of 196.7 G. Using the same previously fitted resonant frequency, we fit Equation 6.12 to the 196.7 G data and extract a TDM of $0.167(17)\,\mathrm{ea_0}$.

The measured loss rates in Figure 6.12 are not consistent with the expectations for a molecule formed by magnetoassociation. Firstly, the loss rates are greater when holding the field at 196.7 G compared to holding at 181.4 G, when we had predicted it to be the other way around. Secondly, the measurements of loss rates holding at a field of 185 G were more consistent with the smaller TDM of $0.064\,\mathrm{ea_0}$ (like the measurements at 181.4 G), returning a chi-squared value of 12.5, compared to a chi-squared value of 1650 using a TDM of $0.167\,\mathrm{ea_0}$ (as fitted to the measurements at 196.7 G). We performed some further investigation using this experiment, which suggested that the TDM changes at a field near to 193 G.

The data are more consistent with the interpretation that the molecules are associated into the least-bound state during the merging stage. In this case, ramping the magnetic field across the Feshbach resonance at 197.1 G would

transfer from $|-1(1,3)s(1,3)\rangle$ to $|-6(2,4)d(2,3)\rangle$, manifested as an increased loss rate at 196.7 G. Then, it is quite feasible that the $|-6(2,4)d(2,3)\rangle$ state crosses with a different state at a field near 193 G. Ramping the field below 193 G would transfer into a state which might have similar characteristics to the least-bound state and therefore have a similar TDM. In fact, preliminary calculations from Jeremy Hutson have identified a crossing between the least-bound g-wave state, $|-1(1,3)g(1,3)\rangle$, and the $|-6(2,4)d(2,3)\rangle$ state at a field of 192.7 G. Ramping the field down to 181.4 G would not yet reach the next avoided crossing, such that the molecule remains in the g-wave state, which has a weaker coupling to the excited molecular state. The similar loss rates measured at 181.4 G and 185 G corroborate this interpretation. After the field ramps are reversed, separating the traps crosses the same TISR to dissociate the weakly-bound molecule into an atom pair again. A clearer understanding of the molecule's state could be gained by measuring the binding energy using either magnetic field modulation spectroscopy [162, 326, 327], or dissociating the molecule using a MW field [328–330], or performing single-photon spectroscopy using laser light with a wavelength near to 1557 nm [140]. Preliminary measurements using the latter approach were taken during the writing of this thesis and are presented in the next section.

6.6.3 Single-photon Spectroscopy of Molecular States

Figure 6.13 displays a series of measurements of the photoexcitation spectrum of a weakly-bound molecule. The molecule is lost when the energy of applied laser light is resonant with a transition from the weakly-bound state to the molecular excited state $|^3\Pi_1 v' = 29, J' = 1\rangle$ in the mixed $b^3\Pi$-$A^1\Sigma^+$ potential. The binding energy of a particular molecular state is dependent on the magnetic field. There is a bound state close to the dissociation threshold that has a magnetic moment similar to that of the atom pair. By measuring the photoexcitation spectrum at a range of magnetic fields, we can observe the molecular state traversing avoided crossings. Then, using knowledge of the magnetic moments of the atoms and the least-bound state, we extract the magnetic moments of the electronic excited state and the other bound

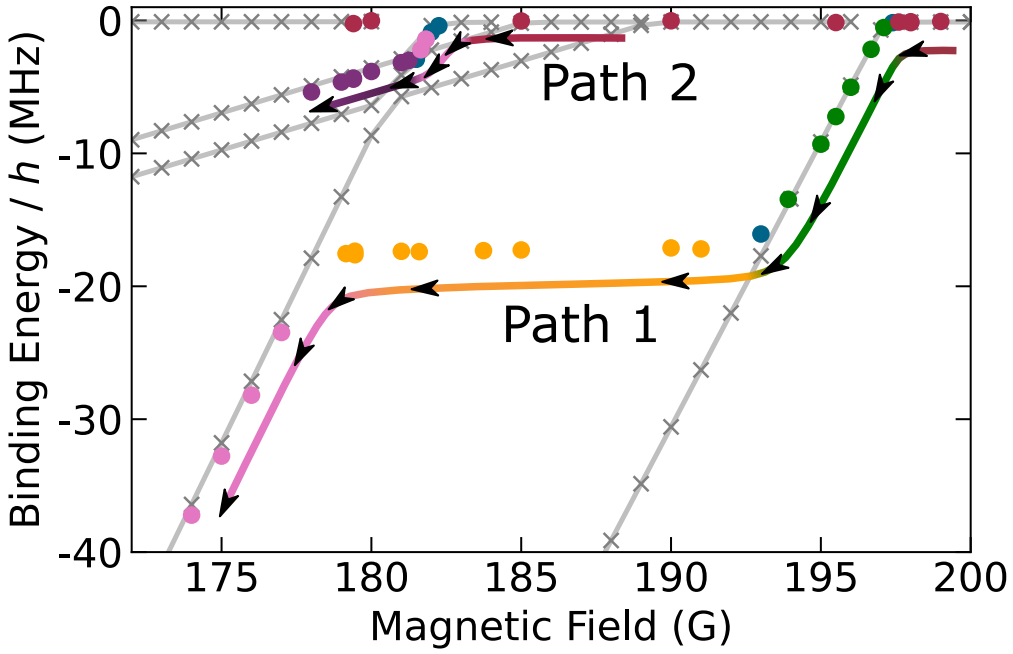

Figure 6.13: Measurements of the molecular binding energy extracted from photoexcitation spectra, relative to the atomic dissociation threshold. The grey crosses are theoretical predictions of the molecular binding energy following the calculations in Ref. [162], and the grey lines guide the eye. The red data points are taken without magnetic field ramps. The green, yellow, and pink data points are taken after a series of downwards magnetic field ramps starting at 205 G: path 1. The change in binding energy with magnetic field reveals transitions between different molecular states, including a previously unobserved state (yellow). The pink and purple data points with energy > -10 MHz are taken after a series of downwards magnetic field ramps starting at 190 G: path 2. The blue points indicate points which are likely to be mixed states. The data in this figure was taken by coworkers during the writing of this thesis.

states.

The experiment used to measure the photoexcitation spectrum follows mostly the same steps as the association sequence outlined in this thesis, but with a few modifications. A Rb atom is prepared in the motional ground state of an 817 nm tweezer, and a Cs atom is prepared in the motional ground state of a 1064 nm tweezer. Then the bias and jump coils are turned on to produce a static magnetic field of either 190 G or 205 G. Subsequently, the 817 nm tweezer is translated to merge with the 1064 nm tweezer so that the atoms are transferred to a common trap with minimal motional excitation. Then the magnetic field is ramped to a variable hold field and after allowing 5 ms for the field to settle, light with a wavelength of 1557 nm is pulsed on to cause photoexcitation of the molecule when on resonance with a bound-bound transition. The photoexcitation is observed as an increase in the probability of not detecting atoms, $P_{2\to 0}$, after reversing the magnetic field ramps and separating the traps.

Mapping out the photoexcitation spectrum as a function of magnetic field allows us to identify several different bound states. We fit the measured resonant photoexcitation frequencies to theoretical predictions of the binding energy that were previously calculated in Ref. [162]. The results of the fit are an offset frequency and a magnetic moment for the excited state of $-0.502(2)\,\mu_{\mathrm{B}}$, having fixed the magnetic moment and binding energy of the least-bound $|-1(1,3)s(1,3)\rangle$ state at $-1.3\,\mu_{\mathrm{B}}$ and 110 kHz respectively [162]. The fit implicitly identifies four out of the five states visible in Figure 6.13.

The red points in Figure 6.13 are taken with the magnetic field held constant. From the fit, we identify the red points as photoexcitation from the least-bound $|-1(1,3)s(1,3)\rangle$ state. Without crossing a Feshbach resonance, the atom pair can only enter a bound state if they cross a TISR during the merging of the traps. Since the atom pair state does not have a strong coupling to the molecular excited state, the observation of photoexcitation without magnetoassociation is strong evidence for association by merging.

Ramping the magnetic field down from 205 G to a variable end point, the molecular state follows path 1 in Figure 6.13. The magnetic field is held constant after the ramp for the photoexcitation pulse. Ramping over

the Feshbach resonance at 197.1 G transfers the least-bound state into the $|-6(2,4)d(2,3)\rangle$ state with a fitted magnetic moment of $1.67(3)\,\mu_{\mathrm{B}}$, consistent with an expected value of $1.7\,\mu_{\mathrm{B}}$ [163]. The ability to transfer into the $|-6(2,4)d(2,3)\rangle$ state is strong evidence for association by merging. This also offers an explanation for the loss rate measurements presented in Section 6.6, where the loss rate increased after crossing the Feshbach resonance. The $|-6(2,4)d(2,3)\rangle$ state is expected to have a larger Franck-Condon overlap with a molecular excited state, compared to the least-bound state with its comparatively long-range wavefunction. Subsequently following the avoided crossing at 193 G is also consistent with the loss rate measurements if the state identified with the orange points has a similar transition dipole moment to the least-bound $|-1(1,3)s(1,3)\rangle$ state. The blue point at 193 G is expected to be a mixed state. Although the state identified with the orange points has not been observed in previous experiments, preliminary theoretical calculations show that the $|-1(1,3)g(1,3)\rangle$ state has binding energies and avoided crossings consistent with the data in Figure 6.13. Continuing the magnetic field ramp below 178 G transfers the molecule into the $|-6(2,4)d(2,4)\rangle$ state, with a magnetic dipole moment of $1.973(6)\,\mu_{\mathrm{B}}$ extracted from a fit to the pink points in Figure 6.13, close to the expected value of $2.0\,\mu_{\mathrm{B}}$ [163].

If the magnetic field ramp instead begins at 190 G, the molecular state follows path 2 in Figure 6.13. Crossing the Feshbach resonance at 181.6 G transfers the molecule into the $|-6(2,4)d(2,4)\rangle$ state, which then transfers into the $|-2(1,3)d(0,3)\rangle$ state for fields < 181.3 G. Fitting to the purple points gives a magnetic moment of $-0.78(2)\,\mu_{\mathrm{B}}$. This is a slight deviation from the expected value of $-0.9\,\mu_{\mathrm{B}}$ [163], which we attribute to inaccuracy in the magnetic field calibration that has a more significant effect when the binding energy has a weaker dependence on magnetic field.

In conclusion, the measurements of photoexcitation spectra are largely consistent with theoretical predictions if we assume that the initial state before any magnetic field ramps is the least-bound $|-1(1,3)s(1,3)\rangle$ state. It is most likely that the atoms are transferred into the least-bound state by crossing a TISR while the traps are merged. On reflection, it is clear that we inadvertently optimised the process of association during the merge by assuming that the signal of molecular association would be a lifetime significantly shorter

than that of the atom pair. Hindsight reveals that the observed shorter lifetime was actually the result of transferring into a more deeply bound state, which is only possible if we associated the atoms during the merge.

6.7 Conclusion

We have demonstrated the creation of a Feshbach molecule with a conversion efficiency of 0.57(3) limited only by technical factors reducing the relative motional ground state preparation fidelity. Our measured conversion efficiency is a significant improvement upon the other experiments associating atoms into molecules using optical tweezers: NaCs molecules have been assembled with a conversion efficiency of 0.47(1) [99], and ^{85}Rb^{87}Rb molecules have been assembled with a conversion efficiency of ~ 0.3 [155].

Achieving efficient association required knowledge of the effect of the tweezer light, which can Stark-shift the position of the Feshbach resonance and cause 2-body loss through photoexcitation of the weakly-bound state. Furthermore, the confinement of the harmonic potential affects the energy spectrum. We observe evidence of inelastic CIRs in the appearance of multiple loss features in Feshbach spectroscopy measurements. We also suggest that measurements of molecular loss rates after manipulating the bound state with magnetic field ramps provide evidence for association by merging; transferring to a bound state by crossing a TISR during the merging of the tweezers. Conclusive evidence for this hypothesis is given in single-photon spectroscopy measurements of molecular binding energies, which also identify a previously unobserved moleular state: $|-1(1,3)g(1,3)\rangle$.

The influence of CIRs and TISRs presents a range of interesting opportunities for future research. At a base level, an understanding of the energy spectrum is required in order to manipulate couplings between atom-pair and molecular states and associate a molecule. At a more advanced level, TISRs could be used to associate atoms without the requirement for large external magnetic fields [270, 315], or to produce quantum gates [269]. The collaboration between theory and experiment has already led to the development of simulations which accurately predict the appearance of inelastic

CIRs [303, 310, 331]. Our optical tweezers experiment offers an ideal environment for further investigation, making full use of the precise control over trap positions and the high-fidelity preparation of a single quantum state.

Overall, the efficient preparation of a molecule in a weakly-bound state provides the starting point for stimulated Raman adiabatic passage into the rovibrational ground state, following a scheme developed for RbCs molecules in bulk mixtures [140, 158]. This work lays the foundations for experiments manipulating RbCs molecules in an optical tweezer array.

Chapter 7

Outlook and Conclusion

7.1 Summary

This work details the stages of an experimental routine for preparing ultracold ^{87}RbCs molecules in an optical tweezer array. Our method assembles a single molecule starting from a Rb atom in an 817 nm tweezer, and a Cs atom in a 938 nm tweezer. The atoms are loaded into and cooled to the motional ground states of separate tweezers before a merging sequence transfers them to a common trap. We have demonstrated association of a weakly-bound molecule, in preparation for the final stage of the experiment which will be transferring the molecule to the rovibrational ground state. Each of the stages of the experiment has been extensively characterised and optimised, allowing us to obtain a high probability of preparing a molecule, limited by technical factors.

The first stage of our protocol is preparing a pair of atoms in separate tweezers and initialising their spin states. We begin by increasing the probability of loading atoms into the tweezers with a rearrangement scheme. Initially we image an array of 817 nm tweezers and an array of 938 nm tweezers generated by driving their respective AODs with multitone RF signals, where the phases of the tones are chosen to mitigate intermodulation effects. An occupied trap is selected from the array, such that we prepare a Rb atom and a Cs atom with a probability of 0.75(4). Characterisation measurements of the tweezer traps are used to predict the intensity at the atoms, such that we

can calculate the light shifts and trap frequencies that the atoms experience. With this knowledge we initialise the atomic spin state with a high-fidelity optical pumping scheme, and similarly high-fidelity MW transitions and 2-photon Raman transitions transfer the atoms between spin states.

The second stage of the molecular assembly protocol is cooling the atoms to the motional ground state of their respective traps. We have designed a pulsed RSC protocol that cools an atom from outside the LD regime by making use of different orders of sideband transitions. The RSC protocol is robust against common experimental imperfections, making it suitable for application to an array of atoms. Moreover, the RSC protocol also permits high-fidelity motional ground state preparation. After applying the RSC pulse sequence, we measured a 3D motional ground state occupation probability of $0.95^{+0.03}_{-0.04}$ for a Cs atom in a 938 nm tweezer, and $0.86^{+0.03}_{-0.04}$ for a Rb atom in an 814 nm tweezer.

In order to merge the traps with minimal motional excitation, we analysed the dominant sources of heating. We designed a merging sequence with an optimised trajectory and appropriate trap depths, such that we were able to prepare an atom pair in the relative motional ground state of a common 1064 nm tweezer with a probability of 0.81(8).

The next stage is to transfer the atom pair into a molecular bound state. An atom pair can be associated into a bound state by ramping a magnetic field across a Feshbach resonance. In an optical tweezer trap, it is also important to consider the effects of confinement. For example, anharmonicity in the trapping potential creates coupling to a bound state with excited COM motion at an inelastic confinement-induced resonance. Furthermore, crossing a trap-induced shape resonance while merging the traps could transfer the atom pair into a weakly bound state. The tweezer light can also influence the magnetic field at which the Feshbach resonance occurs through the AC Stark shift of molecular energy levels. Through a thorough characterisation of AC Stark shifts, we locate a molecular transition at a frequency of 281.783(17) THz and fit a TDM of $0.064(2)\,ea_0$. We choose a tweezer frequency of 281.624 THz, sufficiently far from the molecular transition, so that we are able to create and retain a weakly-bound molecule. Technical factors limit the efficiency of our molecular-assembly protocol, the dominant factor

being motional excitation while merging the traps. Nevertheless, we have demonstrated that our protocol prepares a weakly-bound molecular state in 57(3) % of the experimental runs that started with a Rb atom and a Cs atom.

Optical tweezers are particularly well suited for efficient molecular assembly. The isolation of single particles circumvents collisional losses while preparing the high phase space densities required for efficient association. In experiments using bulk mixtures, inelastic collisions between atoms and weakly-bound molecules limit the conversion efficiency to $\sim 30\,\%$ [163, 332]. Even if the molecules are protected from lossy collisions, sometimes loss is an unavoidable part of the cooling process, such as in evaporative cooling that relies on hot atoms escaping the trap [333]. However, the motional ground state preparation using RSC conserves the atom number. Despite the high conversion efficiency from atoms to molecules, starting each run with only a few atoms means that our optical tweezers experiment currently prepares fewer molecules per second than the experiments working with bulk mixtures, even with our fast cycle time of $\sim 0.5\,\mathrm{s}$. Future adaptations to our experiment will scale up the processes outlined in this thesis to assemble an array of molecules in parallel. Using rearrangement techniques will allow us to prepare defect-free arrays of molecules, overcoming the challenge of achieving high filling fractions faced by experiments using optical lattices [334, 335].

Although most of the molecular-assembly protocol is based on well-established techniques, the confinement of the atom pair influences their interactions in ways that are not yet fully understood. In the previous chapter, we presented conclusive evidence that the atom pair is associated into a bound state before the magnetic field ramp across the Feshbach resonance, most likely by crossing a trap-induced shape resonance (TISR) during the merge. Single-photon spectroscopy measurements of the molecular binding energy reveal which state the molecule occupies, and we show that magnetic field ramps follow a path through avoided crossings which is only possible if the atoms are associated during the merge.

Future work will investigate the process of association by merging. We anticipate that the trap depths during the merge and the positions of the traps at the end of the merge will be important parameters for the investigation. We also note that since the background interspecies scattering length for

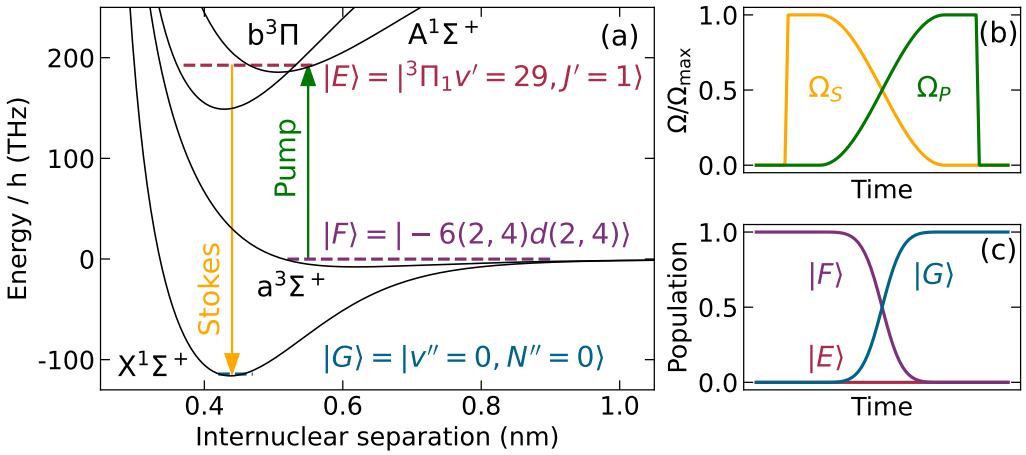

Figure 7.1: The optical transitions involved in the STIRAP to the rovibrational ground state. (a) The pump laser couples the weakly-bound Feshbach molecule state to an excited state in the mixed $b^3\Pi - A^1\Sigma^+$ potential. The Stokes laser couples the excited state to the rovibrational ground state. (b) The time-dependent Rabi frequencies of the pump and Stokes beams. (c) STIRAP transfers population from the weakly-bound state to the rovibrational ground state without populating the excited state.

RbCs is only weakly dependent on magnetic field [162], association by merging presents a method for associating molecules without the need for large external magnetic fields. Modifying the interspecies scattering length during the merge using magnetic fields near to a Feshbach resonance adds another degree of control which expands the prospects for future research [269].

7.2 Outlook

7.2.1 STIRAP

Stimulated Raman adiabatic passage (STIRAP) is an established process for efficiently transferring a molecule to the rovibrational ground state [135–144]. The process has been characterised in detail in the context of ^{87}RbCs molecules [158]. The basic principle is that incident laser beams create a dressed state which can be manipulated to coherently transfer the molecule into the rovibrational ground state.

The STIRAP process can be understood within the framework of a 3-level system. Figure 7.1 displays a 3-level system of molecular states $\{|F\rangle, |E\rangle, |G\rangle\}$ with a pump laser that couples $|F\rangle$ to $|E\rangle$ with Rabi frequency Ω_P and a Stokes laser that couples $|E\rangle$ to $|G\rangle$ with Rabi frequency Ω_S. We set the lasers to single-photon resonance, which also satisfies the two-photon resonance condition. The state $|F\rangle$ projects fully onto a dark dressed state, $|a\rangle = \cos(\theta)|F\rangle - \sin(\theta)|G\rangle$ where $\tan(\theta) = \Omega_P(t)/\Omega_S(t)$, when $\Omega_P(t=0) = 0$ and $\Omega_S(t=0) \neq 0$. The dark state can then be transformed by adiabatically adjusting the pump and Stokes powers. For example, Figure 7.1(b) illustrates a modulation of the pump and Stokes beam powers with a time-dependent profile of $\sin^2(\pi t/2T)$ and $\cos^2(\pi t/2T)$ respectively. Figure 7.1(c) displays the resulting projection of the dark state, such that the state projects fully onto $|G\rangle$ when $\Omega_S(t=T) = 0$ and $\Omega_P(t=T) \neq 0$.

The STIRAP process requires an appropriate choice of excited state in order to work efficiently. The $|E\rangle$ state must have a significant overlap with both the initial state after magnetoassociation (which is in the $a^3\Sigma^+$ potential), and the rovibrational ground state (which is in the $X^1\Sigma^+$ potential). The $|b^3\Pi_1\ v' = 29, J' = 1\rangle$ state is ideally suited for this purpose, as it has strong coupling to $|F\rangle = |-6(2,4)d(2,4)\rangle$ and the spin-orbit coupling of the $^3\Pi$ and $A^1\Sigma^+$ potentials gives the state singlet character, permitting strong coupling to $|G\rangle = |X^1\Sigma^+\ v'' = 0, N'' = 0\rangle$. Furthermore, the excited state $|b^3\Pi_1\ v' = 29, J' = 1\rangle$ has a long lifetime [141] compared to achievable Rabi frequencies and laser linewidths, which is important for maintaining adiabaticity and reducing the effects of decoherence [336]. Finally, in order to avoid coupling to multiple excited states, it is important to minimise AC Stark shifts from the trapping light and minimise the linewidth of the frequency difference between the pump and Stokes lasers.

Figure 7.1(a) displays the optical transitions that couple the molecular states, which are driven by frequency-stabilised lasers. Development of the STIRAP hardware has proceeded alongside the work described in this thesis. Our setup follows a scheme developed for a bulk gas of RbCs [337]. The pump laser has a wavelength of 1557 nm and the Stokes laser has a wavelength of 977 nm. Both lasers are stabilised to a single optical cavity with a finesse of $2.00(8) \times 10^4$. The cavity is constructed from ultra-low-expansion

gas and mounted in a vacuum chamber at a temperature of 35 °C near the zero-expansion temperature of the glass. Fibre-coupled EOMs are used for continuous frequency stabilisation with a Pound-Drever-Hall setup.

The single-photon spectroscopy in Section 6.6.3 demonstrates the first step of coupling the weakly-bound state to the excited state. The next step involves using dark state spectroscopy to identify the resonant frequency for the Stokes transition to the rovibrational ground state. Then we expect to achieve a one-way conversion efficiency to the rovibrational ground state matching the 92 % previously demonstrated for RbCs in a bulk gas [158].

7.2.2 Expansion to an Array

To capitalise on the full potential of the optical tweezers platform, the molecular assembly process will be expanded to produce an array of molecules in parallel. Achieving this goal involves overcoming several technical challenges associated with generating large-scale uniform-intensity arrays.

The first challenge is sourcing sufficient laser power. At some stage, the desire for larger arrays will require purchasing either higher-power laser sources or optical amplifiers. Furthermore, the optical fibres delivering the tweezer light to the main experiment table will also need to be upgraded. Currently, the onset of polarisation noise when the light propagating through the fibre surpasses a threshold power impedes the generation of large arrays. We intend to resolve this issue by replacing the Thorlabs patch cables with patch cables designed for high-power laser transmission. Once sufficient power is available, the next challenge is generating a uniform array of traps.

The powers of traps in an array can be normalised using feedback from CCD images. When the array is generated by driving an AOD with a multitone RF signal, it is important to avoid intermodulation effects by choosing appropriate phases for the individual tones. It is quite feasible to balance the trap powers to within $< 5\,\%$. Alongside the implementation of our RSC protocol, which is designed to be robust against deviations in the two-photon detuning, we should be able to prepare an array of atoms in the motional ground state of their respective traps.

Our first attempt at cooling Rb atoms in an array of four tweezers suffered from inhomogeneous polarisation across the array. We identified that our AODs modify the polarisation of the light in a manner dependent on the frequency of the input RF signal. Although the change in polarisation is relatively small, the associated change in the vector light shift experienced by the atoms is detrimental to the OP fidelity. We have now installed polarisers after each AOD to reassert the desired polarisation. With this modification, we anticipate that the vector light shift from the tweezer will be uniform across the array. We can also generate an array of 1064 nm tweezers using the SLM, with the advantage that the SLM would generate an array of traps with the same polarisation.

Our protocols for rearrangement and merging schemes are simply generalised to 1D arrays. The rearrangement will be performed along the horizontal axis, with the Cs atom array vertically displaced from the Rb atom array. Merging the arrays involves a vertical translation. While defect-free arrays of ~ 50 atoms have been prepared in 1D, expansion to larger arrays is more easily achieved in a 2D array [3, 4]. Implementing rearrangement in a 2D array will require implementing efficient sorting algorithms [5, 88, 94]. When rearranging dual-species arrays, the sorting movements simply avoid undesired collisions when the Cs atom array is displaced from the Rb atom array in both the horizontal and vertical directions and there is sufficient spacing between traps that a moving tweezer could pass between them.

7.2.3 Dipole-dipole Interactions Between Molecules

Applications for ultracold molecules in optical tweezer arrays rely on the dipole-dipole interaction to perform gate operations [15, 44, 45, 48]. It is critical that the the time taken to perform a gate operation is much faster than the decoherence timescale. The gate time is set by the interaction strength, which depends on the separation of the molecules and the dipole moment. For RbCs, a laboratory-frame electric dipole moment of $d_{12} \sim 0.7\,\mathrm{D}$ could be realised by applying an external electric field of $2\,\mathrm{kV\,cm^{-1}}$ [140]. For optical tweezers separated by $R = 0.9\,\mu\mathrm{m}$, the resulting timescale for the dipole-dipole interaction is $h/V_{\mathrm{dd}} = 4\pi\epsilon_0 h R^3/d_{12}^2 \sim 10\,\mathrm{ms}$. The laboratory-

frame dipole moment could instead be induced using a MW field to create a superposition of rotational states, and an entangling gate has been proposed that takes 7.3 ms [15]. Decreasing the separation between molecules is an attractive solution to speeding up the time taken for the gate operation. The interaction strength can be increased by several orders of magnitude by preparing molecules in state-dependent traps separated by $< 0.5\,\mu$m [130, 338].

On the other hand, the coherence time is generally limited by dephasing caused by AC Stark shifts from the trapping light. The first demonstration of entanglement in an optical tweezer array of CaF molecules observed dephasing of spin-exchange oscillations with a 1/e time of 2.5(3) ms. Several actions can be taken to reduce the dephasing. Motional ground state cooling reduces thermal dephasing, analogous to the dephasing discussed in Section 5.2.2. Furthermore, state-dependent AC Stark shifts can be suppressed using magic-polarisation traps [111–113, 121] and magic-wavelength traps [122]. The molecular structure of the RbCs molecule in particular can be exploited to realise a magic-wavelength trapping condition between multiple rotational states [123]. Implementing motional ground state cooling and magic-trapping will extend the coherence time of spin-exchange interactions to approach the > 5 s coherence time demonstrated for maintaining a superposition of hyperfine states [113].

7.2.4 Hybrid Quantum Systems

A growing field of research looks to combine systems of molecules with Rydberg atoms. Proposals for quantum gates take advantage of the long coherence time of qubits encoded in molecular states, and combine this with fast interactions mediated by Rydberg atoms [339–341]. Using Rydberg atoms as mediators for molecular qubit interactions achieves fast gate times of $\sim 1\,\mu$s, with estimated fidelity exceeding 99 % aided by the fact that the gate has little sensitivity to the molecular qubit's motional state. In addition, measuring fluorescence on a cycling transition of the atom permits non-destructive readout of the molecular qubit state [340–344].

An alternative direction for future research seeks to assemble an ultralong-

range triatomic Rydberg molecule [345–347]. These polyatomic molecules have an extreme sensitivity to external electric fields that could be utilised for precision measurements.

Our optical tweezers experiment is an ideal platform to realise a hybrid quantum system of ultracold RbCs molecules with Rydberg atoms.

7.3 Concluding Remarks

This thesis demonstrates progress towards the preparation of rovibrational ground-state ^{87}RbCs molecules in an optical tweezer array. We have demonstrated control over the external and internal states of single atoms in optical tweezers. The high-fidelity preparation of an atom pair in the relative motional ground state of a common trap led to efficient association of a weakly-bound molecular state. Already we have uncovered phenomena that present fruitful avenues for future research, such as the influence of confinement on interactions between an atom pair. Yet, the goal of preparing an array of ultracold molecules is also within reach. The experiment will soon be ready to transfer a molecule to the rovibrational ground state, and the process is scalable to assemble an array of molecules in parallel. This experiment is full of potential for research in quantum science.

Appendix A

3D Raman Sideband Cooling Pulse Sequence

Here we present a table of typical parameters used for the Raman sideband cooling pulse sequence outlined in Chapter 4. We note that after the work presented in Chapter 5, we decided to replace the RB3 pulses with RB2 pulses, and have achieved the same motional ground state occupation probability.

Group 1	axial $\Delta n = -4$	5 repetitions		
Cs Sideband Transition Frequency (kHz)	Rb Sideband Transition Frequency (kHz)	Axis	Rb Raman Rabi Frequency (kHz)	Duration (μs)
68	100	Axial	4.5	272
76	110	Radial 1	21	70
68	100	Axial	4.5	272
112	170	Radial 2	27	60
Group 2	axial $\Delta n = -3$	10 repetitions		
Cs Sideband Transition Frequency (kHz)	Rb Sideband Transition Frequency (kHz)	Axis	Rb Raman Rabi Frequency (kHz)	Duration (μs)
51	75	Axial	4.5	251
76	110	Radial 1	21	70

51	75	Axial	4.5	251
112	170	Radial 2	27	60
Group 3	axial $\Delta n = -2$	10 repetitions		
Cs Sideband Transition Frequency (kHz)	Rb Sideband Transition Frequency (kHz)	Axis	Rb Raman Rabi Frequency (kHz)	Duration (μs)
34	50	Axial	4.5	224
76	110	Radial 1	21	70
34	50	Axial	4.5	224
112	170	Radial 2	27	60
Group 4	axial $\Delta n = -2, -1$	15 repetitions		
Cs Sideband Transition Frequency (kHz)	Rb Sideband Transition Frequency (kHz)	Axis	Rb Raman Rabi Frequency (kHz)	Duration (μs)
34	50	Axial	4.5	224
76	110	Radial 1	21	100
17	25	Axial	4.5	188
112	170	Radial 2	27	60
17	25	Axial	4.5	281
76	110	Radial 1	21	100
34	50	Axial	4.5	224
76	110	Radial 1	21	70
17	25	Axial	4.5	188
112	170	Radial 2	27	60

Table A.1: The pulse sequence used for simultaneous RSC of Rb and Cs. The sideband transition frequency is the difference between the frequency of the carrier transition and the desired sideband transition. The quoted Raman Rabi frequencies are mean values. For a convolution of a Tukey profile and a square pulse, as used to pulse shape the radial directions, this is different from the peak Rabi frequency by a factor of 1.22. For a Blackman-Harris profile the mean Rabi frequency differs from the peak Rabi frequency by a factor of 2.79. The duration of the OP pulses is 15 μs and the entire pulse sequence lasts 45.05 ms.

Bibliography

[1] D. S. Weiss et al., "Another way to approach zero entropy for a finite system of atoms", *Phys. Rev. A* 70 (2004), 040302(R).

[2] Y. Miroshnychenko et al., "An atom-sorting machine", *Nature* 442, 7099 (2006), p. 151.

[3] D. Barredo, S. de Léséleuc, V. Lienhard, T. Lahaye, and A. Browaeys, "An atom-by-atom assembler of defect-free arbitrary two-dimensional atomic arrays", *Science* 354, 6315 (2016), pp. 1021–1023.

[4] M. Endres et al., "Atom-by-atom assembly of defect-free one-dimensional cold atom arrays", *Science* 354, 6315 (2016), pp. 1024–1027.

[5] W. Lee, H. Kim, and J. Ahn, "Defect-free atomic array formation using the Hungarian matching algorithm", *Phys. Rev. A* 95 (2017), p. 053424.

[6] D. Stuart and A. Kuhn, "Single-atom trapping and transport in DMD-controlled optical tweezers", *New J. Phys.* 20 (2018), p. 023013.

[7] D. J. Wineland et al., "Experimental Issues in Coherent Quantum-State Manipulation of Trapped Atomic Ions", *J. Res. Natl. Inst. Stand. Technol.* 103, 3 (1998), pp. 259–328.

[8] C. Weitenberg, S. Kuhr, K. Mølmer, and J. F. Sherson, "A quantum computation architecture using optical tweezers", *Phys. Rev. A* 84, 032322 (2011).

[9] D. Jaksch, C. Bruder, J. I. Cirac, C. W. Gardiner, and P. Zoller, "Cold Bosonic Atoms in Optical Lattices", *Phys. Rev. Lett.* 81, 15 (1998), pp. 3108–3111.

[10] B. Capogrosso-Sansone, C. Trefzger, M. Lewenstein, P. Zoller, and G. Pupillo, "Quantum Phases of Cold Polar Molecules in 2D Optical Lattices", *Phys. Rev. Lett.* 104, 12 (2010), p. 125301.

[11] I. Bloch, J. Dalibard, and S. Nascimbène, "Quantum simulations with ultracold quantum gases", *Nat. Phys.* 8, 4 (2012), pp. 267–276.

[12] T. Wilk et al., "Entanglement of Two Individual Neutral Atoms Using Rydberg Blockade", *Phys. Rev. Lett.* 104, 1 (2010), p. 010502.

[13] T. M. Graham et al., "Rydberg-Mediated Entanglement in a Two-Dimensional Neutral Atom Qubit Array", *Phys. Rev. Lett.* 123, 23 (2019), p. 230501.

[14] H. Levine et al., "Parallel Implementation of High-Fidelity Multiqubit Gates with Neutral Atoms", *Phys. Rev. Lett.* 123 (2019), p. 170503.

[15] M. Hughes et al., "Robust entangling gate for polar molecules using magnetic and microwave fields", *Phys. Rev. A* 101, 6 (2020), p. 062308.

[16] P. Zoller et al., "Quantum information processing and communication", *The European Physical Journal D - Atomic, Molecular, Optical and Plasma Physics* 36, 2 (2005), pp. 203–228.

[17] I. M. Georgescu, S. Ashhab, and F. Nori, "Quantum simulation", *Rev. Mod. Phys.* 86, 1 (2014), pp. 153–185.

[18] R. Blatt and C. F. Roos, "Quantum simulations with trapped ions", *Nat. Phys.* 8, 4 (2012), pp. 277–284.

[19] J. Zhang et al., "Observation of a many-body dynamical phase transition with a 53-qubit quantum simulator", *Nature* 551, 7682 (2017), pp. 601–604.

[20] C. Monroe et al., "Programmable quantum simulations of spin systems with trapped ions", *Rev. Mod. Phys.* 93, 2 (2021), p. 025001.

[21] S. Ebadi et al., "Quantum phases of matter on a 256-atom programmable quantum simulator", *Nature* 595, 7866 (2021), pp. 227–232.

[22] P. Scholl et al., "Quantum simulation of 2D antiferromagnets with hundreds of Rydberg atoms", *Nature* 595, 7866 (2021), pp. 233–238.

[23] A. Micheli, G. K. Brennen, and P. Zoller, "A toolbox for lattice-spin models with polar molecules", *Nat. Phys.* 2 (2006), pp. 341–347.

[24] R. Barnett, D. Petrov, M. Lukin, and E. Demler, "Quantum magnetism with multicomponent dipolar molecules in an optical lattice", *Phys. Rev. Lett.* 96, 19 (2006), p. 190401.

[25] H. P. Büchler et al., "Strongly Correlated 2D Quantum Phases with Cold Polar Molecules: Controlling the Shape of the Interaction Potential", *Phys. Rev. Lett.* 98 (2007), p. 060404.

[26] A. V. Gorshkov, K. R. A. Hazzard, and A. M. Rey, "Kitaev honeycomb and other exotic spin models with polar molecules", *Mol. Phys.* 111, 12-13 (2013), pp. 1908–1916.

[27] T. Lahaye, C. Menotti, L. Santos, M. Lewenstein, and T. Pfau, "The physics of dipolar bosonic quantum gases", *Reports on Progress in Physics* 72, 12 (2009), p. 126401.

[28] K. R. A. Hazzard et al., "Quantum correlations and entanglement in far-from-equilibrium spin systems", *Phys. Rev. A* 90, 6 (2014), p. 063622.

[29] H. Katori, M. Takamoto, V. G. Pal'chikov, and V. D. Ovsiannikov, "Ultrastable Optical Clock with Neutral Atoms in an Engineered Light Shift Trap", *Phys. Rev. Lett.* 91, 17 (2003).

[30] M. A. Norcia et al., "Seconds-scale coherence in a tweezer-array optical clock", *Science* 366 (2019), pp. 93–97.

[31] I. S. Madjarov et al., "An Atomic-Array Optical Clock with Single-Atom Readout", *Phys. Rev. X* 9 (2019), p. 041052.

[32] P. W. Shor, "Algorithms for quantum computation: discrete logarithms and factoring", in: *Proceedings 35th Annual Symposium on Foundations of Computer Science*, 1994, pp. 124–134.

[33] D. P. DiVincenzo, "The physical implementation of quantum computation", *Fortschritte der Physik* 48, 9-11 (2000), pp. 771–783.

[34] H. Häffner, C. F. Roos, and R. Blatt, "Quantum computing with trapped ions", *Phys. Rep.* 469, 4 (2008), pp. 155–203.

[35] C. D. Bruzewicz, J. Chiaverini, R. McConnell, and J. M. Sage, "Trapped-ion quantum computing: Progress and challenges", *Appl. Phys. Rev.* 6, 2 (2019), p. 021314.

[36] M. Saffman, "Quantum computing with atomic qubits and Rydberg interactions: Progress and challenges", *J. Phys. B* 49, 20 (2016).

[37] C. S. Adams, J. D. Pritchard, and J. P. Shaffer, "Rydberg atom quantum technologies", *J. Phys. B* 53, 1 (2019), p. 012002.

[38] F. Arute et al., "Quantum supremacy using a programmable superconducting processor", *Nature* 574, 7779 (2019), pp. 505–510.

[39] H.-L. Huang, D. Wu, D. Fan, and X. Zhu, "Superconducting quantum computing: a review", *Science China Information Sciences* 63, 8 (2020), pp. 1–32.

[40] D. Loss and D. P. DiVincenzo, "Quantum computation with quantum dots", *Phys. Rev. A* 57, 1 (1998), p. 120.

[41] C. Kloeffel and D. Loss, "Prospects for spin-based quantum computing in quantum dots", *Annu. Rev. Condens. Matter Phys.* 4, 1 (2013), pp. 51–81.

[42] J. L. O'brien, "Optical quantum computing", *Science* 318, 5856 (2007), pp. 1567–1570.

[43] H.-S. Zhong et al., "Quantum computational advantage using photons", *Science* 370, 6523 (2020), pp. 1460–1463.

[44] D. DeMille, "Quantum Computation with Trapped Polar Molecules", *Phys. Rev. Lett.* 88 (2002), p. 067901.

[45] S. F. Yelin, K. Kirby, and R. Côté, "Schemes for robust quantum computation with polar molecules", *Phys. Rev. A* 74, 5 (2006), p. 050301.

[46] J. Zhu, S. Kais, Q. Wei, D. Herschbach, and B. Friedrich, "Implementation of quantum logic gates using polar molecules in pendular states", *J. Chem. Phys.* 138, 2 (2013), p. 024104.

[47] F. Herrera, Y. Cao, S. Kais, and K. B. Whaley, "Infrared-dressed entanglement of cold open-shell polar molecules for universal matchgate quantum computing", *New J. Phys.* 16 (2014), p. 075001.

[48] K.-K. Ni, T. Rosenband, and D. D. Grimes, "Dipolar exchange quantum logic gate with polar molecules", *Chem. Sci.* 9, 33 (2018), pp. 6830–6838.

[49] J. Beugnon et al., "Two-dimensional transport and transfer of a single atomic qubit in optical tweezers", *Nat. Phys.* 3 (2007), pp. 696–699.

[50] M. Schlosser et al., "Fast transport, atom sample splitting and single-atom qubit supply in two-dimensional arrays of optical microtraps", *New J. Phys.* 14 (2012), p. 123034.

[51] D. Barredo, V. Lienhard, S. de Léséleuc, T. Lahaye, and A. Browaeys, "Synthetic three-dimensional atomic structures assembled atom by atom", *Nature* 561 (2018), pp. 79–82.

[52] L. Anderegg et al., "An Optical Tweezer Array of Ultracold Molecules", *Science* 365, 6458 (2019), pp. 1156–1158.

[53] C. Gross and I. Bloch, "Quantum simulations with ultracold atoms in optical lattices", *Science* 357, 6355 (2017), pp. 995–1001.

[54] G. Thalhammer et al., "Long-Lived Feshbach Molecules in a Three-Dimensional Optical Lattice", *Phys. Rev. Lett.* 96, 5 (2006), p. 050402.

[55] C. Ospelkaus et al., "Ultracold Heteronuclear Molecules in a 3D Optical Lattice", *Phys. Rev. Lett.* 97, 12 (2006), p. 120402.

[56] F. Deuretzbacher et al., "Heteronuclear molecules in an optical lattice: Theory and experiment", *Phys. Rev. A* 77, 3 (2008), p. 032726.

[57] W. S. Bakr, J. I. Gillen, A. Peng, S. Fölling, and M. Greiner, "A quantum gas microscope for detecting single atoms in a Hubbard-regime optical lattice", *Nature* 462, 7269 (2009), pp. 74–77.

[58] J. F. Sherson et al., "Single-atom-resolved fluorescence imaging of an atomic Mott insulator", *Nature* 467, 7311 (2010), pp. 68–72.

[59] A. Alberti et al., "Super-resolution microscopy of single atoms in optical lattices", *New J. Phys.* 18 (2016), p. 053010.

[60] M. McDonald, J. Trisnadi, K. Yao, and C. Chin, "Superresolution microscopy of cold atoms in an optical lattice", *Phys. Rev. X* 9 (2019), p. 021001.

[61] C. Becker et al., "Ultracold quantum gases in triangular optical lattices", *New J. of Phys.* 12, 6 (2010), p. 065025.

[62] P. Soltan-Panahi et al., "Multi-component quantum gases in spin-dependent hexagonal lattices", *Nature Physics* 7, 5 (2011), pp. 434–440.

[63] M. Greiner, O. Mandel, T. Esslinger, T. W. Hänsch, and I. Bloch, "Quantum phase transition from a superfluid to a Mott insulator in a gas of ultracold atoms", *Nature* 415, 6867 (2002), pp. 39–44.

[64] A. Kumar, T.-Y. Wu, F. Giraldo, and D. S. Weiss, "Sorting ultracold atoms in a three-dimensional optical lattice in a realization of Maxwell's demon", *Nature* 561 (2018), pp. 83–87.

[65] A. Ashkin, "Optical Trapping and Manipulation of Neutral Particles Using Lasers", *Proceedings of the National Academy of Sciences* 94, 10 (1997), pp. 4853–4860.

[66] P. D. Gregory et al., "Sticky collisions of ultracold RbCs molecules", *Nat. Commun.* 10, 1 (2019), p. 3104.

[67] P. D. Gregory, J. A. Blackmore, S. L. Bromley, and S. L. Cornish, "Loss of Ultracold $Rb^{87}Cs^{133}$ Molecules via Optical Excitation of Long-Lived Two-Body Collision Complexes", *Phys. Rev. Lett.* 124, 163402 (2020), p. 163402.

[68] J. F. E. Croft, J. L. Bohn, and G. Quéméner, "Unified model of ultracold molecular collisions", *Phys. Rev. A* 102 (3 2020), p. 033306.

[69] M.-G. Hu et al., "Nuclear spin conservation enables state-to-state control of ultracold molecular reactions", *Nature Chemistry* 13, 5 (2021), pp. 435–440.

[70] P. Gersema et al., "Probing Photoinduced Two-Body Loss of Ultracold Nonreactive Bosonic $^{23}Na^{87}Rb$ and $^{23}Na^{39}K$ Molecules", *Phys. Rev. Lett.* 127 (16 2021), p. 163401.

[71] R. Bause et al., "Collisions of ultracold molecules in bright and dark optical dipole traps", *Phys. Rev. Research* 3 (3 2021), p. 033013.

[72] N. Schlosser, G. Reymond, and P. Grangier, "Collisional Blockade in Microscopic Optical Dipole Traps", *Phys. Rev. Lett.* 89, 2 (2002), p. 023005.

[73] T. Grünzweig, A. Hilliard, M. McGovern, and M. F. Andersen, "Near-deterministic preparation of a single atom in an optical microtrap", *Nat. Phys.* 6 (2010), pp. 951–954.

[74] B. J. Lester, N. Luick, A. M. Kaufman, C. M. Reynolds, and C. A. Regal, "Rapid production of uniformly-filled arrays of neutral atoms", *Phys. Rev. Lett.* 115, 7 (2015), p. 073003.

[75] M. O. Brown, T. Thiele, C. Kiehl, T.-W. Hsu, and C. A. Regal, "Gray-Molasses Optical-Tweezer Loading: Controlling Collisions for Scaling Atom-Array Assembly", *Phys. Rev. X* 9 (2019), p. 011057.

[76] A. Jenkins, J. W. Lis, A. Senoo, W. F. McGrew, and A. M. Kaufman, "Ytterbium Nuclear-Spin Qubits in an Optical Tweezer Array", *Phys. Rev. X* 12, 2 (2022), p. 021027.

[77] J. Ang'ong'a, C. Huang, J. P. Covey, and B. Gadway, "Gray molasses cooling of ^{39}K atoms in optical tweezers", *Phys. Rev. Research* 4, 1 (2022), p. 013240.

[78] S. Bergamini et al., "Holographic generation of microtrap arrays for single atoms by use of a programmable phase modulator", *J. Opt. Soc. Am. B* 21, 11 (2004), pp. 1889–1894.

[79] B. Zimmermann, T. Müller, J. Meineke, T. Esslinger, and H. Moritz, "High-resolution imaging of ultracold fermions in microscopically tailored optical potentials", *New J. Phys.* 13, 4 (2011), p. 043007.

[80] M. J. Piotrowicz et al., "Two-dimensional lattice of blue-detuned atom traps using a projected Gaussian beam array", *Phys. Rev. A* 88, 1 (2013), p. 013420.

[81] F. Nogrette et al., "Single-atom trapping in holographic 2D arrays of microtraps with arbitrary geometries", *Phys. Rev. X* 4, 2 (2014), p. 021034.

[82] H. Kim et al., "In situ single-atom array synthesis using dynamic holographic optical tweezers", *Nat. Commun.* 7, 13317 (2016).

[83] A. M. Kaufman and K.-K. Ni, "Quantum science with optical tweezer arrays of ultracold atoms and molecules", *Nat. Phys.* 17 (2021), pp. 1324–1333.

[84] M. Sroczyńska et al., "Controlling the dynamics of ultracold polar molecules in optical tweezers", *New J. Phys.* 24, 1 (2021), p. 015001.

[85] H. Kim, M. Kim, W. Lee, and J. Ahn, "Gerchberg-Saxton algorithm for fast and efficient atom rearrangement in optical tweezer traps", *Opt. Express* 27, 3 (2019), p. 2184.

[86] A. M. Kaufman et al., "Two-particle quantum interference in tunnel-coupled optical tweezers", *Science* 345, 6194 (2014).

[87] L. R. Liu et al., "Building one molecule from a reservoir of two atoms", *Science* 360, 6391 (2018), pp. 900–903.

[88] K.-N. Schymik et al., "Enhanced atom-by-atom assembly of arbitrary tweezer arrays", *Phys. Rev. A* 102, 6 (2020), p. 063107.

[89] X. He, P. Xu, J. Wang, and M. Zhan, "Rotating single atoms in a ring lattice generated by a spatial light modulator", *Opt. Express* 17, 23 (2009), pp. 21007–21014.

[90] L. Brandt et al., "Spatial light modulators for the manipulation of individual atoms", *Appl. Phys. B* 102 (2011), pp. 443–450.

[91] A. L. Gaunt and Z. Hadzibabic, "Robust Digital Holography For Ultracold Atom Trapping", *Sci. Rep.* 2, 1 (2012), p. 721.

[92] H. Bernien et al., "Probing many-body dynamics on a 51-atom quantum simulator", *Nature* 551 (2017), pp. 579–584.

[93] K. O. Roberts et al., "Steerable optical tweezers for ultracold atom studies", *Opt. Lett.* 39, 7 (2014).

[94] C. Sheng et al., "Defect-Free Arbitrary-Geometry Assembly of Mixed-Species Atom Arrays", *Phys. Rev. Lett.* 128, 8 (2022), p. 083202.

[95] I. I. Beterov and M. Saffman, "Rydberg blockade, Förster resonances, and quantum state measurements with different atomic species", *Phys. Rev. A* 92, 4 (2015), p. 042710.

[96] J. M. Auger, S. Bergamini, and D. E. Browne, "Blueprint for fault-tolerant quantum computation with Rydberg atoms", *Phys. Rev. A* 96, 5 (2017), p. 052320.

[97] K. Singh, S. Anand, A. Pocklington, J. T. Kemp, and H. Bernien, "Dual-Element, Two-Dimensional Atom Array with Continuous-Mode Operation", *Phys. Rev. X* 12, 1 (2022), p. 011040.

[98] R. V. Brooks et al., "Preparation of one ^{87}Rb and one ^{133}Cs atom in a single optical tweezer", *New J. Phys.* 23, 6 (2021), p. 065002.

[99] J. T. Zhang et al., "Forming a single molecule by magnetoassociation in an optical tweezer", *Phys. Rev. Lett.* 124, 25 (2020), p. 253401.

[100] L. D. Carr, D. Demille, R. V. Krems, and J. Ye, "Cold and Ultracold Molecules: Science, Technology and Applications", *New J. Phys.* 11 (2009), p. 055049.

[101] S. A. Moses, J. P. Covey, M. T. Miecnikowski, D. S. Jin, and J. Ye, "New frontiers for quantum gases of polar molecules", *Nat. Phys.* 13, 1 (2017), pp. 13–20.

[102] R. Sawant et al., "Ultracold polar molecules as qudits", *New J. Phys.* 22, 013027 (2020), p. 013027.

[103] B. L. Augenbraun et al., "Laser-cooled polyatomic molecules for improved electron electric dipole moment searches", *New J. Phys.* 22, 2 (2020), p. 022003.

[104] M. Saffman, T. G. Walker, and K. Mølmer, "Quantum information with Rydberg atoms", *Rev. Mod. Phys.* 82, 3 (2010), p. 2313.

[105] A. Browaeys and T. Lahaye, "Many-body physics with individually controlled Rydberg atoms", *Nat. Phys.* 16, 2 (2020), pp. 132–142.

[106] T. L. Nguyen et al., "Towards quantum simulation with circular Rydberg atoms", *Phys. Rev. X* 8, 1 (2018), p. 011032.

[107] S. R. Cohen and J. D. Thompson, "Quantum computing with circular Rydberg atoms", *PRX Quantum* 2, 3 (2021), p. 030322.

[108] A. Muni et al., "Optical coherent manipulation of alkaline-earth circular Rydberg states", *Nat. Phys.* 18, 5 (2022), pp. 502–505.

[109] J. A. Blackmore et al., "Ultracold molecules for quantum simulation: rotational coherences in CaF and RbCs", *Quant. Sci. Tech.* 4 (2019), p. 014010.

[110] V. V. Albert, J. P. Covey, and J. Preskill, "Robust Encoding of a Qubit in a Molecule", *Phys. Rev. X* 10, 3 (2020), p. 031050.

[111] B. Neyenhuis et al., "Anisotropic polarizability of ultracold polar $^{40}K^{87}Rb$ molecules", *Phys. Rev. Lett.* 109, 23 (2012), p. 230403.

[112] F. Seeßelberg et al., "Extending Rotational Coherence of Interacting Polar Molecules in a Spin-Decoupled Magic Trap", *Phys. Rev. Lett.* 121 (25 2018), p. 253401.

[113] P. D. Gregory, J. A. Blackmore, S. L. Bromley, J. M. Hutson, and S. L. Cornish, "Robust storage qubits in ultracold polar molecules", *Nat. Phys.* 17, 10 (2021), pp. 1149–1153.

[114] S. Burchesky et al., "Rotational Coherence Times of Polar Molecules in Optical Tweezers", *Phys. Rev. Lett.* 127, 12 (2021), p. 123202.

[115] S. A. Will, J. W. Park, Z. Z. Yan, H. Loh, and M. W. Zwierlein, "Coherent Microwave Control of Ultracold $^{23}Na^{40}K$ Molecules", *Phys. Rev. Lett.* 116, 22 (2016), p. 225306.

[116] J. A. Blackmore et al., "Controlling the ac Stark effect of RbCs with dc electric and magnetic fields", *Phys. Rev. A* 102, 5 (2020), p. 053316.

[117] B. Yan et al., "Observation of dipolar spin-exchange interactions with lattice-confined polar molecules", *Nature* 501, 7468 (2013), pp. 521–525.

[118] L. Christakis et al., "Probing site-resolved correlations in a spin system of ultracold molecules", *arXiv:2207.09328* (2022), URL: `https://arxiv.org/abs/2207.09328`.

[119] C. M. Holland, Y. Lu, and L. W. Cheuk, "On-Demand Entanglement of Molecules in a Reconfigurable Optical Tweezer Array", *arXiv:2207.09328* (2022), URL: `https://arxiv.org/abs/2210.06309`.

[120] M. Baranov, "Theoretical progress in many-body physics with ultracold dipolar gases", *Phys. Rep.* 464 (2008), pp. 71–111.

[121] S. Kotochigova and D. DeMille, "Electric-field-dependent dynamic polarizability and state-insensitive conditions for optical trapping of diatomic polar molecules", *Phys. Rev. A* 82, 6 (2010), p. 063421.

[122] R. Bause et al., "Tune-Out and Magic Wavelengths for Ground-State Na 23 K 40 Molecules", *Phys. Rev. Lett.* 125, 2 (2020), p. 023201.

[123] Q. Guan, S. L. Cornish, and S. Kotochigova, "Magic conditions for multiple rotational states of bialkali molecules in optical lattices", *Phys. Rev. A* 103, 4 (2021), p. 043311.

[124] B. Sundar, M. Thibodeau, Z. Wang, B. Gadway, and K. R. A. Hazzard, "Strings of ultracold molecules in a synthetic dimension", *Phys. Rev. A* 99, 1 (2019), p. 013624.

[125] M. R. Tarbutt, "Laser cooling of molecules", *Contemporary Physics* 59, 4 (2018), pp. 356–376.

[126] J. F. Barry, D. J. McCarron, E. B. Norrgard, M. H. Steinecker, and D. Demille, "Magneto-optical trapping of a diatomic molecule", *Nature* 512, 7514 (2014), pp. 286–289.

[127] V. Zhelyazkova et al., "Laser cooling and slowing of CaF molecules", *Phys. Rev. A* 89 (2014), p. 053416.

[128] L. Anderegg et al., "Laser cooling of optically trapped molecules", *Nat. Phys.* 14 (2018), pp. 890–893.

[129] A. L. Collopy et al., "3D Magneto-Optical Trap of Yttrium Monoxide", *Phys. Rev. Lett.* 121, 21 (2018), p. 213201.

[130] L. Caldwell and M. R. Tarbutt, "Sideband cooling of molecules in optical traps", *Phys. Rev. Res.* 2, 1 (2020), p. 013251.

[131] C. A. Regal, C. Ticknor, J. L. Bohn, and D. S. Jin, "Creation of ultracold molecules from a Fermi gas of atoms", *Nature* 424, 6944 (2003), pp. 47–50.

[132] J. Herbig et al., "Preparation of a Pure Molecular Quantum Gas", *Science* 301, 5639 (2003), pp. 1510–1513.

[133] T. Köhler, K. Góral, and P. S. Julienne, "Production of cold molecules via magnetically tunable Feshbach resonances", *Rev. Mod. Phys.* 78, 4 (2006), pp. 1311–1361.

[134] C. Chin, R. Grimm, P. Julienne, and E. Tiesinga, "Feshbach resonances in ultracold gases", *Rev. Mod. Phys.* 82, 2 (2010), pp. 1225–1286.

[135] U. Gaubatz, P. Rudecki, S. Schiemann, and K. Bergmann, "Population transfer between molecular vibrational levels by stimulated Raman scattering with partially overlapping laser fields. A new concept and experimental results", *The J. Chem. Phys.* 92 (1990), pp. 5363–5376.

[136] K. Bergmann, H. Theuer, and B. W. Shore, "Coherent population transfer among quantum states of atoms and molecules", *Rev. Mod. Phys.* 70, 3 (1998), pp. 1003–1025.

[137] K. K. Ni et al., "A high phase-space-density gas of polar molecules", *Science* 322, 5899 (2008), pp. 231–235.

[138] J. G. Danzl et al., "Quantum Gas of Deeply Bound Ground State Molecules", *Science* 321, 5892 (2008), pp. 1062–1066.

[139] F. Lang, K. Winkler, C. Strauss, R. Grimm, and J. H. Denschlag, "Ultracold Triplet Molecules in the Rovibrational Ground State", *Phys. Rev. Lett.* 101, 13 (2008), p. 133005.

[140] P. K. Molony et al., "Creation of ultracold ^{87}RbCs molecules in the rovibrational ground state", *Phys. Rev. Lett.* 113 (2014), p. 255301.

[141] T. Takekoshi et al., "Ultracold dense samples of dipolar RbCs molecules in the rovibrational and hyperfine ground state", *Phys. Rev. Lett.* 113, 20 (2014), p. 205301.

[142] M. Guo et al., "Creation of an Ultracold Gas of Ground-State Dipolar ^{23}Na^{87}Rb Molecules", *Phys. Rev. Lett.* 116, 20 (2016), p. 205303.

[143] J. W. Park, S. A. Will, and M. W. Zwierlein, "Ultracold Dipolar Gas of Fermionic ^{23}Na^{40}K Molecules in Their Absolute Ground State", *Phys. Rev. Lett.* 114, 20 (2015), p. 205302.

[144] M.-G. Hu et al., "Direct observation of bimolecular reactions of ultracold KRb molecules", *Science* 366, 6469 (2019), pp. 1111–1115.

[145] J. T. Zhang et al., "An optical tweezer array of ground-state polar molecules", *Quantum Sci. Technol.* 7, 3 (2022), p. 035006.

[146] T. Busch, B. G. Englert, K. Rzazewski, and M. Wilkens, "Two Cold Atoms in a Harmonic Trap", *Foundations of Physics* 28, 4 (1998), pp. 549–559.

[147] W. Neuhauser, M. Hohenstatt, P. Toschek, and H. Dehmelt, "Optical-Sideband Cooling of Visible Atom Cloud Confined in Parabolic Well", *Phys. Rev. Lett.* 41 (1978), pp. 233–236.

[148] D. J. Wineland, R. E. Drullinger, and F. L. Walls, "Radiation-Pressure Cooling of Bound Resonant Absorbers", *Phys. Rev. Lett.* 40 (1978), pp. 1639–1642.

[149] A. M. Kaufman, B. J. Lester, and C. A. Regal, "Cooling a Single Atom in an Optical Tweezer to Its Quantum Ground State", *Phys. Rev. X* 2 (2012), p. 041014.

[150] J. D. Thompson, T. G. Tiecke, A. S. Zibrov, V. Vuletić, and M. D. Lukin, "Coherence and Raman Sideband Cooling of a Single Atom in an Optical Tweezer", *Phys. Rev. Lett.* 110, 133001 (2013), p. 133001.

[151] P. Sompet et al., "Zeeman-insensitive cooling of a single atom to its two-dimensional motional ground state in tightly focused optical tweezers", *Phys. Rev. A* 95, 3 (2017), p. 031403.

[152] Y. Yu et al., "Motional Ground State Cooling Outside the Lamb-Dicke Regime", *Phys. Rev. A* 97, 6 (2018), p. 63423.

[153] K. Wang et al., "Preparation of a Hetero-nuclear Two-atom System in the 3D Motional Ground State in an Optical Tweezer", *Phys. Rev. A* 100 (2019), p. 063429.

[154] N. Lorenz, L. Festa, L. M. Steinert, and C. Gross, "Raman sideband cooling in optical tweezer arrays for Rydberg dressing", *SciPost Physics* 10, 3 (2021), p. 52.

[155] X. He et al., "Coherently forming a single molecule in an optical trap", *Science* 370, 6514 (2020), pp. 331–335.

[156] L. R. Liu et al., "Molecular Assembly of Ground-State Cooled Single Atoms", *Phys. Rev. X* 9, 2 (2019), p. 021039.

[157] W. B. Cairncross et al., "Assembly of a Rovibrational Ground State Molecule in an Optical Tweezer", *Phys. Rev. Lett.* 126, 12 (2021), p. 123402.

[158] P. K. Molony et al., "Production of Ultracold ^{87}Rb^{133}Cs in the Absolute Ground State: Complete Characterisation of the Stimulated Raman Adiabatic Passage Transfer", *ChemPhysChem* 17 (2016), pp. 3811–3817.

[159] J. Aldegunde, B. A. Rivington, P. S. Żuchowski, and J. M. Hutson, "Hyperfine energy levels of alkali-metal dimers: Ground-state polar molecules in electric and magnetic fields", *Phys. Rev. A* 78, 3 (2008), p. 033434.

[160] P. D. Gregory, J. Aldegunde, J. M. Hutson, and S. L. Cornish, "Controlling the rotational and hyperfine state of ultracold ^{87}Rb^{133}Cs molecules", *Phys. Rev. A* 94, 4 (2016), p. 041403.

[161] J. A. Blackmore, P. D. Gregory, S. L. Bromley, and S. L. Cornish, "Coherent manipulation of the internal state of ultracold 87Rb133Cs molecules with multiple microwave fields", *Phys. Chem. Chem. Phys.* 22 (2020), pp. 27529–27538.

[162] T. Takekoshi et al., "Towards the production of ultracold ground-state RbCs molecules: Feshbach resonances, weakly bound states, and the coupled-channel model", *Phys. Rev. A* 85, 3 (2012), p. 032506.

[163] M. P. Köppinger et al., "Production of optically trapped ^{87}RbCs Feshbach molecules", *Phys. Rev. A* 89, 3 (2014), p. 033604.

[164] R. V. Brooks, "Control and Collisions of ^{87}Rb and ^{133}Cs Atoms in Optical Tweezers", PhD thesis, Durham University, 2022.

[165] R. V. Brooks et al., "Feshbach Spectroscopy of Cs Atom Pairs in Optical Tweezers", *arXiv:2204.08877* (2022), URL: `https://doi.org/10.48550/arXiv.2204.08877`.

[166] S. Spence, R. V. Brooks, D. K. Ruttley, A. Guttridge, and S. L. Cornish, "Preparation of ^{87}Rb and ^{133}Cs in the motional ground state of a single optical tweezer", *New J. Phys.* 24, 10 (2022), p. 103022.

[167] E. L. Raab, M. Prentiss, A. Cable, S. Chu, and D. E. Pritchard, "Trapping of Neutral Sodium Atoms with Radiation Pressure", *Phys. Rev. Lett.* 59, 23 (1987), pp. 2631–2634.

[168] A. M. Steane, M. Chowdhury, and C. J. Foot, "Radiation force in the magneto-optical trap", *J. Opt. Soc. Am. B* 9, 12 (1992), pp. 2142–2158.

[169] P. D. Lett et al., "Optical Molasses", *J. Opt. Soc. Am. B* 6, 11 (1989), p. 2084.

[170] S. Kuhr et al., "Coherence Properties and Quantum State Transportation in an Optical Conveyor Belt", *Phys. Rev. Lett.* 91, 21 (2003), p. 213002.

[171] M. P. A. Jones et al., "Fast quantum state control of a single trapped neutral atom", *Phys. Rev. A* 75, 4 (2007), p. 040301.

[172] A. J. Kerman, "Raman sideband cooling and cold atomic collisions in optical lattices", PhD thesis, Stanford University, 2002.

[173] S. Heckmann, "Modal noise in single-mode fibers", *Opt. Lett.* 6, 4 (1981), pp. 201–203.

[174] B. Daino, G. de Marchis, and S. Piazzolla, "Analysis and measurement of modal noise in an optical fibre", Undetermined, *Electronics Letters* 15, 23 (1979), pp. 755–756.

[175] A. Cooper et al., "Alkaline-Earth atoms in optical tweezers", *Phys. Rev. X* 8, 4 (2018), p. 041055.

[176] S. Saskin, J. Wilson, B. Grinkemeyer, and J. Thompson, "Narrow-line cooling and imaging of Ytterbium atoms in an optical tweezer array", *Phys. Rev. Lett.* 122, 143002 (2019).

[177] A. Goutzoulis, *Design and Fabrication of Acousto-Optic Devices*, CRC Press, 1994.

[178] C. V. Raman and N. S. N. Nathe, "The diffraction of light by high frequency sound waves: Part I.", *Proceedings of the Indian Academy of Sciences - Section A* 2, 4 (1935), pp. 406–412.

[179] M. T. Valentine et al., "Precision steering of an optical trap by electro-optic deflection", *Opt. Lett.* 33, 6 (2008), pp. 599–601.

[180] M. S. Woody, M. Capitanio, E. M. Ostap, and Y. E. Goldman, "Electro-optic deflectors deliver advantages over acousto-optical deflectors in a high resolution, ultra-fast force-clamp optical trap", *Opt. Express* 26, 9 (2018), pp. 11181–11193.

[181] L. R. Liu, "Building Single Molecules – Reactions, Collisions, and Spectroscopy of Two Atoms", PhD thesis, Harvard University, Cambridge, Massachusetts, 2019.

[182] H. Levine, "Quantum Information Processing and Quantum Simulation with Programmable Rydberg Atom Arrays", PhD thesis, Harvard University, Cambridge, Massachusetts, 2021.

[183] I. S. Madjarov, "Entangling, controlling, and detecting individual strontium atoms in optical tweezer arrays", PhD thesis, California Institute of Technology, 2021.

[184] M. Schroeder, "Synthesis of low-peak-factor signals and binary sequences with low autocorrelation (Corresp.)", *IEEE Transactions on Information Theory* 16, 1 (1970), pp. 85–89.

[185] Y. Yang et al., "An improved crest factor minimization algorithm to synthesize multisines with arbitrary spectrum", *Physiological Measurement* 36, 5 (2015), pp. 895–910.

[186] J. Ojarand and M. Min, "Recent Advances in Crest Factor Minimization of Multisine", *Elektronika ir Elektrotechnika* 23, 2 (2017), pp. 59–62.

[187] R. M. W. van Bijnen et al., "Patterned Rydberg excitation and ionization with a spatial light modulator", *New J. Phys.* 17, 2 (2015), p. 023045.

[188] J.-B. Béguin et al., "Reduced volume and reflection for bright optical tweezers with radial Laguerre-Gauss beams", *Proceedings of the National Academy of Sciences* 117, 42 (2020), pp. 26109–26117.

[189] M. M. H. Yu, "Towards interferometry with bright solitary waves in a ring", PhD thesis, Durham University, 2016.

[190] D. C. O'Shea, T. J. Suleski, A. D. Kathman, and D. W. Prather, *Diffractive Optics: Design, Fabrication, and Test*, SPIE, 2003.

[191] R. W. Gerchberg and W. O. Saxton, "A Practical Algorithm for the Determination of Phase from Image and Diffraction Plane Pictures", *Optik* 35, 2 (1972).

[192] J. R. Fienup, "Phase retrieval algorithms: a comparison", *Appl. Opt.* 21, 15 (1982), pp. 2758–2769.

[193] Z. Zalevsky, D. Mendlovic, and R. G. Dorsch, "Gerchberg–Saxton algorithm applied in the fractional Fourier or the Fresnel domain", *Opt. Lett.* 21, 12 (1996), pp. 842–844.

[194] M. Ansmann, "Benchmarking the Superconducting Josephson Phase Qubit: The Violation of Bell's Inequality", PhD thesis, University of California, 2009.

[195] F. Ziegler et al., "A new Pulse-Pattern Generator based on LabVIEW FPGA", *Nuclear Instruments and Methods in Physics Research Section A: Accelerators, Spectrometers, Detectors and Associated Equipment* 679 (2012), pp. 1–6.

[196] P. T. Starkey et al., "A scripted control system for autonomous hardware-timed experiments", *Review of Scientific Instruments* 84, 8 (2013), p. 085111.

[197] A. Keshet and W. Ketterle, "A distributed, graphical user interface based, computer control system for atomic physics experiments", *Review of Scientific Instruments* 84, 1 (2013), p. 015105.

[198] M. T. Lichtman, "Coherent operations, entanglement, and progress toward quantum search in a large 2D array of neutral atom qubits", PhD thesis, The University of Wisconsin-Madison, 2015.

[199] *ARTIQ, open-source experimental control system*, URL: `https://m-labs.hk/experiment-control/artiq/`.

[200] E. Perego et al., "A scalable hardware and software control apparatus for experiments with hybrid quantum systems", *Review of Scientific Instruments* 89, 11 (2018), p. 113116.

[201] Y. Yu, "Coherent Creation of Single Molecules from Single Atoms", PhD thesis, Harvard University, Cambridge, Massachusetts, 2020.

[202] A. Trenkwalder, M. Zaccanti, and N. Poli, "A flexible system-on-a-chip control hardware for atomic, molecular, and optical physics experiments", *Review of Scientific Instruments* 92, 10 (2021), p. 105103.

[203] T. Wiles, "Dynamics of bright solitary matter-waves", PhD thesis, Durham University, 2013.

[204] R. Computing, *PyQt: Python bindings for The Qt Company's Qt application framework*, URL: `https://www.riverbankcomputing.com/software/pyqt/`.

[205] C. Glasbey, "An Analysis of Histogram-Based Thresholding Algorithms", *CVGIP: Graphical Models and Image Processing* 55, 6 (1993), pp. 532–537.

[206] M. Martinez-Dorantes et al., "Fast Nondestructive Parallel Readout of Neutral Atom Registers in Optical Potentials", *Phys. Rev. Lett.* 119 (2017), p. 180503.

[207] A. Bergschneider et al., "Spin-resolved single-atom imaging of Li^6 in free space", *Phys. Rev. A* 97, 063613 (2018).

[208] *XML Processing with lxml.etree*, URL: `https://lxml.de/tutorial.html`.

[209] M. Chilcott and N. Kjærgaard, "Low-cost wireless condition monitoring system for an ultracold atom machine", *Internet of Things* 13 (2021), p. 100345.

[210] T. J. Barrett et al., "An environmental monitoring network for quantum gas experiments and devices", *Quantum Sci. Technol.* 7, 2 (2022), p. 025001.

[211] I. Inc., *InfluxDB: purpose-built open source time series database*, 2021, URL: `https://influxdata.com`.

[212] B. P. Lathi and R. A. Green, *Essentials of Digital Signal Processing*, Cambridge University Press, 2014.

[213] K. Gentile and R. Cushing, *A Technical Tutorial on Digital Signal Synthesis*, Analog Devices, 1999.

[214] J. Weiner, V. S. Bagnato, S. Zilio, and P. S. Julienne, "Experiments and theory in cold and ultracold collisions", *Rev. Mod. Phys.* 71, 1 (1999), pp. 1–85.

[215] J. Dalibard and C. Cohen-Tannoudji, "Laser cooling below the Doppler limit by polarization gradients: simple theoretical models", *J. Opt. Soc. Am. B* 6 (1989), pp. 2023–2045.

[216] W. Lee, H. Kim, and J. Ahn, "Three-dimensional rearrangement of single atoms using actively controlled optical microtraps", *Opt. Express* 24, 9 (2016), pp. 9816–9825.

[217] L. D. Brown, T. T. Cai, and A. DasGupta, "Interval Estimation for a Binomial Proportion", *Statistical Science* 16, 2 (2001), pp. 101–133, URL: https://doi.org/10.1214/ss/1009213286.

[218] T. A. Savard, K. M. O'Hara, and J. E. Thomas, "Laser-noise-induced heating in far-off resonance optical traps", *Phys. Rev. A* 56, 2 (1997), R1095–R1098.

[219] G. Reymond, N. Schlosser, I. Protsenko, and P. Grangier, "Single-atom manipulations in a microscopic dipole trap", *Phys. Trans. R. Soc. A* 361 (2003), pp. 1527–1536.

[220] C. Tuchendler, A. M. Lance, A. Browaeys, Y. R. P. Sortais, and P. Grangier, "Energy distribution and cooling of a single atom in an optical tweezer", *Phys. Rev. A* 78, 3 (2008), p. 033425.

[221] A. Dareau, Y. Meng, P. Schneeweiss, and A. Rauschenbeutel, "Observation of Ultrastrong Spin-Motion Coupling for Cold Atoms in Optical Microtraps", *Phys. Rev. Lett.* 121, 25 (2018), p. 253603.

[222] R. A. Cline, J. D. Miller, M. R. Matthews, and D. J. Heinzen, "Spin relaxation of optically trapped atoms by light scattering", *Opt. Lett.* 19, 3 (1994), pp. 207–209.

[223] J. Zhang, "Assembling an array of polar molecules with full quantum-state control", PhD thesis, Harvard University, 2021.

[224] E. Knill et al., "Randomized benchmarking of quantum gates", *Phys. Rev. A* 77, 1 (2008), p. 012307.

[225] S. Kuhr et al., "Analysis of dephasing mechanisms in a standing-wave dipole trap", *Phys. Rev. A* 72 (2005), p. 023406.

[226] N. Lundblad, M. Schlosser, and J. V. Porto, "Experimental observation of magic-wavelength behavior of ^{87}Rb atoms in an optical lattice", *Phys. Rev. A* 81, 3 (2010), p. 031611.

[227] C. Sheng et al., "High-Fidelity Single-Qubit Gates on Neutral Atoms in a Two-Dimensional Magic-Intensity Optical Dipole Trap Array", *Phys. Rev. Lett.* 121, 24 (2018), p. 240501.

[228] F. A. An, E. J. Meier, and B. Gadway, "Diffusive and arrested transport of atoms under tailored disorder", *Nat. Commun.* 8, 1 (2017), p. 325.

[229] D. Leibfried, R. Blatt, C. Monroe, and D. Wineland, "Quantum dynamics of single trapped ions", *Rev. Mod. Phys.* 75 (2003), pp. 281–324.

[230] D. J. Heinzen and D. J. Wineland, "Quantum-limited cooling and detection of radio-frequency oscillations by laser-cooled ions", *Phys. Rev. A* 42 (1990), pp. 2977–2994.

[231] C. Monroe et al., "Resolved-Sideband Raman Cooling of a Bound Atom to the 3D Zero-Point Energy", *Phys. Rev. Lett.* 75, 22 (1995), pp. 4011–4014.

[232] G. Morigi, J. Eschner, and C. H. Keitel, "Ground State Laser Cooling Using Electromagnetically Induced Transparency", *Phys. Rev. Lett.* 85, 21 (2000), pp. 4458–4461.

[233] S. E. Hamann et al., "Resolved-Sideband Raman Cooling to the Ground State of an Optical Lattice", *Phys. Rev. Lett.* 80, 19 (1998), pp. 4149–4152.

[234] H. Perrin, A. Kuhn, I. Bouchoule, and C. Salomon, "Sideband cooling of neutral atoms in a far-detuned optical lattice", *Europhysics Letters* 42 (1998), pp. 395–400.

[235] A. Kaufman, "Laser-cooling atoms to indistinguishability: Atomic Hong-Ou-Mandel interference and entanglement through spin-exchange", PhD thesis, University of Colorado, 2015.

[236] S. Stenholm, "The semiclassical theory of laser cooling", *Rev. Mod. Phys.* 58, 3 (1986), pp. 699–739.

[237] Y. Wu, "Effective Raman theory for a three-level atom in the Λ configuration", *Phys. Rev. A* 54, 2 (1996), pp. 1586–1592.

[238] J. Bateman, A. Xuereb, and T. Freegarde, "Stimulated Raman transitions via multiple atomic levels", *Phys. Rev. A* 81, 4 (2010), p. 043808.

[239] R. C. Jones, "A New Calculus for the Treatment of Optical SystemsI Description and Discussion of the Calculus", *J. Opt. Soc. Am.* 31, 7 (1941), pp. 88–493.

[240] V. M. Porozova et al., "Raman sideband cooling of a single atom in an optical dipole trap: Toward a theoretical optimum in a three-dimensional regime", *Phys. Rev. A* 99, 4 (2019), p. 043406.

[241] J. I. Cirac, L. J. Garay, R. Blatt, A. S. Parkins, and P. Zoller, "Laser cooling of trapped ions: The influence of micromotion", *Phys. Rev. A* 49 (1994), pp. 421–432.

[242] G. Morigi, H. Baldauf, W. Lange, and H. Walther, "Raman sideband cooling in the presence of multiple decay channels", *Optics Communications* 187, 1-3 (2001).

[243] G. Morigi, J. I. Cirac, M. Lewenstein, and P. Zoller, "Ground-state laser cooling beyond the Lamb-Dicke limit", *Europhysics Letters (EPL)* 39, 1 (1997), pp. 13–18.

[244] E. Jaynes and F. Cummings, "Comparison of quantum and semiclassical radiation theories with application to the beam maser", *Proceedings of the IEEE* 51, 1 (1963), pp. 89–109.

[245] D. M. Meekhof, C. Monroe, B. E. King, W. M. Itano, and D. J. Wineland, "Generation of Nonclassical Motional States of a Trapped Atom", *Phys. Rev. Lett.* 76, 11 (1996), pp. 1796–1799.

[246] F. Schwabl, *Quantum Mechanics*, Springer Berlin, Heidelberg, 1995.

[247] G. Arfken, *Mathematical Methods for Physicists*, Academic Press, 1985.

[248] I. Dotsenko, "Raman spectroscopy of single atoms", PhD thesis, Bonn University, 2002.

[249] J. R. Johansson, P. D. Nation, and F. Nori, "QuTiP: An open-source Python framework for the dynamics of open quantum systems", *Computer Physics Communications* 183, 8 (2012), pp. 1760–1772.

[250] B. Albrecht et al., "Fictitious magnetic-field gradients in optical microtraps as an experimental tool for interrogating and manipulating cold atoms", *Phys. Rev. A* 94 (2016), p. 061401.

[251] M. E. Gehm, K. M. O'Hara, T. A. Savard, and J. E. Thomas, "Dynamics of noise-induced heating in atom traps", *Phys. Rev. A* 58, 5 (1998), pp. 3914–3921.

[252] F. J. Harris, "On the Use of Windows for Harmonic Analysis with the Discrete Fourier Transform", *Proc. IEEE* 66, 1 (1978), pp. 51–83.

[253] A. J. Rasmusson, M. D'Onofrio, Y. Xie, J. Cui, and P. Richerme, "Optimized pulsed sideband cooling and enhanced thermometry of trapped ions", *Phys. Rev. A* 104, 4 (2021), p. 043108.

[254] F. Diedrich, J. C. Bergquist, W. M. Itano, and D. J. Wineland, "Laser Cooling to the Zero-Point Energy of Motion", *Phys. Rev. Lett.* 62, 4 (1989), pp. 403–406.

[255] A. C. Keesling, "Quantum Simulation and Quantum Information Processing with Programmable Rydberg Atom Arrays", PhD thesis, Harvard University, Cambridge, Massachusetts, 2021.

[256] R. Shadmehr and S. Wise, *Supplementary Documents for Computational Neurobiology of Reaching and Pointing*, MIT Press, Cambridge, MA, 2005.

[257] D. Hucul et al., "On the transport of atomic ions in linear and multidimensional ion trap arrays", *Quantum Information and Computation* 8, 6-7 (2008), pp. 0501–0578.

[258] S. Schulz, U. Poschinger, K. Singer, and F. Schmidt-Kaler, "Optimization of segmented linear Paul traps and transport of stored particles", *Fortschritte der Physik* 54, 8-10 (2006), pp. 648–665.

[259] A. Couvert, T. Kawalec, G. Reinaudi, and D. Guéry-Odelin, "Optimal transport of ultracold atoms in the non-adiabatic regime", *EPL (Europhysics Letters)* 83, 1 (2008), p. 13001.

[260] M. Murphy, L. Jiang, N. Khaneja, and T. Calarco, "High-fidelity fast quantum transport with imperfect controls", *Phys. Rev. A* 79, 2 (2009), p. 020301.

[261] X. Chen, E. Torrontegui, D. Stefanatos, J.-S. Li, and J. G. Muga, "Optimal trajectories for efficient atomic transport without final excitation", *Phys. Rev. A* 84, 4 (2011), p. 043415.

[262] E. Torrontegui et al., "Fast atomic transport without vibrational heating", *Phys. Rev. A* 83, 1 (2011), p. 013415.

[263] D. Guéry-Odelin et al., "Shortcuts to adiabaticity: Concepts, methods, and applications", *Rev. Mod. Phys.* 91 (4 2019), p. 045001.

[264] M. R. Lam et al., "Demonstration of Quantum Brachistochrones between Distant States of an Atom", *Phys. Rev. X* 11, 1 (2021), p. 011035.

[265] A. M. Kaufman et al., "Entangling two transportable neutral atoms via local spin exchange", *Nature* 527 (2015), pp. 208–211.

[266] O. Docenko et al., "Spectroscopic data, spin-orbit functions, and revised analysis of strong perturbative interactions for the A $^1\Sigma^+$ and b$^3\Pi$ states of RbCs", *Phys. Rev. A* 81, 4 (2010), p. 042511.

[267] R. Vexiau et al., "Dynamic dipole polarizabilities of heteronuclear alkali dimers: optical response, trapping and control of ultracold molecules", *Int. Rev. Phys. Chem.* 36 (2017), pp. 709–750.

[268] J. D. Hood et al., "Multichannel interactions of two atoms in an optical tweezer", *Phys. Rev. Research* 2, 2 (2020), p. 023108.

[269] M. Krych and Z. Idziaszek, "Controlled collisions of two ultracold atoms in separate harmonic traps", *Phys. Rev. A* 80, 2 (2009), p. 022710.

[270] T. Fogarty, T. Busch, J. Goold, and M. Paternostro, "Non-locality of two ultracold trapped atoms", *New J. Phys.* 13, 2 (2011), p. 023016.

[271] H. Feshbach, "Unified theory of nuclear reactions", *Annals of Physics* 5, 4 (1958), pp. 357–390.

[272] U. Fano, "Effects of Configuration Interaction on Intensities and Phase Shifts", *Phys. Rev.* 124, 6 (1961), pp. 1866–1878.

[273] E. Tiesinga, B. J. Verhaar, and H. T. C. Stoof, "Threshold and resonance phenomena in ultracold ground-state collisions", *Phys. Rev. A* 47, 5 (1993), pp. 4114–4122.

[274] S. Inouye et al., "Observation of Feshbach resonances in a Bose–Einstein condensate", *Nature* 392, 6672 (1998), pp. 151–154.

[275] Y. Wang, J. P. D'Incao, and B. D. Esry, "Ultracold three-body collisions near narrow Feshbach resonances", *Phys. Rev. A* 83 (2011), p. 042710.

[276] Y. Wang and P. S. Julienne, "Universal van der Waals physics for three cold atoms near Feshbach resonances", *Nat. Phys.* 10, 10 (2014), pp. 768–773.

[277] V. Vuletic, A. J. Kerman, C. Chin, and S. Chu, "Observation of low-field feshbach resonances in collisions of cesium atoms", *Phys. Rev. Lett.* 82, 7 (1999).

[278] A. M. Thomas, "Ultra-cold collisions and evaporative cooling of caesium in a magnetic trap", PhD thesis, University of Oxford, 2004.

[279] I. Bloch, J. Dalibard, and W. Zwerger, "Many-body physics with ultracold gases", *Review of Modern Physics* 80 (2008), pp. 885–964.

[280] E. Timmermans, P. Tommasini, M. Hussein, and A. Kerman, "Feshbach resonances in atomic Bose–Einstein condensates", *Phys. Rep.* 315, 1 (1999), pp. 199–230.

[281] F. H. Mies, E. Tiesinga, and P. S. Julienne, "Manipulation of Feshbach resonances in ultracold atomic collisions using time-dependent magnetic fields", *Phys. Rev. A* 61, 2 (2000), p. 022721.

[282] J. M. Hutson and P. Soldán, "Molecule formation in ultracold atomic gases", *International Reviews in Physical Chemistry* 25, 4 (2006), pp. 497–526.

[283] E. L. Bolda, E. Tiesinga, and P. S. Julienne, "Effective-scattering-length model of ultracold atomic collisions and Feshbach resonances in tight harmonic traps", *Phys. Rev. A* 66, 1 (2002), p. 013403.

[284] D. M. Bauer, M. Lettner, C. Vo, G. Rempe, and S. Dürr, "Control of a magnetic Feshbach resonance with laser light", *Nat. Phys.* 5, 5 (2009).

[285] H. Feshbach, *Theoretical Nuclear Physics: Nuclear Reactions*, Theoretical Nuclear Physics Vol. 2, Wiley, 1992.

[286] J. M. Hutson, "Feshbach resonances in ultracold atomic and molecular collisions: threshold behaviour and suppression of poles in scattering lengths", *New J. Phys.* 9, 5 (2007), p. 152.

[287] J. Dalibard, "Collisional dynamics of ultracold atomic gases", in: *Bose-Einstein Condensation in Atomic Gases*, vol. 140, 1998, pp. 321–349.

[288] B. Bransden and C. Joachain, *Quantum Mechanics*, Prentice Hall, 2000.

[289] J. Sakurai and J. Napolitano, *Modern Quantum Mechanics*, Cambridge University Press, 2020.

[290] M. Berninger et al., "Feshbach resonances, weakly bound molecular states, and coupled-channel potentials for cesium at high magnetic fields", *Phys. Rev. A* 87, 3 (2013), p. 032517.

[291] H. J. Patel, C. L. Blackley, S. L. Cornish, and J. M. Hutson, "Feshbach resonances, molecular bound states, and prospects of ultracold-molecule formation in mixtures of ultracold K and Cs", *Phys. Rev. A* 90, 3 (2014), p. 032716.

[292] J. M. Hutson and C. R. Le Sueur, "MOLSCAT: A program for non-reactive quantum scattering calculations on atomic and molecular collisions", *Computer Physics Communications* 241 (2019), pp. 9–18.

[293] J. M. Hutson and C. R. Le Sueur, "BOUND and FIELD: Programs for calculating bound states of interacting pairs of atoms and molecules", *Computer Physics Communications* 241 (2019), pp. 1–8.

[294] A. J. Moerdijk, B. J. Verhaar, and A. Axelsson, "Resonances in ultracold collisions of ^{6}Li, ^{7}Li, and ^{23}Na", *Phys. Rev. A* 51, 6 (1995), pp. 4852–4861.

[295] C. Zener, "Non-adiabatic crossing of energy levels", *Proceedings of the Royal Society of London. Series A, Containing Papers of a Mathematical and Physical Character* 137, 833 (1932), pp. 696–702.

[296] D. Blume and C. H. Greene, "Fermi pseudopotential approximation: Two particles under external confinement", *Phys. Rev. A* 65, 4 (2002), p. 043613.

[297] A. Derevianko, J. F. Babb, and A. Dalgarno, "High-precision calculations of van der Waals coefficients for heteronuclear alkali-metal dimers", *Phys. Rev. A* 63, 5 (2001), p. 052704.

[298] Z. Idziaszek and T. Calarco, "Analytical solutions for the dynamics of two trapped interacting ultracold atoms", *Phys. Rev. A* 74 (2 2006), p. 022712.

[299] G. E. Andrews, R. Askey, and R. Roy, *Special Functions*, Encyclopedia of Mathematics and its Applications, Cambridge University Press, 1999.

[300] P. Naidon, E. Tiesinga, W. F. Mitchell, and P. S. Julienne, "Effective-range description of a Bose gas under strong one- or two-dimensional confinement", *New J. Phys.* 9, 1 (2007), pp. 19–19.

[301] P.-I. Schneider, Y. V. Vanne, and A. Saenz, "Feshbach resonances of harmonically trapped atoms", *Phys. Rev. A* 83, 3 (2011), p. 030701.

[302] M. Olshanii, "Atomic Scattering in the Presence of an External Confinement and a Gas of Impenetrable Bosons", *Phys. Rev. Lett.* 81, 5 (1998), pp. 938–941.

[303] S. Sala, P. I. Schneider, and A. Saenz, "Inelastic confinement-induced resonances in low-dimensional quantum systems", *Phys. Rev. Lett.* 109, 7 (2012), p. 073201.

[304] R. Stock, I. H. Deutsch, and E. L. Bolda, "Quantum State Control via Trap-Induced Shape Resonance in Ultracold Atomic Collisions", *Phys. Rev. Lett.* 91, 18 (2003), p. 183201.

[305] T. Bergeman, M. G. Moore, and M. Olshanii, "Atom-Atom Scattering under Cylindrical Harmonic Confinement: Numerical and Analytic Studies of the Confinement Induced Resonance", *Phys. Rev. Lett.* 91, 16 (2003), p. 163201.

[306] E. Haller et al., "Confinement-Induced Resonances in Low-Dimensional Quantum Systems", *Phys. Rev. Lett.* 104, 15 (2010), p. 153203.

[307] B. Fröhlich et al., "Radio-Frequency Spectroscopy of a Strongly Interacting Two-Dimensional Fermi Gas", *Phys. Rev. Lett.* 106, 10 (2011), p. 105301.

[308] V. Peano, M. Thorwart, C. Mora, and R. Egger, "Confinement-induced resonances for a two-component ultracold atom gas in arbitrary quasi-one-dimensional traps", *New J. Phys.* 7 (2005), pp. 192–192.

[309] J. P. Kestner and L.-M. Duan, "Anharmonicity-induced resonances for ultracold atoms and their detection", *New J. Phys.* 12, 5 (2010), p. 053016.

[310] S.-G. Peng, H. Hu, X.-J. Liu, and P. D. Drummond, "Confinement-induced resonances in anharmonic waveguides", *Phys. Rev. A* 84, 4 (2011), p. 043619.

[311] S. Sala et al., "Coherent Molecule Formation in Anharmonic Potentials Near Confinement-Induced Resonances", *Phys. Rev. Lett.* 110, 20 (2013), p. 203202.

[312] J. F. Bertelsen and K. Mølmer, "Association of heteronuclear molecules in a harmonic oscillator well", *Phys. Rev. A* 76, 4 (2007), p. 043615.

[313] K. Jachymski, Z. Idziaszek, and T. Calarco, "Feshbach resonances in a nonseparable trap", *Phys. Rev. A* 87, 4 (2013), p. 042701.

[314] Z. Idziaszek, T. Calarco, and P. Zoller, "Controlled collisions of a single atom and an ion guided by movable trapping potentials", *Phys. Rev. A* 76, 3 (2007), p. 033409.

[315] R. Stock and I. H. Deutsch, "Trap-induced resonances in controlled collisions of cesium atoms", *Phys. Rev. A* 73, 3 (2006), p. 032701.

[316] T. Stöferle, H. Moritz, K. Günter, M. Köhl, and T. Esslinger, "Molecules of Fermionic Atoms in an Optical Lattice", *Phys. Rev. Lett.* 96, 3 (2006), p. 030401.

[317] K. M. Jones, E. Tiesinga, P. D. Lett, and P. S. Julienne, "Ultracold photoassociation spectroscopy: Long-range molecules and atomic scattering", *Rev. Mod. Phys.* 78, 2 (2006), pp. 483–535.

[318] P. Courteille, R. S. Freeland, D. J. Heinzen, F. A. van Abeelen, and B. J. Verhaar, "Observation of a Feshbach Resonance in Cold Atom Scattering", *Phys. Rev. Lett.* 81, 1 (1998), pp. 69–72.

[319] F. A. van Abeelen, D. J. Heinzen, and B. J. Verhaar, "Photoassociation as a probe of Feshbach resonances in cold-atom scattering", *Phys. Rev. A* 57, 6 (1998), R4102–R4105.

[320] M. Junker et al., "Photoassociation of a Bose-Einstein Condensate near a Feshbach Resonance", *Phys. Rev. Lett.* 101, 6 (2008), p. 060406.

[321] V. Kokoouline, O. Dulieu, R. Kosloff, and F. Masnou-Seeuws, "Mapped Fourier methods for long-range molecules: Application to perturbations in the Rb2(0u+) photoassociation spectrum", *The Journal of Chemical Physics* 110, 20 (1999), pp. 9865–9876.

[322] F. A. van Abeelen and B. J. Verhaar, "Time-Dependent Feshbach Resonance Scattering and Anomalous Decay of a Na Bose-Einstein Condensate", *Phys. Rev. Lett.* 83, 8 (1999), pp. 1550–1553.

[323] M. D. Frye, B. C. Yang, and J. M. Hutson, "Ultracold collisions of Cs atoms in excited Zeeman and hyperfine states", *Phys. Rev. A* 100 (2019), p. 022702.

[324] K. Pilch et al., "Observation of interspecies Feshbach resonances in an ultracold Rb-Cs mixture", *Phys. Rev. A* 79, 4 (2009), p. 042718.

[325] A. Chotia et al., "Long-Lived Dipolar Molecules and Feshbach Molecules in a 3D Optical Lattice", *Phys. Rev. Lett.* 108, 8 (2012), p. 080405.

[326] Q. Beaufils et al., "Radio-frequency association of molecules: an assisted Feshbach resonance", *The European Physical Journal D* 56, 1 (2009), p. 99.

[327] A. D. Lange et al., "Determination of atomic scattering lengths from measurements of molecular binding energies near Feshbach resonances", *Phys. Rev. A* 79, 1 (2009), p. 013622.

[328] O. Dulieu and C. Gabbanini, "Formation and interactions of cold and ultracold molecules: new challenges for interdisciplinary physics", *Reports on Progress in Physics* 72, 8 (2009).

[329] C.-H. Wu, J. W. Park, P. Ahmadi, S. Will, and M. W. Zwierlein, "Ultracold Fermionic Feshbach Molecules of ^{23}Na^{40}K", *Phys. Rev. Lett.* 109, 8 (2012), p. 085301.

[330] J. S. Rosenberg, L. Christakis, E. Guardado-Sanchez, Z. Z. Yan, and W. S. Bakr, "Observation of the Hanbury Brown–Twiss effect with ultracold molecules", *Nat. Phys.* 18, 9 (2022), pp. 1062–1066.

[331] D. Capecchi et al., "Observation of confinement-induced resonances in a 3D lattice", *arXiv:2209.12504* (2022), URL: `https://arxiv.org/abs/2209.12504`.

[332] J. J. Zirbel et al., "Heteronuclear molecules in an optical dipole trap", *Phys. Rev. A* 78, 1 (2008), p. 013416.

[333] D. J. McCarron, H. W. Cho, D. L. Jenkin, M. P. Köppinger, and S. L. Cornish, "Dual-species Bose-Einstein condensate of ^{87}Rb and ^{133}Cs", *Phys. Rev. A* 84, 1 (2011), p. 011603.

[334] S. A. Moses et al., "Creation of a low-entropy quantum gas of polar molecules in an optical lattice", *Science* 350, 6261 (2015), pp. 659–662.

[335] L. Reichsöllner, A. Schindewolf, T. Takekoshi, R. Grimm, and H.-C. Nägerl, "Quantum Engineering of a Low-Entropy Gas of Heteronuclear Bosonic Molecules in an Optical Lattice", *Phys. Rev. Lett.* 118, 7 (2017), p. 073201.

[336] K. Aikawa et al., "Toward the production of quantum degenerate bosonic polar molecules, ^{41}K^{87}Rb", *New J. Phys.* 11, 5 (2009), p. 055035.

[337] P. D. Gregory et al., "A Simple, Versatile Laser System for the Creation of Ultracold Ground State Molecules", *New J. Phys.* 17, 5 (2015), p. 055006.

[338] L. Caldwell and M. R. Tarbutt, "General approach to state-dependent optical-tweezer traps for polar molecules", *Phys. Rev. Res.* 3, 1 (2021).

[339] E. Kuznetsova, S. T. Rittenhouse, H. R. Sadeghpour, and S. F. Yelin, "Rydberg atom mediated polar molecule interactions: a tool for molecular-state conditional quantum gates and individual addressability", *Phys. Chem. Chem. Phys.* 13, 38 (2011), pp. 17115–17121.

[340] C. Zhang and M. R. Tarbutt, "Quantum computation in a hybrid array of molecules and Rydberg atoms", *arXiv:2204.04276* (2022), URL: `https://arxiv.org/abs/2204.04276`.

[341] K. Wang, C. P. Williams, L. R. Picard, N. Y. Yao, and K.-K. Ni, "Enriching the quantum toolbox of ultracold molecules with Rydberg atoms", *arXiv:2204.05293* (2022), URL: `https://arxiv.org/abs/2204.05293`.

[342] E. Kuznetsova, S. T. Rittenhouse, H. R. Sadeghpour, and S. F. Yelin, "Rydberg-atom-mediated nondestructive readout of collective rotational states in polar-molecule arrays", *Phys. Rev. A* 94, 3 (2016), p. 032325.

[343] M. Zeppenfeld, "Nondestructive detection of polar molecules via Rydberg atoms", *Europhysics Letters* 118, 1 (2017), p. 13002.

[344] F. Jarisch and M. Zeppenfeld, "State resolved investigation of Förster resonant energy transfer in collisions between polar molecules and Rydberg atoms", *New J. Phys.* 20, 11 (2018), p. 113044.

[345] S. T. Rittenhouse and H. R. Sadeghpour, "Ultracold Giant Polyatomic Rydberg Molecules: Coherent Control of Molecular Orientation", *Phys. Rev. Lett.* 104, 24 (2010), p. 243002.

[346] J. Aguilera-Fernández, H. R. Sadeghpour, P. Schmelcher, and R. González-Férez, "Ultralong-Range Rb-KRb Rydberg Molecules: Selected Aspects of Electronic Structure, Orientation and Alignment", *Journal of Physics: Conference Series* 635, 1 (2015), p. 012023.

[347] R. González-Férez, H. R. Sadeghpour, and P. Schmelcher, "Rotational hybridization, and control of alignment and orientation in triatomic ultralong-range Rydberg molecules", *New J. Phys.* 17, 1 (2015), p. 013021.